Stable Orbits in the Small-Body Problem

An Application to the Psyche Mission

Stijn Mast

Technische Universiteit Delft

TU Delft

JPL
Jet Propulsion Laboratory
California Institute of Technology

Front cover: Artist illustration of the Psyche mission spacecraft orbiting asteroid (16) Psyche. Image courtesy NASA/JPL-Caltech.

Stable Orbits in the Small-Body Problem

An Application to the Psyche Mission

by

Stijn Mast

to obtain the degree of Master of Science
at Delft University of Technology,
to be defended publicly on Friday August 31, 2018 at 10:00 AM.

Student number:	4279425	
Project duration:	October 2, 2017 – August 31, 2018	
Thesis committee:	Ir. R. Noomen,	TU Delft
	Dr. D.M. Stam,	TU Delft
	Ir. J.A. Melkert,	TU Delft
Advisers:	Ir. R. Noomen,	TU Delft
	Dr. J.A. Sims,	JPL
	Dr. S. Eggl,	JPL
	Dr. G. Lantoine,	JPL

An electronic version of this thesis is available at `http://repository.tudelft.nl/`.

TU Delft

This page is intentionally left blank.

Preface

Before you lies the thesis *Stable Orbits in the Small-Body Problem: An Application to the Psyche Mission*. This thesis has been written to obtain the degree of Master of Science in Aerospace Engineering at Delft University of Technology. Its contents are intended for anyone with an interest in the field of spacecraft trajectory dynamics and stability in the vicinity of small celestial bodies. The methods presented in this thesis have been applied extensively to the Psyche mission. Consequently, the work can be of interest to anyone involved in the Psyche mission.

This research was carried out at the Jet Propulsion Laboratory, California Institute of Technology, as part of the JPL Visiting Student Research Program sponsored by the National Aeronautics and Space Administration. Reference herein to any specific commercial product, process, or service by trade name, trademark, manufacturer, or otherwise, does not constitute or imply its endorsement by the United States Government or the Jet Propulsion Laboratory, California Institute of Technology.

The road to the successful completion of my work has been challenging and I would not have been able to reach my goals without the support and guidance of the many people around me. Firstly, I would like to thank my supervisors, ir. Ron Noomen and Dr. Jon Sims. During weekly meetings, we discussed the direction of my research. Dr. Sims also made it possible for me to present my work at JPL several times and provided all the logistic support required for me to carry out my work. The value of carrying out research at the world-renowned Jet Propulsion Laboratory is difficult to put into words. I would also like to thank Dr. Siegfried Eggl for spending hours with me discussing my work and for providing crucial input. Furthermore, I wish to thank Dr. Gregory Lantoine, Dr. Stephen Broschart, Dr. Martin Lo, Dr. Dayung Koh and Dr. Robyn Woollands for their advice as well. My gratitude goes out to Airbus Defence & Space Netherlands and the Justus & Louise Van Effen Research Grant for providing essential financial support.

Finally, I thank my parents, Raf Mast and An Deroo, for always believing in me and encouraging me to pursue my dreams.

Stijn Mast
Delft, August 2018

This page is intentionally left blank.

Abstract

Over the past few years, space missions to minor celestial bodies have gained increased attention from the space community. A prime example is the selection of Psyche as the National Astronautics and Space Administration's (NASA) fourteenth Discovery Program mission. Orbital dynamics in the vicinity of small irregular bodies pose great challenges for trajectory design. In particular, science orbits close to the surface of small bodies are often strongly perturbed by the irregular gravity field. These irregularities can potentially perturb the trajectory of a spacecraft in such a way that it becomes uncontrollable, resulting in impact on the surface of the central body or escape from the system. A less dramatic consequence would be the need for costly orbit maintenance maneuvers to counteract these instabilities, which is undesirable. For uniformly rotating bodies such as the Psyche asteroid, mean motion resonances with the asteroid rotation amplify instabilities even further, warranting the need for a systematic study of orbital stability in such systems.

In this research project, to increase our understanding of these dynamically challenging environments, firstly analytical approximate solutions are derived in a uniformly rotating gravity field. The starting point of these derivations is the Gauss Planetary Equations (GPE) for the semi-major axis and the eccentricity of the orbit. The resulting expressions clearly show the detrimental impact of mean motion resonances with asteroid rotation. For prograde orbits, terms appear that become infinitely large in magnitude as the mean motion of orbiting spacecraft approaches the 1:2, 1:1, 3:2 and 2:1 resonances with the rotation of the central body. Similar terms appear for retrograde orbits. However, the magnitude of these terms always remains finite, which shows that retrograde orbits are more robust against instabilities caused by mean motion resonances. A comparison with numerical results validates that the analytically derived solutions adequately approximate the real solution under the specified assumptions.

Secondly, an extensive numerical characterization of stability in the uniformly rotating second degree and order gravity field is carried out by uniformly sampling the initial condition space and the gravity field harmonic coefficients. In doing so, a stability condition similar to Bounded-Input, Bounded-Output (BIBO) stability is applied. Using the BIBO-stability condition, stability plots are generated that can be used to quickly inform mission designers on stable and unstable regions in the phase space for the majority of small bodies. In addition, a conservative sufficient empirical stability condition for the maximum unstable semi-major axis of circular orbits around small bodies is derived. The BIBO-stability plots are used to assess the current science orbit selection for the Psyche mission and show that the two exterior circular orbits at an inclination of 90 degrees are BIBO-stable. However, it is advised to increase the inclination of the second innermost orbit beyond 90 degrees to ensure orbit stability in case the gravity field of the Psyche asteroid is very irregular. Similarly, the innermost orbit is likely to only be stable beyond an inclination of 140 degrees and an eccentricity close to 0.1 is recommended to reach altitudes closer to the surface of the Psyche asteroid in order to increase the science output of the mission. A comparison of the orbital results obtained in a second and eighth degree and order gravity field demonstrates the validity of using a low degree and order field for the preliminary characterization of stability around the Psyche asteroid.

After that, a different notion of stability is applied to the same search space. This condition is based on the regularity or chaoticity of spacecraft trajectories, quantified by the Fast Lyapunov In-

dicator (FLI). Our results show that FLI maps provide more rich information, especially regarding the detection of families of periodic solutions. In addition, the FLI distinguishes between stable and unstable motion more effectively when compared to a BIBO-stability constraint. Often, it is able to detect the instability of a trajectory very soon, even when the trajectory appears to be stable. However, this comes at the cost of an increased computational workload due to the required numerical integration of deviation vectors using the variational equations. Nonetheless, the FLI is recommended as an effective and independent complementary mission design tool. Stability plots using the FLI condition overall lead to the same conclusions as mentioned in the previous paragraph when it comes to the selection of science orbits for the Psyche mission.

The initial work presented in this thesis can be developed further into a complementary mission design tool for future small-body missions.

List of Abbreviations

AO	Adaptive Optics
BIBO	Bounded-Input, Bounded-Output
BoL	Beginning-of-Life
CoM	Center of Mass
EOM	Equations Of Motion
Fe	Iron (element)
FLI	Fast Lyapunov Indicator
GALI	General Alignment Index
GPE	Gauss Planetary Equations
IVP	Initial Value Problem
JPL	Jet Propulsion Laboratory
LCE	Lyapunov Characteristic Exponent
LI	Lyapunov Indicator
LPE	Lagrange Planetary Equations
MEGNO	Mean Exponential Growth factor of Nearby Orbits
MESSENGER	MErcury Surface, Space ENvironment, GEochemistry and Ranging
mLCE	maximum Lyapunov Characteristic Exponent
MMS	Magnetospheric Multiscale Mission
NASA	National Aeronautics and Space Administration
NEAR	Near Earth Asteroid Rendezvous
Ni	Nickel (element)
ODE	Ordinary Differential Equation
OFLI	Orthogonal Fast Lyapunov Indicator
RKF78	Runge-Kutta Fehlberg 7(8)
RLI	Relative Lyapunov Indicator
RMS	Root-Mean-Square
SALI	Smaller Alignment Index
SBDT	Small-Body Dynamics Toolkit
SC	Spacecraft
SEP	Solar Electric Propulsion
SRP	Solar Radiation Pressure
SSL	Space Systems/Loral
TB	Third-Body
TDB	Barycentric Dynamical Time
TRL	Technology Readiness Level

This page is intentionally left blank.

List of Symbols

Roman Symbol	Parameter	Unit
a	Semi-major axis	m
$\boldsymbol{a}$	Acceleration vector	m/s^2
A	Hessian matrix	n.a.
a_c	Critical semi-major axis	m
a_s	Empirical stability limit	m
B_{SC}	Spacecraft mass-to-area ratio	kg/m^2
C_J	Jacobi constant	m^2/s^2
C_{J_x}	Jacobi constant of intersection	m^2/s^2
C_{nm}	Spherical harmonic coefficient	-
C_R	Spacecraft reflectivity coefficient	-
d	Distance	m
D	Spectral distance	-
e	Eccentricity	-
$\boldsymbol{e}$	Eccentricity vector	-
$\boldsymbol{f}$	Vector containing first-order derivatives of EOM (flow)	n.a.
F_r	Acceleration in radial direction	m/s^2
F_{λ_t}	Acceleration in direction of motion	m/s^2
h	Specific angular momentum	m^2/s
$\boldsymbol{h}$	Specific angular momentum vector	m^2/s
H	Hamiltonian	m^2/s^2
i	Inclination	rad
I	Identity matrix	-
I	Mass moment of inertia	$kg\,m^2$
J_n	Zonal harmonic coefficient of n'th order	-
M	Mass	kg
M	Mean anomaly	rad
n	Mean motion	rad/s
$\tilde{n}$	Perturbed mean motion	rad/s
N	Number of integrator steps	-
P_{nm}	Associated Legendre polynomial	-
r	Radial distance	m
$\boldsymbol{r}$	Radial distance vector	m
R	Radial dimension	m
R_3	Rotation matrix about z-axis	-
r_a	Apoapsis radius	m
r_e	Spherical harmonic reference radius	m
r_p	Periapsis radius	m
r_s	1:1 resonance radius	m
S_{nm}	Spherical harmonic coefficient	-
t	Time	s
T	Period	s
T_s	Sidereal rotation period of central body	s

u	Argument of latitude	rad
U	Gravity potential	m^2/s^2
U_p	Perturbing gravity potential	m^2/s^2
v	Velocity	m/s
$\boldsymbol{v}$	Velocity vector	m/s
V	Effective potential	m^2/s^2
$\boldsymbol{w}$	Deviation vector	n.a.
$\boldsymbol{x}$	Spacecraft state vector	n.a.

Greek Symbol	**Parameter**	**Unit**
α	Semi-major axis ellipsoid	m
β	Intermediate axis ellipsoid	m
γ	Semi-minor axis ellipsoid	m
δ	Latitude	rad
δ_{nm}	Kronecker delta function	-
θ	True anomaly	rad
λ	Eigenvalue	-
λ	Longitude	rad
λ_t	True longitude	rad
μ	Gravitational parameter	m^3/s^2
ν	Central body shape parameter	-
σ	Central body mass distribution parameter	-
τ	Central body rotation angle	rad
Φ	State transition matrix	n.a.
χ	Simplifying parameter, related to longitude	rad
χ_1	Maximum Lyapunov Characteristic Exponent	1/s
ψ	Ratio true longitude secular rate over the mean motion	-
ω	Argument of periapsis	rad
$\bar{\omega}$	Longitude Argument of periapsis	rad
ω_A	Central body rotational rate	rad/s
$\boldsymbol{\omega_A}$	Central body rotational rate vector	rad/s
Ω	Right ascension of the ascending node	rad

Constant	**Parameter**	**Value**	**Unit**
a_J	Semi-major axis Jupiter	$7.7857\ 10^{11}$	m
AU	Astronomical unit	$1.49597871\ 10^{11}$	m
c	Speed of light	$2.99792458\ 10^{8}$	m/s
W_S	Mean solar irradiance at 1 AU	$1.361\ 10^{3}$	W/m^2
μ_S	Gravitational parameter Sun	$1.32712\ 10^{20}$	m^3/s^2
μ_J	Gravitational parameter Jupiter	$1.26687\ 10^{18}$	m^3/s^2

Contents

Preface v

Abstract vii

List of Abbreviations ix

List of Symbols xi

1 Introduction 1

2 Mission Background 3
2.1 Asteroids . . . 3
2.2 Psyche . . . 4
2.2.1 Orbital Parameters . . . 5
2.2.2 Mass . . . 5
2.2.3 Shape . . . 5
2.2.4 Gravity Field . . . 7
2.3 Mission . . . 8
2.3.1 Objectives . . . 8
2.3.2 Spacecraft . . . 8
2.3.3 Trajectory Design . . . 10

3 Physical Environment 13
3.1 Perturbations . . . 13
3.2 Gravity Field . . . 14
3.2.1 Spherical Harmonics . . . 14
3.2.2 Second Degree and Order Gravity Field . . . 16
3.2.3 Higher Degree and Order Gravity Field . . . 19
3.3 Equations of Motion . . . 21

4 Analytical Analysis 23
4.1 Assumptions and Simplifications . . . 24
4.1.1 Second Degree and Order Gravity Potential . . . 24
4.1.2 Radial Distance to Center of Body . . . 24
4.1.3 True Anomaly and Longitude of Periapsis . . . 24
4.2 Gauss Planetary Equations . . . 26
4.3 Solutions for $\frac{da}{dt}$ and $\frac{de}{dt}$ . . . 27
4.4 Solutions for $a(t)$ and $e(t)$ . . . 27
4.5 Comparison with High-Fidelity Numerical Integration . . . 29

5 Simulator 35
5.1 Small-Body Dynamics Toolkit . . . 35
5.2 Integrator . . . 36
5.3 Software Architecture . . . 37

6 Numerical Stability Analysis 41
6.1 Practical Definition Stability . . . 41
6.2 Methodology . . . 44
6.2.1 Analysis *A* . . . 44
6.2.2 Analysis *B* . . . 45
6.2.3 Analysis *C* . . . 46
6.3 Analysis *A* . . . 46
6.3.1 Stability plots . . . 46
6.3.2 Comparison $\sigma = 0.5$, 0.75 and 1.0 . . . 48
6.3.3 Empirical stability limit . . . 49
6.3.4 Results for Psyche ($\sigma \approx 0.5$) . . . 52
6.4 Analysis *B* . . . 55
6.5 Analysis *C* . . . 57

7 Chaos Indicators 61
7.1 Overview . . . 61
7.2 Fast Lyapunov Indicators . . . 63
7.2.1 Background and Motivation . . . 63
7.2.2 Variational Equations . . . 64
7.2.3 Definition and Computation of FLI/OFLI . . . 65
7.3 Regular and Chaotic Motion . . . 67
7.3.1 Comparison Regular and Chaotic Orbits . . . 68
7.3.2 Sampling of Initial Conditions . . . 71
7.3.3 Threshold Regular and Chaotic Orbits . . . 71
7.4 Characterizing Stability . . . 72
7.4.1 FLI and OFLI Maps . . . 74
7.4.2 Comparison BIBO- and FLI-Stability Conditions . . . 77
7.4.3 Psyche Mission . . . 81

8 Verification and Validation 83
8.1 Comparison with Small-Body Dynamics Toolkit . . . 83
8.2 BIBO-Stability Analysis . . . 85
8.3 FLI-Stability Analysis . . . 85

9 Conclusions 89

10 Recommendations 91

A Reference Frames and Coordinate Transformations 93
A.1 Rotating and Inertial Reference Frame Transformations . . . 93
A.2 Cartesian Coordinates to Keplerian Elements . . . 94
A.3 Keplerian Elements to Cartesian Coordinates . . . 95

B Phase Space Characterization 97
B.1 Zero-Velocity Surfaces . . . 97
B.2 Equilibria and Stability . . . 98
B.3 Stable Trajectories around Equilibria . . . 100

C Second Degree and Order Gravity Field Derivatives 103

D Software Flow Diagrams 105

Bibliography 107

1 Introduction

On January 4, 2017, the National Astronautics and Space Administration (NASA) selected Psyche as the fourteenth mission of its Discovery Program. The mission targets asteroid (16) Psyche and aims to be launched in 2022, arriving at its target in 2026 (Oh et al., 2017). Psyche is a large object residing within the Main Asteroid Belt at approximately 3 Astronomical Units (AU). The asteroid is unlike any other body in our Solar System. Observations from Earth using radar, occultations, lightcurve inversions and reflection spectra have led to the hypothesis that Psyche may be almost entirely composed of metal (Hanuš et al., 2017, Shepard et al., 2016). This would make Psyche the largest M-type asteroid of our Solar System, which opens up a world full of questions regarding its formation history, connection with other Solar System bodies and its current state. Planetary formation models show that bodies with a similar size to Psyche are likely to be differentiated, meaning that heavier materials such as metals sink to the core of the body and silicates form the mantle. Surprisingly, Psyche's density is too high to conform with the existence of a significant silicate mantle and its reflection spectra show similarities with metal bodies. Consequently, the leading hypothesis is that Psyche is a remnant of a planetary formation process and that multiple impacts stripped away its silicate mantle after differentiation, leaving an exposed core. By investigating this unusual body, we can learn more about the formation of our Solar System and the cores of rocky planets such as Earth (Oh et al., 2016).

The trajectory design of the Psyche mission in the vicinity of the body shows great similarities with the Dawn mission, which successfully explored asteroids Ceres and Vesta. Four quasi-circular orbits are proposed to explore the asteroid. Each orbit has a radius smaller than the previous one, getting closer to the surface of the asteroid as the mission progresses and the gravity field of the asteroid is mapped in greater detail (Oh et al., 2017). A major challenge in the design of trajectories close to irregular bodies such as Psyche is the selection of orbits which are stable. Due to large gravity-field perturbations, orbital parameters can vary significantly over relatively short time spans, possibly resulting in a spacecraft impact on the asteroid surface or an escape from the system (Hu and Scheeres, 2004). Therefore, it is essential to characterize stability in the vicinity of Psyche in order to ensure safe mission operations. In addition, by providing a general characterization of stability in the uniformly rotating two-body problem, the obtained results can be applied to a large number of small bodies beyond the Psyche asteroid as well.

In recent years, research has focused significantly on the search for periodic orbit solutions in the body-fixed frame of small bodies (Hu and Scheeres, 2008, Yu and Baoyin, 2012) by using techniques such as differential correction (Russell, 2006) and Poincaré maps (Scheeres, 1999a). These methods can provide quasi-stable periodic solutions and look at stability from a dynamical systems

point of view. Hu and Scheeres (2004), Araujo et al. (2015) and other authors analyzed stability from a more practical point of view, which is deemed more applicable and useful for the majority of space exploration missions. From a mission perspective, the orbital parameters of orbits should remain bounded between a certain range of values for an extended period of time to ensure that the spacecraft does not undergo excursions to unwanted regions around the small body. During the literature study preceding this research, gaps were found in literature concerning the analysis of stable orbits from this practical point of view. Scheeres (2012) postulates that a second degree and order gravity field captures the most important perturbations in the vicinity of a small body, but it is unclear whether this low-order field is sufficiently complex to globally characterize stability near an irregular body. To the best of the author's knowledge, an extensive parametric numerical characterization of stability in the uniformly rotating two-body problem is lacking from literature. Finally, it was identified that it is uncertain whether chaos indicators, such as the Fast Lyapunov Indicator (FLI), can be used effectively to characterize stability near an irregular body and what their advantages and disadvantages are for globally characterizing stability. Consequently, the research objective of this study is to provide recommendations to mission designers at the Jet Propulsion Laboratory (JPL), regarding how to select stable science orbits in the vicinity of the Psyche asteroid by numerically determining stability regions, while taking into account uncertainties in the gravity field model and providing an assessment on the effectiveness of FLIs for the determination of stability. Based on this research objective and the identified gaps in literature, three research questions can be formulated:

1. Which orbits around the Psyche asteroid are stable and robust against uncertainties in the gravity field?
2. Can a second degree and order gravity field be used to globally characterize stability near a small body?
3. Are chaos indicators, such as the FLI, an effective tool for characterizing orbit stability?

By answering these questions, significant contributions will be made to the field of small-body dynamics in general and the Psyche mission in particular.

The outline of this thesis is as follows. Firstly, Chapter 2 gives a background on asteroids, the Psyche asteroid and the Psyche mission. Secondly, the physical model used in the orbit simulations along with the equations of motion are introduced in Chapter 3. After that, the system is analyzed in an analytical way in Chapter 4 by deriving analytical solutions of the equations of motion. The external software, the numerical integrator and the software architecture are described in Chapter 5. Subsequently, Chapter 6 presents the methodology and results of an extensive parametric numerical characterization of stability in the small-body problem with results applied to the Psyche mission. Then, stability is characterized by applying the FLI in Chapter 7. In this chapter, it will be assessed whether a chaos indicator is an effective tool to characterize stability. Finally, the simulations and results are validated in Chapter 8, after which conclusions and recommendations are presented in Chapters 9 and 10 respectively.

2 Mission Background

To support answering the research objective, this chapter provides background information on asteroids, the Psyche asteroid and the Psyche mission. Firstly, Section 2.1 gives a brief overview of asteroids in general, after which Section 2.2 focuses specifically on the Psyche asteroid. Then, the Psyche mission will be described in Section 2.3, including relevant information on its objectives, spacecraft and trajectory design.

2.1. Asteroids

Asteroids are a taxonomic subset of small bodies that reside within our Solar System and are defined as minor planets which do not experience visible outgassing (Scheeres, 2012, p. 25), although a strict definition is always ambiguous and arbitrary. Other subsets of small bodies include moons (or natural satellites) of planetary bodies, Oort Cloud objects, Kuiper Belt objects, dwarf planets and interplanetary dust. Asteroids are often considered to be the remnants of Solar System formation and therefore carry great scientific value. By exploring these pristine worlds, it is deemed that one can attain a greater understanding of the history and formation of the Solar System. In addition, asteroids have gained an increased amount of attention in recent years due to the possible exploitation of these objects for scarce natural resources.

The most common way to subdivide asteroids further is to classify them based on their orbital parameters. Figure 2.1 (Scheeres, 2012, p. 27) shows the distribution of asteroids within the Solar System. Most asteroids reside within the Main Asteroid Belt between the orbits of Mars and Jupiter. In the figure, the Kirkwood Gaps caused by resonances with Jupiter's orbit are clearly visible. Other notable families of asteroids are the Trojans (residing in the vicinity of Jupiter's fourth and fifth Lagrange points), the Centaurs (residing between the orbits of Jupiter and Neptune) and the Near-Earth Asteroids (with orbits in proximity of Earth's orbit).

Another property used to classify small bodies is their spin state, which is often determined from variations in light curves. This property is especially relevant to the current research since the spin state of the body can severely influence the dynamics in the vicinity of the body. Three main classes can be identified: uniform rotation, complex rotation and synchronized rotation, with the latter class only being applicable to multi-body systems (Scheeres, 2012, p. 35). The majority of the asteroids are uniform rotators with their angular momentum vector being approximately constant in magnitude and orientation within an inertial frame and aligned with the principal moment of inertia of the body. This is expected since it results in the lowest energy state of the body, whereas complex rotation causes tidal energy dissipation. Apart from the type of spin state, one can also

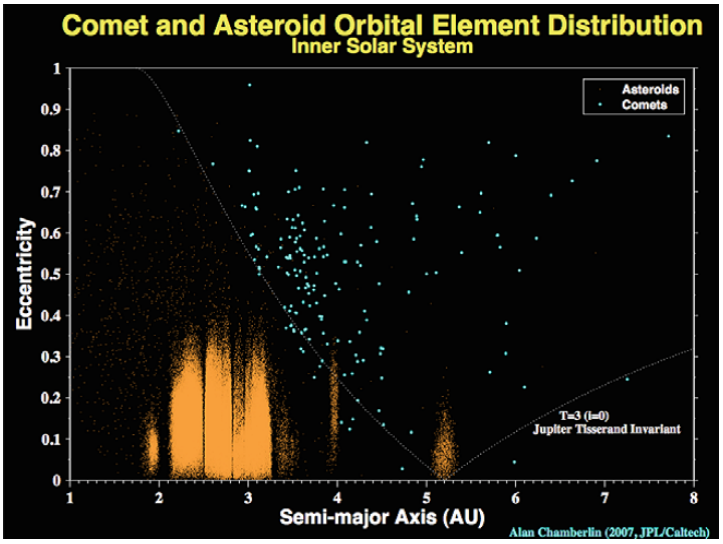

Figure 2.1: Distribution of asteroids and comets within the Solar System based on orbital characteristics. Image courtesy: Alan Chamberlain, JPL/Caltech and retrieved from (Scheeres, 2012, p. 27).

classify bodies based on the magnitude of their rotational rate (Scheeres, 2012, p. 35).

Finally, asteroids can be subdivided based on their spectral features which give indications on their composition. A common subdivision is the following (DeMeo et al., 2015):

- **C-complex**: Asteroids associated with a carbonaceous chondrite composition due to low albedo's, flat or low spectral slopes and subtle to no spectral features. This group contains the C-type asteroids, which make up more than 75 percent of all asteroids.
- **S-complex**: Asteroids associated with a silicate composition due to silicate absorption features within its spectra. These asteroids are assumed to be 'stony' and make up approximately 17 percent of the asteroids.
- **X-complex**: Asteroids with moderate spectral slopes, subtle to no spectral features and low to high albedo's. This complex can be broken down further into E-, M- and P-types, ranging from high to low albedo's respectively. The M-type asteroids are also known as the metallic asteroids and form the third largest group of asteroids.

Note that there are multiple classes that do not fit these complexes such as the very red D-type asteroids and the olivine A-type asteroids.

2.2. Psyche

Using ground-based observations, several studies have indicated that Psyche could be the largest metal-rich (M-type) asteroid in the Main Asteroid Belt (Sanchez et al., 2017). It measures approximately 200 km across and contains 1% of the mass of the Main Asteroid Belt (Shepard et al., 2016), making it a large and massive asteroid. Estimates of the asteroid's density, analysis of its reflection spectra and radar observations characterizing its albedo and size, indicate that Psyche could be composed almost entirely of Fe-Ni metal. Due to its size, density and estimated composition, it is hypothesized that Psyche is the remnant of a planetary formation process. It is thought to be the exposed core of a small planet that never formed, unable to complete its accretion process into a regular planet. This would have been the result of multiple impacts on the asteroid during the formation of the Solar System, which stripped away any silicates encapsulating its core. Therefore, the

asteroid is the target of the Psyche mission which can provide valuable insight in planetary formation and planetary interiors. Furthermore, it is the only body in the Solar System that could provide this kind of information since no other known bodies with a similar composition have a size comparable to Psyche (Oh et al., 2016).

2.2.1. Orbital Parameters

The orbital parameters of the Psyche asteroid are known with high accuracy and are summarized in Table 2.1 along with the orbit period of Psyche around the Sun, the siderial rotation period of the asteroid and the rotational rate (JPL, 2018). Furthermore, Psyche rotates uniformly and it is assumed that it does so about its principal moment of inertia axis.

Parameter	Value	Units
a	2.928	AU
e	0.1339	-
i	3.095	deg
Ω	150.2	deg
ω	227.9	deg
M	210.5	deg
T	5.0138	yr
T_s	4.1939	hr
ω_A	$4.1616\ 10^{-4}$	rad/s

Table 2.1: Orbital elements of Psyche at epoch 2458200.5 (23 March 2018) TDB (JPL, 2018).

Going from top to bottom in the table above, the symbols represent the semi-major axis, the eccentricity, the inclination, the right ascension of the ascending node, the argument of periapsis, the mean anomaly, the rotation period of Psyche around the Sun, the siderial rotation period of Psyche about its rotation axis and the uniform rotational rate of Psyche.

2.2.2. Mass

Several studies have attempted to determine the mass of the Psyche asteroid using astrometric measurements. By tracking encounters of Psyche with smaller asteroids and fitting a two-body problem to the observations, estimates can be obtained of the mass of the asteroid. Then, these estimates can in turn be used to determine a single weighted average of the asteroid's mass. Estimates of Psyche's mass were summarized by Baer et al. (2011) and showed mass estimates ranging from 0.87 10^{-11} to 3.38 10^{-11} solar masses by different studies. However, the approach mentioned earlier is only a first approximation since the asteroid encounters are not isolated. By solving simultaneously for the mass of the asteroid and the epoch state vector(s) of the asteroid, the accuracy of asteroid mass estimates can be increased. Baer and Chelsey (2017) implemented this technique for simultaneous mass determination for gravitationally coupled asteroids and obtained a more precise mass estimate M for the Psyche asteroid, which is listed in Table 2.2 (Baer and Chelsey, 2017) along with Psyche's gravitational parameter μ. This mass estimate is currently also used by Psyche's mission design team. The 1:1 resonance radius r_s of the mean motion of an orbiting body with the asteroid rotation of Psyche can be determined with μ and T_s and is presented in Table 2.2 as well.

2.2.3. Shape

Several methods exist to obtain shape models of asteroids from Earth observations. The most common methods are radar observations, Adaptive Optics (AO) images, lightcurve shape model inversions and occultations. Multiple attempts have been made to construct shape models of the Psyche

Property	Value	1σ Uncertainty	Units
M	$2.29\ 10^{19}$	$7.0\ 10^{17}$	kg
μ	1.53	0.047	km^3/s^2
r_s	207	6.3	km

Table 2.2: Mass, gravitational parameter and 1:1 resonance radius of the Psyche asteroid (Baer and Chelsey, 2017).

asteroid using these techniques. Kaasalainen et al. (2002) developed the first convex shape model of Psyche using lightcurve inversions. Since then, more observations have been made including more accurate radar observations by Shepard et al. (2016) in 2015. The developed shape model compared with these new radar observations is shown in Figure 2.2 (Shepard et al., 2016). Images are presented in groups of three, where the left one is the radar image of Psyche, the middle one is the simulated radar image using the shape model of Psyche and the right one is the shape model of Psyche including its rotation axis.

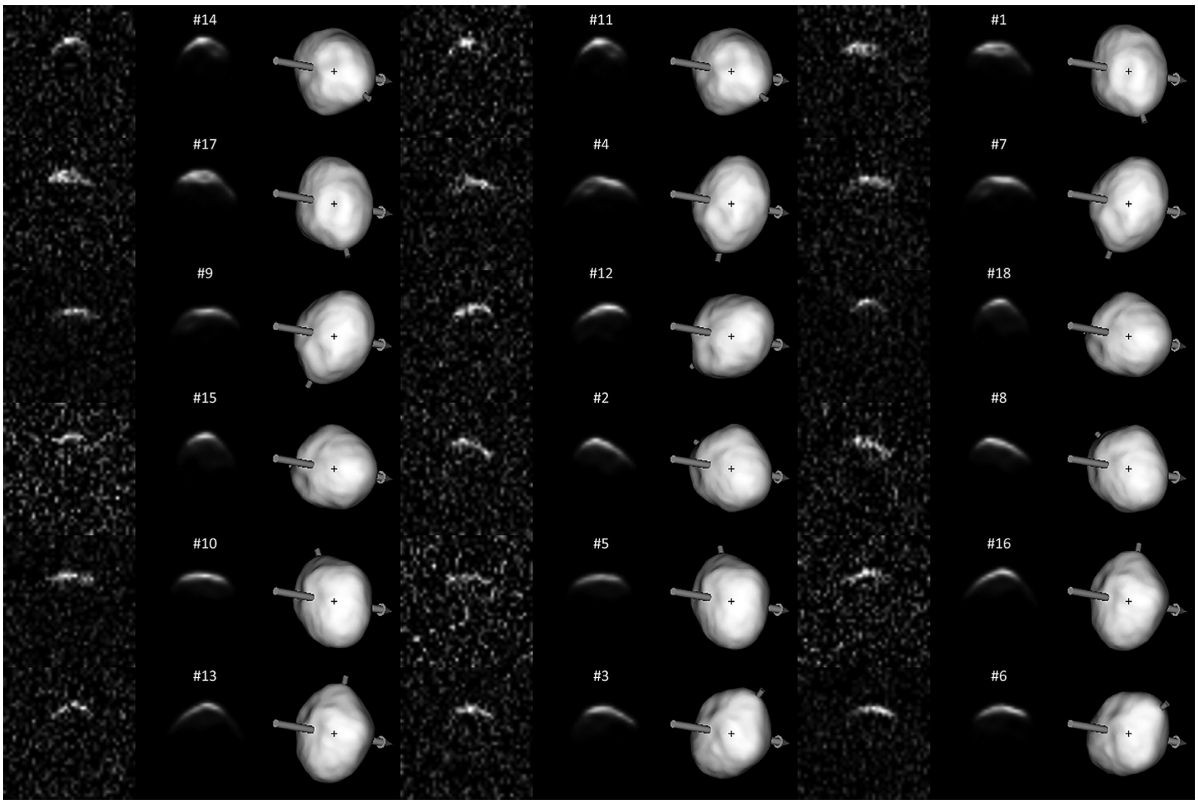

Figure 2.2: Shape model of the Psyche asteroid compared with delay-Doppler radar imaging observations (Shepard et al., 2016). Images are presented in groups of three, where the left one is the radar image of Psyche, the middle one is the simulated radar image using the shape model of Psyche and the right one is the shape model of Psyche including its rotation axis.

The figure presented above clearly illustrates the low resolution of the radar observations, which makes it difficult to generate an accurate shape model of the Psyche asteroid. Hanuš et al. (2017) also developed a shape model, but this one deviates significantly from the other two shape models that were developed for Psyche. Furthermore, Shepard et al. (2016) use a large set of different types of observations and is deemed more reliable for that reason. Their model has been shown to be consistent with previously published AO images and occultations. Several properties of their shape model of the Psyche asteroid are summarized in Table 2.3 (Shepard et al., 2016) and the model itself

is illustrated in Figure 2.3. The model shows that Psyche has an ellipsoidal shape with a mass deficit over a region spanning 90 degrees in longitude.

Property	Value	1σ Uncertainty	Units
R_{mean}	113	12	km
R_{min}	88	9	km
R_{max}	140	14	km
ellipsoidal dimensions	$279 \times 232 \times 189$	$28 \times 23 \times 19$	km

Table 2.3: Shape model characteristics of the Psyche asteroid (Shepard et al., 2016).

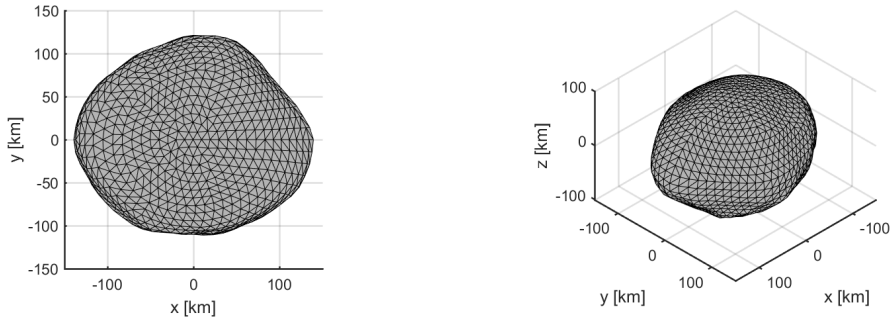

(a) Top view.

(b) Isometric view.

Figure 2.3: Shape model of the Psyche asteroid (Shepard et al., 2016).

2.2.4. Gravity Field

The shape model presented in Subsection 2.2.3 contains large uncertainties, which is expected when analyzing the raw radar images of Figure 2.2. Combined with the mass uncertainty of the asteroid and the fact that it is not possible to derive information on the density distribution within the asteroid, any gravity field derived from the shape model will contain large uncertainties as well. Using the Small-Body Dynamics Toolkit (SBDT) developed by Broschart et al. (2015) in MATLAB©, it is possible to determine the normalized spherical harmonic gravity field coefficients from the polyhedron shape model derived by Shepard et al. (2016) up to and including degree and order 20 and assuming a uniform density distribution.

Here, the nominal gravity field is assumed to be the gravity field corresponding to a uniform-density Psyche asteroid. To account for a possible heterogeneous density distribution, researchers at JPL also generated multiple other spherical harmonics gravity fields assuming density variations within the asteroid. A case resulting in a more irregular gravity field (and larger magnitudes in the spherical harmonic coefficients) would be one with strong density concentrations in the exterior of the asteroid. In this way, more mass is closer to the orbiting spacecraft, causing greater perturbations on its trajectory. Such a gravity field will be used for comparison with the nominal (uniform density) gravity field to study and quantify orbit stability of Psyche's science orbits in a conservative way. Mass concentrated near the center of the asteroid would result in a less irregular gravity field compared to the nominal case.

Both the nominal and the conservative gravity field will be used throughout the stability analysis. In this way, results will be generated based on a realistic and conservative estimate of the spherical harmonic coefficients. To increase computational efficiency, both gravity fields are truncated at degree and order eight since it is assumed that a spherical harmonic degree and order above eight

will be associated with large uncertainties compared to the magnitudes of the coefficients and those of lower degree and order (as will be shown in the next chapter). The values of the zonal and sectoral spherical harmonic coefficients of second degree and order (C_{20} and C_{22}) are given in Table 2.4 for both gravity fields. The reference radius r_e is equal to R_{mean}. For confidentiality reasons, additional spherical harmonic coefficients of Psyche's gravity field are not reported in this thesis.

Coefficient	Nominal	Conservative
C_{20}	-0.1031	-0.1566
C_{22}	0.01910	0.03266

Table 2.4: Spherical harmonic coefficients C_{20} and C_{22} of Psyche's nominal and conservative gravity field with reference radius R_{mean}. The conservative gravity field was generated by the Psyche mission design team at JPL.

2.3. Mission

On January 4, 2017, Psyche was selected as NASA's next mission as part of its Discovery Program. It was selected along with the Lucy mission, which will explore six Trojan asteroids. Both missions competed against 25 other proposals for selection. The Discovery Program aims to develop low-cost and low-risk exploration missions by leveraging flight heritage and commercial partnerships. So far, the program has an extensive list of mission successes, including NEAR Schoemaker, Mars Pathfinder, MESSENGER and Dawn, to name few. Due to the success of the Dawn mission (which completed its science objectives at Vesta and Ceres in 2012 and 2016 respectively), the concept of using Solar Electric Propulsion (SEP) has gained increased attention in recent years. Dawn demonstrated that SEP can be leveraged in favor of other traditional propulsion techniques for planetary science purposes. Of the five final mission proposals for the new round of Discovery Program missions in 2016, Psyche was the only one utilizing SEP, which undoubtedly contributed to its selection. The information presented in this section originates from the work presented by Oh et al. (2016) and Oh et al. (2017) unless stated otherwise.

2.3.1. Objectives

As mentioned before, the Psyche asteroid is one-of-a-kind. Psyche is assumed to be the largest metal-rich asteroid in the Solar System and has not been explored before. The Psyche mission has three main goals: understand how planets are formed by looking at its earliest building block (the core), gain insight in the cores of terrestrial planets by directly observing what is thought to be the exposed core of a small terrestrial planet, and explore a type of world that has never been explored before, namely a metal world. To reach these goals, the Psyche mission has five science objectives:

- Determine whether Psyche is a core, or whether it is unmelted material.
- Determine the relative ages of regions of its surface.
- Determine whether small metal bodies incorporate the same light elements as in the Earth's high-pressure core.
- Determine whether Psyche was formed under conditions more oxidizing or more reducing than Earth's core.
- Characterize the topography and impact crater morphology of Psyche.

2.3.2. Spacecraft

A single spacecraft will be sent to the asteroid to explore this mysterious world. To achieve the goal of having a low-cost and low-risk mission, the design of the mission and the spacecraft is robust. This will be accomplished by maximizing flight heritage, the experience of partner organizations

and hardware with a high Technology Readiness Level (TRL). Following in the footsteps of the Dawn mission, Psyche will use SEP throughout its entire life cycle, excluding the need for chemical propulsion. For the power and propulsion subsystem, JPL has partnered with by Space Systems/Loral (SSL), a commercial spacecraft manufacturer. This partnership is illustrated through the current spacecraft architecture in Figure 2.4 (Oh et al., 2016). The goal is to combine the deep-space exploration experience of JPL with the SEP subsystem experience of SSL.

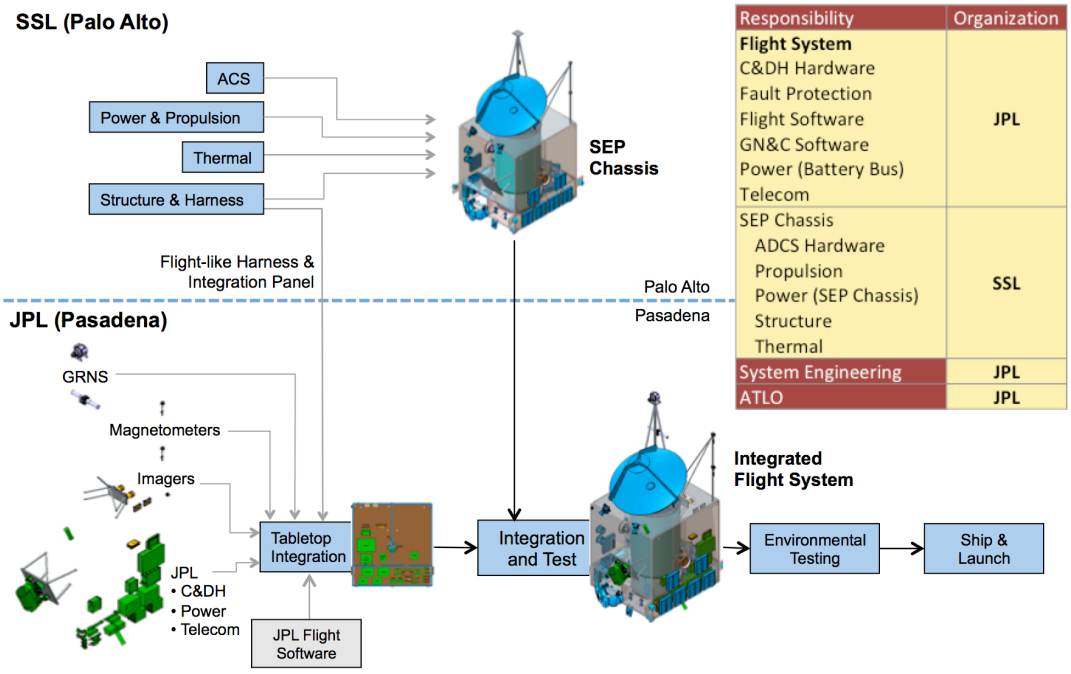

Figure 2.4: Psyche spacecraft architecture (Oh et al., 2016).

Assuming the nominal launch opportunity of August 2022, the spacecraft will approximately have 915 kg of cruise propellant and a delivered mass of 1965 kg at the asteroid. Since the Psyche mission is in its early design stages, these numbers are subject to change. Using an array of five solar panels, the power output at Beginning-of-Life (BoL) at 1 AU is approximately 20 kW. The estimated bus power consumption lies at 780 W. To achieve the science objectives of the mission, the spacecraft has a payload of three remote sensing instruments and uses its X-band communications antenna to conduct radio science. The payload instruments are listed in Table 2.5 (Oh et al., 2017).

Instrument	Flight Heritage	Measurements
Multi-spectral imager	Curiosity Rover Mastcam	Surface geology, composition and topography
Gamma ray and neutron spectrometer	MESSENGER	Key elemental composition and surface compositional heterogeneity
Fluxgate magnetometer	Magnetospheric Multiscale Mission (MMS) and Insight	Magnetic field characterization
X-band antenna	multiple	Gravity field mapping

Table 2.5: Payload of the Psyche spacecraft consisting of three remote sensing instruments and a communications antenna (Oh et al., 2017).

A clear requirement following from the science objectives is that the spacecraft should globally map the surface of the asteroid. The elemental composition observation should be conducted at the lowest altitude possible and at an inclination as close as possible to 90 degrees, which is a challenge for orbit design, especially when considering the irregularities and uncertainties in the environment.

2.3.3. Trajectory Design

Currently, the nominal launch date for the Psyche mission is the 6th of August of 2022. After a 3.6 year cruise and a Mars flyby, the spacecraft should arrive at the asteroid in January 2026. Other launch opportunities exist as well, some of which include additional gravity assists with Earth. However, the 2022 launch opportunity has several advantages compared with the other launch opportunities (Oh et al., 2017):

- The spacecraft does not need to travel to heliocentric distances below 1 AU, which decreases constraints on the thermal subsystem of the spacecraft.
- The spacecraft arrives at Psyche during optimal lighting conditions.
- The cruise time is the shortest of all proposed launch opportunities.

Once the spacecraft arrives at Psyche, it will orbit the asteroid in quasi-circular orbits. In total, four orbits are proposed, with each orbit having a smaller semi-major axis compared to the previous one. In this way, more information on Psyche and its gravity field is obtained as the mission progresses, which allows the spacecraft to be navigated safely when reaching lower and lower altitudes. This strategy has been successfully demonstrated by Dawn at Ceres and Vesta. The spacecraft will operate in the vicinity of the asteroid for 21 months. The first orbit (A) lasts for 56 days during which the magnetometer captures scientific data. Then, the spacecraft will transfer to orbit B during which the topography will be mapped and the spectral imager will be used for 76 days. After that, the spacecraft will transfer to orbit C to capture the gravity field of Psyche in more detail for 100 days. The final mission orbit is D, during which elemental composition observation of the surface will take place for 100 days. Orbits A, B, C and D are illustrated in Figure 2.5 (Oh et al., 2017). Again, this is a preliminary mission scenario and is subject to change before and throughout the mission.

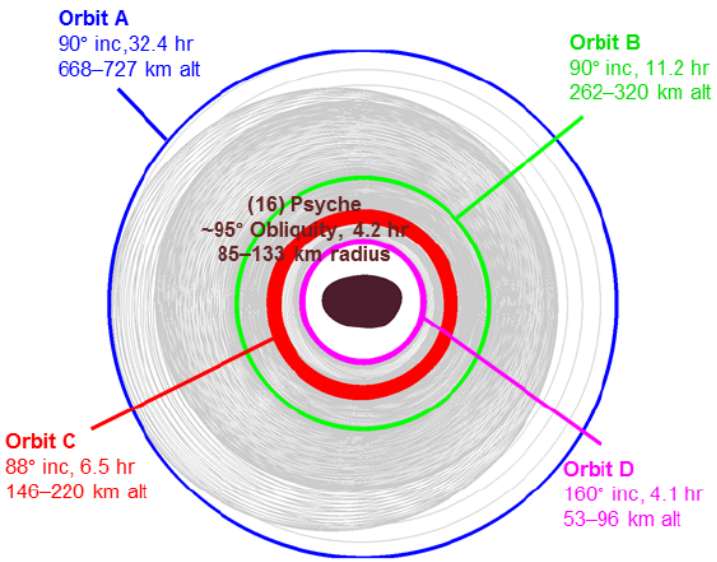

Figure 2.5: Science orbits of the Psyche mission (Oh et al., 2017).

A major challenge in the mission design is the selection of orbits at low altitudes (such as orbits C and D), which are stable for long periods of time. Due to gravity-field perturbations and mean motion resonances with the asteroid rotation, orbit instability can be detrimental for the mission since it can cause the spacecraft to impact or escape the asteroid. Orbits A and B are assumed to be far enough from the asteroid to ensure stability and are both polar Sun-synchronous orbits with repeat ground-tracks. Orbit C is deemed to be the lowest stable polar Sun-synchronous orbit with a repeat ground-track above the 1:1 resonance of the asteroid. Finally, orbit D is deemed stable as well, but has to be inclined to a retrograde orbit to ensure stability. Figure 2.6 shows that orbits B, C and D fall within the stable region according to a preliminary stability analysis (Oh et al., 2017).

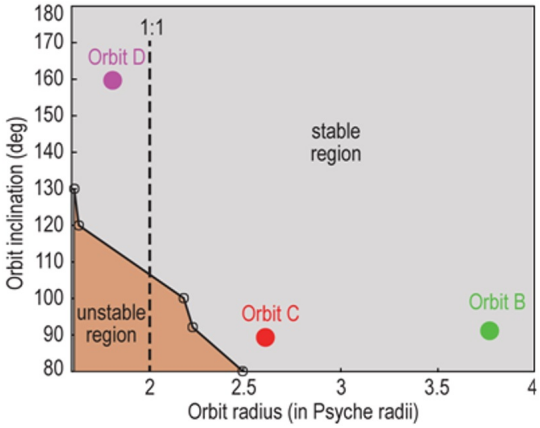

Figure 2.6: Orbit (in)stability as a function of orbit radius and inclination. Results followed from an extensive numerical survey on orbit stability (Oh et al., 2017).

Stability is a major challenge due to the expected irregular shape of the Psyche asteroid and the fact that the gravity field is still very uncertain, which will remain the case until the spacecraft arrives at the asteroid. Consequently, it is essential to select highly stable science orbits in order to minimize the influence of uncertainties in the dynamical environment and the spacecraft state. This approach will also reduce the number of orbit maintenance maneuvers required.

With respect to the Psyche mission in particular, a significant contribution to the mission design will be made by characterizing the stable and unstable regions in the vicinity of the asteroid. This will be done by considering a nominal and a conservative gravity field and an extensive parametric search of the initial condition space using two different notions of stability, namely BIBO-stability and the regularity or chaoticity of orbits. Subsequently, the current mission design can be validated or different (more optimal) orbits can be suggested from the perspective of orbit stability and coverage.

This page is intentionally left blank.

3 Physical Environment

Spacecraft trajectories can only be propagated to a finite accuracy. This chapter will describe the simplified physical environment that will be modeled to simulate the spacecraft trajectories. Firstly, the perturbations in the vicinity of Psyche will be discussed in general in Section 3.1. Then, the perturbations due to the gravity field of Psyche will be described and discussed in more detail in Section 3.2. Finally, the equations of motion are described in Section 3.3. The relevant reference frames and coordinate transformations are described in Appendix A.

3.1. Perturbations

Most often, the main force acting on a spacecraft trajectory is the central gravity of the body which the spacecraft is orbiting. However, this trajectory can be perturbed by irregularities in the gravity field of the body, Solar Radiation Pressure (SRP), third-body gravity and others. Even though most perturbations are small when compared to the central gravity of the body, their influence can be significant over large timescales. Below, each type of perturbation will be analyzed in a first-order and conservative way in order to assess which perturbations should be taken into account in the force model.

Gravity-field perturbations

Due to the irregular shape of Psyche, its gravity field cannot be modeled as a point mass. Since the shape of Psyche is very different from a sphere, it is expected that gravity-field perturbations will significantly influence spacecraft trajectories. To conservatively estimate the effect of gravity-field perturbations, the maximum accelerations due to the zonal spherical harmonic terms J_2, J_4 and J_8 will be determined (note that $J_n = -C_{n0}$). The magnitude of the maximum acceleration due to the n'th J_n term is given by Equation 3.1 and is shown for J_2 in (Wakker, 2015, p. 532).

$$|\boldsymbol{a}_{Jn}|_{max} = (1+n)\mu J_n \frac{r_e^n}{r^{n+2}} \tag{3.1}$$

Here, μ represents the gravitational parameter of the body, r_e is the reference radius of the assumed spherical harmonics gravity field and r is the distance from the spacecraft to the center of the body.

Solar Radiation Pressure

Solar radiation exerts a force on the spacecraft through a momentum exchange between photons and the spacecraft. Impacting photons can either be reflected or absorbed by the surface of the spacecraft. The magnitude of the acceleration caused by solar radiation is given in Equation 3.2 (Wakker, 2015, p. 541).

$$|\boldsymbol{a}_{SRP}| = \frac{C_R W_S}{B_{SC} c} \frac{1}{d^2} \tag{3.2}$$

Here, C_R is the spacecraft's reflectivity (assumed to be 1.4), W_S is the mean solar irradiance at 1 AU, B_{SC} is the spacecraft mass-to-area ratio (assumed to be 20 kg/m^2 similar to the Rosetta mission), c is the speed of light, and d is the distance of Psyche from the Sun in astronomical units (assumed to be equal to Psyche's semi-major axis).

Third-Body Gravity

The gravitational attraction of other celestial bodies can perturb spacecraft trajectories. This is caused by the difference in acceleration exerted on the spacecraft relative to the central body. The magnitude of this relative acceleration is given by Equation 3.3 (Wakker, 2015, p. 540).

$$|\boldsymbol{a}_{TB}| = \frac{2\mu_{TB} r}{d^3} \tag{3.3}$$

In the equation above, μ_{TB} is the gravitational parameter of the perturbing celestial body, r is the radial distance from the spacecraft to the center of the central body and d is the distance from the central body to the third body. The third-body gravity of the Sun and Jupiter will be analyzed, assuming Psyche and Jupiter have circular orbits and a close approach between Psyche and Jupiter occurs.

Other

There are several other perturbations which may influence the trajectories of the spacecraft orbiting Psyche such as particle interactions and electromagnetic forces. In addition, relativistic effects and apparent forces (due to the rotation of Psyche around the Sun) influence the accuracy of the orbit propagations as well. Nevertheless, it is assumed that these effects are negligible compared to the perturbations presented above.

Now, the magnitude of the central gravity and the magnitudes of the perturbing accelerations can be compared as a function of distance from the center of the central body for the Psyche asteroid. Subsequently, it can be assessed which perturbations are relevant for the orbit stability analysis in the vicinity of the asteroid. The relative acceleration of each perturbation with respect to the central gravity of the body is presented in Figure 3.1. The accelerations due to the zonal spherical harmonic coefficients assume the nominal gravity field of Psyche.

From Figure 3.1, it is clear that dynamics in the vicinity of the asteroid are dominated by its gravity field. The largest non-gravitational perturbation is caused by SRP and is more than 4 orders of magnitude smaller when compared to the central gravity. Therefore, non-gravitational accelerations are not included in the force model of the simulations. In addition, the gravity field will not be modeled beyond degree eight. The magnitude of the maximum acceleration due to J_8 is less than 0.5% of the central gravity and less than 2% of the gravity due to J_2 at a radial distance of 150 km. Since it needs to be considered that the gravity field coefficients still contain large uncertainties, terms beyond degree eight can be omitted from the model.

3.2. Gravity Field

3.2.1. Spherical Harmonics

Since gravity is a conservative force, its field can be described by a potential. The gradient of this potential gives the acceleration due to gravity as given in Equation 3.4. Other conventions for the sign of the potential U are used in literature as well.

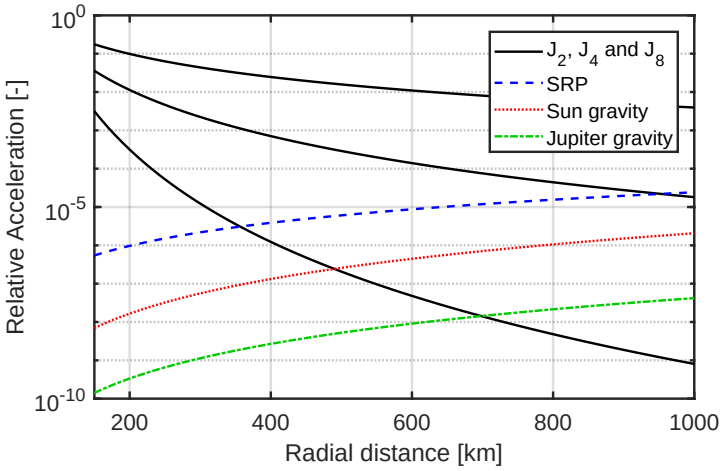

Figure 3.1: Ratio of maximum acceleration for each perturbation with respect to the central gravity acceleration for trajectories near Psyche. The gravity accelerations due to J_2, J_4 and J_8 are shown in the black curves from top to bottom. The x-axis captures all proposed mission orbits. It is assumed that trajectories with radial distances smaller than 150 km are unsafe (R_{max} = 140 km).

$$\boldsymbol{a}_g = \nabla U \tag{3.4}$$

There are various mathematical descriptions available for the gravity potential of a small body. A common one is the polyhedron model originally developed by Werner and Scheeres (1997). When the shape of the body is accurately known, the polyhedron method provides more accurate results when compared to traditional methods, especially close to the surface of the body. The model assumes a uniform-density body and calculates a closed-form solution to Laplace's equation of a polyhedron with triangular faces. Another well-known method is the mass concentration method, which models the body's mass by a series of point masses. Then, the gravity or potential of each point mass can be determined and superimposed with the fields of all other point masses to approximate the total gravitational field of the body as shown by Yu (2016).

Both methods are computationally expensive and require an accurate shape model of the body. This is not the case for the Psyche asteroid and computational power is an important constraint when globally characterizing stability regions. Therefore, the gravity field will be modeled using the well-known spherical harmonics representation, which is computationally efficient (especially when considering a low degree and order gravity field). By separating variables in terms of spherical coordinates, Laplace's equation ($\nabla^2 U = 0$) can be solved. The spherical coordinates are given as a function of Cartesian coordinates in Equations 3.5 through 3.7.

$$r = \sqrt{x^2 + y^2 + z^2} \tag{3.5}$$

$$\sin\delta = \frac{z}{r} \tag{3.6}$$

$$\tan\lambda = \frac{y}{x} \tag{3.7}$$

Here, δ and λ represent the latitude and longitude of the spacecraft position with respect to the central body respectively. The spherical harmonic potential field is given by Equation 3.8 (Scheeres, 2012, p. 43).

$$U = \frac{\mu}{r}\left\{\sum_{n=0}^{\infty}\sum_{m=0}^{n}\left(\frac{r_e}{r}\right)^n P_{nm}(\sin\delta)[C_{nm}\cos m\lambda + S_{nm}\sin m\lambda]\right\} \tag{3.8}$$

In the equation above, n and m represent the order and degree of the spherical harmonics respectively, μ is the gravitational parameter of the body, r is the radial distance from the center of the body, r_e is the reference radius of the spherical harmonic field, P_{nm} are the associated Legendre polynomials and C_{nm} and S_{nm} are the spherical harmonic coefficients that ultimately describe the gravity field. The associated Legendre polynomials can be determined using Equations 3.9 and 3.10 (Hofmann-Wellenhof and Moritz, 2006, p. 14).

$$P_n(x) = \frac{1}{(-2)^n n!}\frac{d^n}{dx^n}(1-x^2)^n \tag{3.9}$$

$$P_{nm}(x) = (1-x^2)^{m/2}\frac{d^m P_n(x)}{dx^m} \tag{3.10}$$

3.2.2. Second Degree and Order Gravity Field

The coefficient C_{00} is equal to 1 for any body. Furthermore, if the center of the coordinate system coincides with the CoM of the body, it can be shown that $C_{11} = S_{11} = C_{10} = 0$. For most gravity fields, this is the case. In addition, relationships exist between the mass moments of inertia of the body and the second degree and order gravity field coefficients. These relations are given in Equations 3.11 through 3.16 (Scheeres, 2012, p. 45) and hold for any body.

$$I_{xx} - I_{yy} = -4Mr_e^2 C_{22} \tag{3.11}$$

$$I_{yy} - I_{zz} = Mr_e^2(C_{20} + 2C_{22}) \tag{3.12}$$

$$I_{zz} - I_{xx} = -Mr_e^2(C_{20} - 2C_{22}) \tag{3.13}$$

$$I_{xy} = -2Mr_e^2 S_{22} \tag{3.14}$$

$$I_{yz} = -Mr_e^2 S_{21} \tag{3.15}$$

$$I_{zx} = -Mr_e^2 C_{21} \tag{3.16}$$

In the equations above, the I's represent the moments of inertia of the body and M represents the mass of the body. For any mass distribution, the coordinate system can be oriented in such a way that all products of inertia are zero such that $S_{22} = S_{21} = C_{21} = 0$. Consequently, the second degree and order gravity field of any small body can be described fully by coefficients C_{20} and C_{22} only.

The second degree and order gravity field is the simplest non-trivial gravity field that can be used to describe the dynamics in the vicinity of an irregular body. It has been shown in several studies in the past that this simple model accounts for the majority of the gravity-field perturbations (Scheeres, 1999b, Scheeres et al., 1996) (see also Figure 3.1). The gravitational potential of the second degree and order gravity field (excluding the central gravity term) is given in spherical and Cartesian coordinates in Equations 3.17 and 3.18 respectively (Scheeres, 2012, p. 45).

$$U_2 = \frac{\mu r_e^2}{r^3}\left[C_{20}\left(1-\frac{3}{2}\cos\delta^2\right)+3C_{22}\cos\delta^2\cos(2\lambda)\right] \tag{3.17}$$

$$U_2 = \frac{\mu r_e^2}{r^5}\left[-\frac{1}{2}C_{20}(x^2+y^2-2z^2)+3C_{22}(x^2-y^2)\right] \tag{3.18}$$

Hu and Scheeres (2004) analyzed stability in the vicinity of a small body using a second degree and order gravity field, but only in the equatorial plane of the body. However, most missions require inclined orbits such that the entire surface of the body can be observed. A part of the research objective is to extend their analysis to consider inclined orbits as well. Throughout the rest of this subsection, the gravity field will be parameterized in an alternative and more convenient way and a normalization will be introduced to remove the dependence on μ and ω_A from the equations of motion. The methods and equations presented throughout the rest of this subsection originate from Hu and Scheeres (2004).

The first step is to introduce a length and time normalization. It is assumed that the body rotates uniformly at a rate ω_A and its mass is defined by the gravitational parameter μ. Then, the total number of independent parameters of the system can be reduced from four (μ, ω_A, C_{20} and C_{22}) to two (C_{20} and C_{22}). The length and time normalizations that are introduced are presented in Equations 3.19 and 3.20 respectively,

$$r_s = (\mu/\omega_A^2)^{1/3} \tag{3.19}$$

$$\tau = \omega_A t \tag{3.20}$$

where r_s is the 1:1 resonance radius of the asteroid and τ is the rotation angle of the asteroid. The reference radius of the spherical harmonic field r_e is here defined as the resonance radius r_s. Finally, by setting $r_e = \mu = 1$ in Equations 3.17 and 3.18, the normalized potential is obtained. The gravity-field coefficients C_{20} and C_{22} normalized with respect to r_s instead of R_{mean} are given in Table 3.1.

Coefficient	Nominal	Conservative
C_{20}	-0.03081	-0.04678
C_{22}	0.005708	0.009758

Table 3.1: Spherical harmonic coefficients C_{20} and C_{22} of Psyche's nominal and conservative gravity fields with reference radius r_s.

Assuming that the z-axis in the body-fixed frame is aligned with the principal moment of inertia of the body, the y-axis is aligned with the intermediate moment of inertia and the x-axis is aligned with the smallest moment of inertia, it follows that $I_{zz} > I_{yy} > I_{xx}$. From this, it can easily be shown that $C_{20} \leq 0$ and $C_{22} \geq 0$ (see Equations 3.11 through 3.13). Similar to Hu and Scheeres (2004), a mass distribution parameter σ can be introduced, which is defined in Equation 3.21.

$$\sigma = \frac{I_{yy}-I_{xx}}{I_{zz}-I_{xx}} = \frac{4C_{22}}{2C_{22}-C_{20}} \tag{3.21}$$

For any body, $0 \leq \sigma \leq 1$. For $\sigma = 0$, the body has rotational symmetry about its z-axis and for $\sigma = 1$, the body has rotational symmetry about its x-axis. In addition, the parameter ν is defined in Equation 3.22.

$$\nu = \frac{I_{zz} - I_{xx}}{Mr_s^2} = 2C_{22} - C_{20} \tag{3.22}$$

In this way, the second degree and order gravity field can be defined completely by parameters σ and ν. The coefficients C_{20} and C_{22} can be written in terms of σ and ν in Equations 3.23 and 3.24 respectively.

$$C_{20} = -\frac{1}{2}\frac{I_{zz} - I_{xx}}{Mr_s^2}(2-\sigma) = -\frac{1}{2}\nu(2-\sigma) \tag{3.23}$$

$$C_{22} = \frac{1}{4}\frac{I_{zz} - I_{xx}}{Mr_s^2}\sigma = \frac{1}{4}\nu\sigma \tag{3.24}$$

Parameters σ and ν can be determined for Psyche using Equations 3.21 and 3.22. Their values are presented in Table 3.2.

Parameter	Nominal	Conservative
σ	0.5406	0.5888
ν	0.04223	0.06630

Table 3.2: Parameters σ and ν of Psyche's nominal and conservative gravity fields.

Since the stability analysis will consider variations in the gravity field of the asteroid, it is useful to place realistic bounds on the magnitudes of C_{20} and C_{22}. Under the assumption that the body is a uniform ellipsoid with semi-major axes $\alpha \leq \beta \leq \gamma$ along its x-, y- and z-axis respectively, the moments of inertia of the body are given in Equations 3.25 through 3.27.

$$I_{xx} = M\frac{\beta^2 + \gamma^2}{5} \tag{3.25}$$

$$I_{yy} = M\frac{\alpha^2 + \gamma^2}{5} \tag{3.26}$$

$$I_{zz} = M\frac{\alpha^2 + \beta^2}{5} \tag{3.27}$$

Now, Equations 3.23 and 3.24 can be rewritten into Equations 3.28 and 3.29 respectively.

$$C_{20} = -\frac{1}{10}\frac{\alpha^2 - \gamma^2}{r_s^2}(2-\sigma) \tag{3.28}$$

$$C_{22} = \frac{1}{20}\frac{\alpha^2 - \gamma^2}{r_s^2}\sigma \tag{3.29}$$

For most asteroids, it holds that $r_s > \alpha$. Otherwise, the asteroid's rotation would be so large that it experiences tensile stress and material on its surface would be accelerated into space. From this condition and using the equations above, the following limits on C_{20} and C_{22} can be placed: $-0.2 \leq C_{20} \leq 0$ and $0 \leq C_{22} \leq 0.05$. Again, it is important to note that these coefficients are normalized with respect to the resonance radius of the body. In addition, it can be shown through proof by contradiction that the upper limit of ν is 0.2 in Equations 3.30 through 3.32.

$$\nu = \frac{I_{zz} - I_{xx}}{Mr_s^2} > 0.2 \tag{3.30}$$

$$M\frac{\alpha^2-\gamma^2}{5}\frac{1}{Mr_s^2}>0.2 \tag{3.31}$$

$$\alpha^2 > r_s^2+\gamma^2 \tag{3.32}$$

Under the assumption that $r_s > \alpha$, the inequalities above are false. Consequently, ν ranges between 0 and 0.2 and σ ranges between 0 and 1 throughout the stability analysis. The relations between gravity coefficients C_{20} and C_{22} and the newly defined parameters are illustrated in Figure 3.2. The nominal and conservative gravity fields of Psyche are mapped onto these figures with a circle and a star respectively.

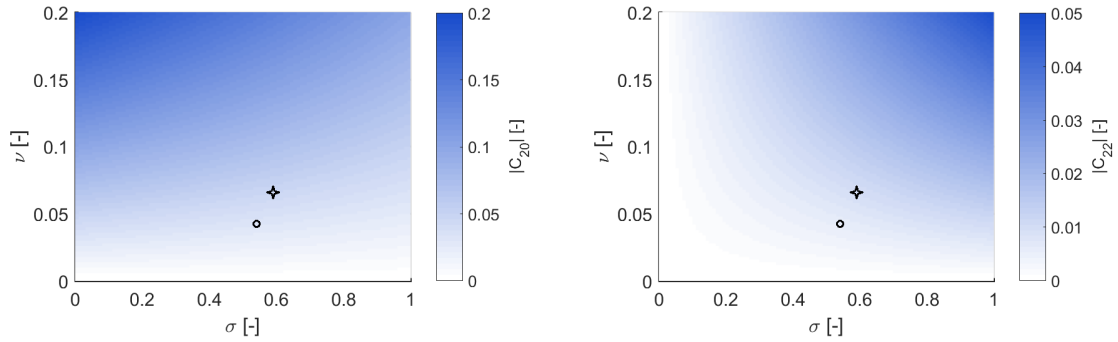

(a) C_{20} as a function of σ and ν.

(b) C_{22} as a function of σ and ν.

Figure 3.2: Magnitude of spherical harmonic gravity coefficients C_{20} and C_{22} as a function of σ and ν. The nominal gravity field is indicated with a black circle and the conservative gravity field is indicated with a black star.

From Figure 3.2, it is clear that large values of ν correlate with large values of C_{20} and C_{22}, and large values of σ correlate with large values of C_{22} and small values of C_{20}.

3.2.3. Higher Degree and Order Gravity Field

The second degree and order gravity field lends itself well to a parametric analysis in terms of variety in the gravity field of a small body since there are only two coefficients that define the gravity field. However, for a stability analysis specifically tailored to the Psyche asteroid, a second degree and order gravity field might not provide the required accuracy. Therefore, the results of the stability analysis using the second degree and order gravity field will be compared to results using an eighth degree and order gravity field. Furthermore, an analysis with a higher degree and order gravity field can also be used to assess the impact of higher degree and order terms on orbital stability.

Since the spherical harmonic coefficients vary greatly in magnitude for most gravity fields, they are often given in normalized form. This is also the case for the gravity field coefficients of Psyche. The relation between the spherical harmonic coefficients and their normalized counterparts is given in Equation 3.33 (Montenbruck and Gill, 2000, p. 58), where δ represents the Kronecker delta function.

$$\begin{Bmatrix}\bar{C}_{nm}\\ \bar{S}_{nm}\end{Bmatrix}=\sqrt{\frac{(n+m)!}{(2-\delta_{0m})(2n+1)(n-m)!}}\begin{Bmatrix}C_{nm}\\ S_{nm}\end{Bmatrix} \tag{3.33}$$

There are many recursion formulas available in literature to calculate the accelerations in x-, y- and z-directions in the body-fixed frame for a given spherical harmonics gravity field. An elegant,

computationally efficient and stable recursive method is outlined in (Montenbruck and Gill, 2000, p. 66-68), which will be used to determine the accelerations caused by the higher degree and order gravity field of Psyche. The method is based upon recurrence relations for the Legendre polynomials. Below, the necessary steps and equations are presented to calculate the accelerations for a position vector in the body-fixed frame (defined by coordinates x, y and z and length r) and an arbitrary gravity field with coefficients C_{nm} and S_{nm}, reference radius r_e and gravitational parameter μ.

The first step is to calculate the intermediate parameters V_{nm} and W_{nm} for all possible combinations of n and m with Equations 3.34 through 3.37 (Montenbruck and Gill, 2000, p. 66-67).

$$V_{mm} = (2m-1)\left[\frac{xr_e}{r^2}V_{m-1,m-1} - \frac{yr_e}{r^2}W_{m-1,m-1}\right] \tag{3.34}$$

$$W_{mm} = (2m-1)\left[\frac{xr_e}{r^2}W_{m-1,m-1} + \frac{yr_e}{r^2}V_{m-1,m-1}\right] \tag{3.35}$$

$$V_{nm} = \frac{2n-1}{n-m}\frac{zr_e}{r^2}V_{n-1,m} - \frac{n+m-1}{n-m}\frac{r_e^2}{r^2}V_{n-2,m} \tag{3.36}$$

$$W_{nm} = \frac{2n-1}{n-m}\frac{zr_e}{r^2}W_{n-1,m} - \frac{n+m-1}{n-m}\frac{r_e^2}{r^2}W_{n-2,m} \tag{3.37}$$

To initialize the recursion, $V_{00} = r_e/r$ and $W_{00} = 0$. Then, the zonal terms V_{n0} can be determined (W_{n0} is zero for all n). After that, the sectoral terms V_{mm} and W_{mm} can be calculated. Finally, the remaining tesseral terms can be calculated as well. The recursion scheme is presented in Figure 3.3 (Montenbruck and Gill, 2000, p. 67).

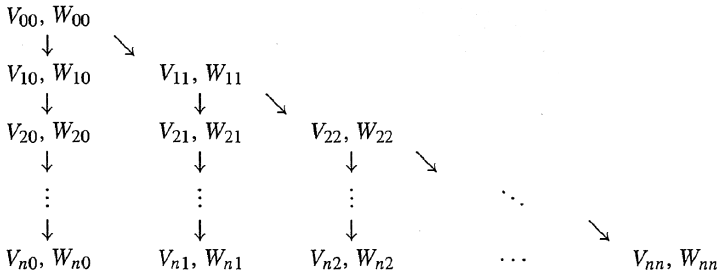

Figure 3.3: Recursion scheme to determine parameters V_{nm} and W_{nm} for all n and m (Montenbruck and Gill, 2000, p. 67).

After determining these intermediate parameters, the gravity field accelerations can be determined as well. The accelerations in x-, y- and z-directions in the body-fixed frame for spherical harmonic degree n and order m are given in Equations 3.38, 3.39 and 3.40 respectively (Montenbruck and Gill, 2000, p. 68).

$$\ddot{x}_{nm} = \begin{cases} \frac{\mu}{r_e^2}\left[-C_{n0}V_{n+1,1}\right], & \text{if } m = 0 \\ \frac{\mu}{r_e^2}\frac{1}{2}\Big[(-C_{nm}V_{n+1,m+1} - S_{nm}W_{n+1,m+1}) \\ \quad + \frac{(n-m+2)!}{(n-m)!}(C_{nm}V_{n+1,m-1} + S_{nm}W_{n+1,m-1})\Big], & \text{if } m > 0 \end{cases} \tag{3.38}$$

$$\ddot{y}_{nm} = \begin{cases} \frac{\mu}{r_e^2}\left[-C_{n0}W_{n+1,1}\right], & \text{if } m = 0 \\ \frac{\mu}{r_e^2}\frac{1}{2}\Big[(-C_{nm}W_{n+1,m+1} + S_{nm}V_{n+1,m+1}) \\ \quad + \frac{(n-m+2)!}{(n-m)!}(-C_{nm}W_{n+1,m-1} + S_{nm}V_{n+1,m-1})\Big], & \text{if } m > 0 \end{cases} \tag{3.39}$$

$$\ddot{z}_{nm} = \frac{\mu}{r_e^2}\left[(n-m+1)(-C_{nm}V_{n+1,m} - S_{nm}W_{n+1,m})\right] \tag{3.40}$$

3.3. Equations of Motion

Newton's equations are the most well-known equations to describe the motion of a spacecraft. Since it is assumed that the only perturbing force on the spacecraft originates from the central body's gravity field, the equations of motion in the inertial frame are described by Equation 3.41.

$$\ddot{\boldsymbol{r}} = \nabla U(\boldsymbol{r}) = -\frac{\mu \boldsymbol{r}}{r^3} + \nabla U_p(\boldsymbol{r}) \tag{3.41}$$

In the equation above, $U_p(\boldsymbol{r})$ is defined as the perturbing gravity potential of the body. Since the potential field is time-independent in the body-fixed frame, it is convenient to express the equations of motion in that frame. Subsequently, the equations of motion are given by Equation 3.42 (Scheeres, 2012, p. 89).

$$\ddot{\boldsymbol{r}} = -\frac{\mu \boldsymbol{r}}{r^3} + \nabla U_p(\boldsymbol{r}) - \dot{\boldsymbol{\omega}}_{\boldsymbol{A}} \times \boldsymbol{r} - 2\boldsymbol{\omega}_{\boldsymbol{A}} \times \boldsymbol{r} - \boldsymbol{\omega}_{\boldsymbol{A}} \times \boldsymbol{\omega}_{\boldsymbol{A}} \times \boldsymbol{r} \tag{3.42}$$

In the equation above, $\boldsymbol{r}$ is defined as the position vector of the spacecraft in the body-fixed frame and $\boldsymbol{\omega}_A$ is the rotational rate vector of the asteroid. Since it is assumed that Psyche is rotating uniformly, the term $\dot{\boldsymbol{\omega}}_A \times \boldsymbol{r}$ disappears.

For a uniformly rotating asteroid, the equations of motion presented above are time-invariant. A useful property is that an integral of motion exists for this set of equations. The Hamiltonian of these equations of motion is an energy integral and is more commonly known as the Jacobi integral defined in Equation 3.43.

$$H(\boldsymbol{r}, \dot{\boldsymbol{r}}) = \frac{1}{2}\dot{\boldsymbol{r}} \cdot \dot{\boldsymbol{r}} - V(\boldsymbol{r}) = \frac{1}{2}\dot{\boldsymbol{r}} \cdot \dot{\boldsymbol{r}} - \frac{1}{2}(\boldsymbol{\omega}_A \times \boldsymbol{r}) \cdot (\boldsymbol{\omega}_A \times \boldsymbol{r}) - U(\boldsymbol{r}) \tag{3.43}$$

In the equation above, $V(\boldsymbol{r})$ is the effective potential in the uniformly rotating frame. The Jacobi integral is constant for a given point mass following a trajectory in the dynamical system described above. More commonly, the Jacobi constant $C_J(\boldsymbol{r}, \dot{\boldsymbol{r}}) = -H(\boldsymbol{r}, \dot{\boldsymbol{r}})$ is used. This conserved quantity can be used to verify whether the equations of motion, the numerical integration scheme and the spherical harmonics gravity field are implemented correctly, by checking that C_J remains constant (round-off and truncation errors may cause C_J to vary slightly).

The expression for the effective potential $V(\boldsymbol{r})$ can be simplified assuming the asteroid rotates about its z-axis such that $\boldsymbol{\omega}_A = [0\ 0\ 1]^T \omega_A$. The simplified expression is given in Equation 3.44.

$$V(\boldsymbol{r}) = \frac{1}{2}\omega_A^2(x^2 + y^2) + \frac{\mu}{r} + U_p(\boldsymbol{r}) \tag{3.44}$$

Similarly, the expression for the equations of motion given in Equation 3.42 can be simplified. In scalar form, the equations of motion are given in Equations 3.45, 3.46 and 3.47.

$$\ddot{x} = 2\omega_A \dot{y} + \omega_A^2 x - \frac{\mu x}{r^3} + \frac{dU_p}{dx} \tag{3.45}$$

$$\ddot{y} = -2\omega_A \dot{x} + \omega_A^2 y - \frac{\mu y}{r^3} + \frac{dU_p}{dy} \tag{3.46}$$

$$\ddot{z} = -\frac{\mu z}{r^3} + \frac{dU_p}{dz} \tag{3.47}$$

To simplify the equations of motion further for the case of the second degree and order gravity field, they will be converted to a set of non-dimensional equations using Equations 3.19 and 3.20 as introduced in Section 3.1. The normalized parameters are $\tilde{\ddot{x}} = \ddot{x}/(r_s\omega_A^2)$, $\tilde{\dot{x}} = \dot{x}/(r_s\omega_A)$, $\tilde{x} = x/r_s$ and $\tilde{r} = r/r_s$. The normalizations for y and z are similar and it is assumed that the potential field is already normalized as described in the previous section. From now on, the tilde symbol will be dropped. The normalized equations of motion using the second degree and order gravity field are presented in Equations 3.48 through 3.50 (Hu and Scheeres, 2004).

$$\ddot{x} = 2\dot{y} + x - \frac{x}{r^3} - \frac{C_{20}x}{r^5} + \frac{5C_{20}x(x^2+y^2-2z^2)}{2r^7} + \frac{6C_{22}x}{r^5} - \frac{15C_{22}x(x^2-y^2)}{r^7} \tag{3.48}$$

$$\ddot{y} = -2\dot{x} + y - \frac{y}{r^3} - \frac{C_{20}y}{r^5} + \frac{5C_{20}y(x^2+y^2-2z^2)}{2r^7} - \frac{6C_{22}y}{r^5} - \frac{15C_{22}y(x^2-y^2)}{r^7} \tag{3.49}$$

$$\ddot{z} = -\frac{z}{r^3} + \frac{2C_{20}z}{r^5} + \frac{5C_{20}z(x^2+y^2-2z^2)}{2r^7} - \frac{15C_{22}z(x^2-y^2)}{r^7} \tag{3.50}$$

The normalized effective potential V of the second degree and order gravity field, and its first- and second-order Cartesian derivatives are presented in Appendix C.

4

Analytical Analysis

Analyzing a system in an analytical manner allows for a deeper understanding of the problem when compared to solely applying numerical techniques. Analytically derived equations and results can also be used to better understand and interpret numerically obtained results and can be used to verify numerical simulations. This chapter deals with such an analytical analysis applied to the uniformly rotating second degree and order gravity field, with a specific focus on the Psyche asteroid.

The shape and orientation of any given orbit around a body are defined by five of its six Keplerian elements: the semi-major axis a, the eccentricity e, the inclination i, the right ascension of the ascending node Ω and the argument of periapsis ω. Two of these elements (a and e) describe the size and shape of the orbit and the others (i, Ω and ω) describe its orientation around the body. For oblate bodies and bodies with small rotational rates, the size and shape of the orbit remain constant on average, whereas its orientation can change over time due to periodic and secular changes in Ω and ω (Hu and Scheeres, 2004). However, for bodies with considerable ellipticity (contained largely in the coefficient C_{22}), it was shown analytically by Scheeres (1999b) that orbits close to the body experience significant short-term non-periodic variations in a and e due to energy and angular momentum exchange with the central body. These large and sudden variations in a and e can result in impact on the body or escape from the system and need to be avoided. Therefore, it is desirable to derive analytical expressions that relate changes in the shape parameters of the orbit (a and e) to initial Keplerian elements and gravity field coefficients.

Approximate analytical expressions will be derived starting from the Gauss Planetary Equations (GPE) for $\frac{da}{dt}$ and $\frac{de}{dt}$. The Lagrange Planetary Equations (LPE) are avoided because of the singularity appearing in the expression of $\frac{de}{dt}$ for e approaching zero. Deriving approximate analytical solutions for a and e will provide crucial insight into the dynamics of the system and can be used to interpret the numerical results presented later on. To the best of the author's knowledge, the derivations presented throughout this chapter are new and have not been presented in literature to this day. Firstly, Section 4.1 presents the necessary assumptions and simplifications used to derive the analytical solutions. Secondly, Section 4.2 starts the derivations with the GPE. After that, solutions of the derivatives of a and e and solutions of a and e are presented in Sections 4.3 and 4.4 respectively. Finally, the analytical results are compared with high-fidelity numerical solutions in Section 4.5.

Another common way to attain a deeper understanding of a dynamical system is to characterize its phase space. A brief characterization of the phase space of Psyche's second degree and order gravity field is presented in Appendix B.

4.1. Assumptions and Simplifications

In order to derive analytical expressions, it is necessary to simplify the problem. Firstly, it is assumed that the results are restricted to orbits in a uniformly rotating second degree and order gravity field with coefficients C_{20} and C_{22}. Secondly, the analysis is restricted to equatorial orbits (prograde or retrograde). Thirdly, the orbits are assumed to have a small initial eccentricity such that second order terms in e can be neglected ($e \ll 1$). Also, it is assumed that a and e do not experience strong variations over short time spans. Finally, averaged short- and long-term periodic variations in a and e are assumed to be negligible. In the following paragraphs of this section, several essential approximations will be introduced.

4.1.1. Second Degree and Order Gravity Potential

The perturbing potential in spherical coordinates was given in Equation 3.17. Since the analytical expressions will restrict themselves to motion in the equatorial plane of the body, the latitude δ can be set to zero. Consequently, Equation 3.17 can be simplified to Equation 4.1.

$$U_2 = \frac{\mu r_e^2}{r^3}\Big[-\frac{1}{2}C_{20} + 3C_{22}\cos(2\lambda)\Big] \tag{4.1}$$

The longitude of the orbiting object with respect the central body λ can easily be expressed in terms of the true longitude of the orbiting object λ_t and the rotational state of the central body for equatorial orbits. An expression for λ is given in Equation 4.2 for prograde (+) and retrograde (−) equatorial orbits.

$$\lambda_\pm = \pm\lambda_t - \omega_A t \tag{4.2}$$

For non-circular orbits, $\lambda_t = \theta + \bar{\omega}$ with $\bar{\omega}$ being the longitude of periapsis. Since it is defined that the central body is uniformly rotating in counterclockwise direction about the z-axis, it adds a negative linear term in t to the longitude of the orbiting body. Equation 4.2 also implicitly assumes that the body-fixed frame and the inertial frame coincide at $t = 0$.

4.1.2. Radial Distance to Center of Body

The distance between a central body and an orbiting object can be expressed by Equation 4.3. A first-order Taylor-series expansion of this expression in e is shown on the right-hand side of the equation,

$$r = \frac{a(1-e^2)}{1+e\cos\theta} = \frac{a}{1+e\cos\theta} + \mathcal{O}(e^2) = a(1-e\cos\theta) + \mathcal{O}(e^2) \tag{4.3}$$

where θ is the true anomaly and $\mathcal{O}$ contains the error made by the Taylor-series approximation.

4.1.3. True Anomaly and Longitude of Periapsis

In order to analytically integrate $\frac{da}{dt}$ and $\frac{de}{dt}$ over time, the true anomaly and the longitude of periapsis need to be expressed as a function of time. To zeroth-order accuracy in e, the true anomaly is equal to the mean anomaly which results in Equation 4.4.

$$\frac{d\theta}{dt} = \frac{dM}{dt} + \mathcal{O}(e) \tag{4.4}$$

The longitude of periapsis $\bar{\omega}$ is defined as the sum of Ω and ω. Consequently, $\frac{d\bar{\omega}}{dt}$ is given in Equation 4.5.

$$\frac{d\bar{\omega}}{dt} = \frac{d\Omega}{dt} + \frac{d\omega}{dt} \tag{4.5}$$

Firstly, the GPE show that $\frac{d\omega}{dt}$ and $\frac{dM}{dt}$ suffer from singularities as the eccentricity goes to zero (Wakker, 2015, p. 609). Secondly, by integrating the expressions above to first order due to the effect of J_2, it can be shown that ω, Ω and M are composed of secular, short-period and long-period terms (Wakker, 2015, p. 616). It is also noted that only zonal harmonic terms (such as J_2) can potentially cause a secular change in these Keplerian elements (Wakker, 2015, p. 624). Therefore, C_{22} does not induce a secular component in any of these elements. In its simplest form, the time history of $\bar{\omega}$ or M can be broken down into its components as illustrated in Figure 4.1.

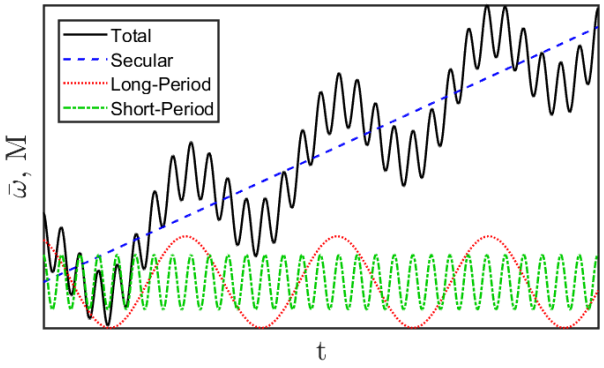

Figure 4.1: Time history of $\bar{\omega}$ or M broken down into its secular, long-period and short-period variations.

Going forward, only secular changes in $\bar{\omega}$ an M will be considered. Averaging $\bar{\omega}$ and M over time without accounting for resonant terms due to C_{22} will cause the long- and short-period oscillations to collapse onto or near the secular term. In addition, it is not possible to include periodic terms of $\bar{\omega}$ and M since this would prohibit the analytical integration of $\frac{da}{dt}$ and $\frac{de}{dt}$ with respect to time. Equations 4.6, 4.7 and 4.8 show the approximate secular terms in $\frac{d\Omega}{dt}$, $\frac{d\omega}{dt}$ and $\frac{d\theta}{dt}$ respectively (Wakker, 2015, p. 624). Furthermore, these equations are first-order accurate in C_{20}. Due to the singularity, the accuracy of these expressions deteriorates as e approaches zero, as it also does for large eccentricities.

$$\frac{d\Omega}{dt} \approx \frac{3}{2} n C_{20} \left(\frac{r_e}{a}\right)^2 \cos i \tag{4.6}$$

$$\frac{d\omega}{dt} \approx -\frac{3}{4} n C_{20} \left(\frac{r_e}{a}\right)^2 (5(\cos i)^2 - 1) \tag{4.7}$$

$$\frac{d\theta}{dt} \approx n \tag{4.8}$$

By summing up and analytically integrating the first-order secular contributions of $\frac{d\Omega}{dt}$ and $\frac{d\omega}{dt}$, a distinction can be made between the prograde and retrograde secular drift in $\bar{\omega}$ ($i = 0$ deg and $i = 180$ deg respectively). Assuming $\bar{\omega} = \bar{\omega}_0$ at $t = 0$, $\bar{\omega}$ is expressed as a function of time in Equations 4.9 and 4.10 for prograde and retrograde orbits respectively. Similarly, Equation 4.11 expresses θ as a function of time assuming $\theta = \theta_0$ at $t = 0$.

$$\bar{\omega}_+ \approx \bar{\omega}_0 - \frac{3}{2} n C_{20} \left(\frac{r_e}{a}\right)^2 t \tag{4.9}$$

$$\bar{\omega}_- \approx \bar{\omega}_0 - \frac{9}{2} n C_{20} \left(\frac{r_e}{a}\right)^2 t \tag{4.10}$$

$$\theta = \theta_0 + nt \tag{4.11}$$

In order to simplify the equations presented in the following sections, a new parameter ψ is introduced in Equation 4.12 for prograde and retrograde orbits. Generally, ψ is close to one and approximates the ratio of the secular rate of change of the true longitude over the mean motion n.

$$\psi_\pm = 1 + 3C_{20}\left(\frac{r_e}{a}\right)^2 \left(-1 \pm \frac{1}{2}\right) \tag{4.12}$$

With the approximations of the true anomaly and the longitude of periapsis, the true longitude can be given as an explicit function time in Equation 4.13 for prograde and retrograde orbits.

$$\lambda_{t\pm} \approx \theta_0 + \bar{\omega}_0 + \psi_\pm nt \tag{4.13}$$

4.2. Gauss Planetary Equations

Now that several essential assumptions and simplifications have been introduced, the focus can be turned to the starting point of the derivation. The GPE for $\frac{da}{dt}$ and $\frac{de}{dt}$ are given in Equations 4.14 and 4.15 respectively (Haranas and Ragos, 2010).

$$\frac{da}{dt} = \frac{2}{n\sqrt{1-e^2}} \left[F_r e \sin\theta + \frac{a(1-e^2)}{r} F_{\lambda_t} \right] \tag{4.14}$$

$$\frac{de}{dt} = \frac{\sqrt{1-e^2}}{na} \left[F_r \sin\theta + \left(\frac{e+\cos\theta}{1+e\cos\theta} + \cos\theta \right) F_{\lambda_t} \right] \tag{4.15}$$

In the equations above, F_r is the acceleration of the orbiting object experienced in radial direction and F_{λ_t} is the acceleration experienced in direction of motion, perpendicular to the radial direction in the orbital plane. Again, the equations above can be simplified by applying a first-order Taylor-series expansion in e. The simplified expressions are given in Equations 4.16 and 4.17 for $\frac{da}{dt}$ and $\frac{de}{dt}$ respectively.

$$\frac{da}{dt} = \frac{2}{n} \left[F_r e \sin\theta + (1 + e\cos\theta) F_{\lambda_t} \right] + \mathcal{O}(e^2) \tag{4.16}$$

$$\frac{de}{dt} = \frac{1}{na} \left[F_r \sin\theta + \left(2\cos\theta + e(\sin\theta)^2\right) F_{\lambda_t} \right] + \mathcal{O}(e^2) \tag{4.17}$$

F_r and F_{λ_t} can be computed by substituting Equation 4.1, solving the partial derivatives and simplifying the expressions. The results are given in Equations 4.18 and 4.19 respectively. Note that the central gravity term is already excluded from the potential since it is well known that a and e remain constant in a point-mass gravity field. Both expressions differentiate between prograde (+) and retrograde (−) orbits.

$$F_{r\pm} = \left(\frac{\partial U_2}{\partial r}\right)_\pm = \frac{3\mu r_e^2}{r^4} \left[\frac{1}{2} C_{20} - 3C_{22} \cos(2\lambda_\pm) \right] \tag{4.18}$$

$$F_{\lambda_t \pm} = \frac{1}{r} \left(\frac{\partial U_2}{\partial \lambda_t}\right)_\pm = \mp \frac{6\mu r_e^2 C_{22}}{r^4} \sin(2\lambda_\pm) \tag{4.19}$$

The equations above can be simplified further by substituting Equation 4.3 and neglecting higher-order terms in e. The simplified expressions for F_r and F_{λ_t} are presented in Equations 4.20 and 4.21 respectively.

$$F_{r\pm} = \frac{3\mu r_e^2}{a^4}(1+4e\cos\theta)\left[\frac{1}{2}C_{20} - 3C_{22}\cos(2\lambda_\pm)\right] + \mathcal{O}(e^2) \tag{4.20}$$

$$F_{\lambda_t\pm} = \mp\frac{6\mu r_e^2 C_{22}}{a^4}(1+4e\cos\theta)\sin(2\lambda_\pm) + \mathcal{O}(e^2) \tag{4.21}$$

4.3. Solutions for $\frac{da}{dt}$ and $\frac{de}{dt}$

Firstly, new parameter χ is introduced, which will greatly simplify equations presented below. χ is defined in Equation 4.22 and is a parameter closely related to the longitude of the orbiting body with respect to the central body.

$$\chi_\pm = 2(\theta_0 + \bar{\omega}_0 + \psi_\pm nt \mp \omega_A t) \approx \pm 2\lambda_\pm \tag{4.22}$$

Now, by substituting Equations 4.20 and 4.21 into Equation 4.16, an expression for $\frac{da}{dt}$ can be obtained in which all state variables can be expressed as a function of time. After substituting, linearizing to first order in e, grouping terms and simplifying using trigonometric properties, Equation 4.23 can be obtained.

$$\begin{aligned}\left(\frac{da}{dt}\right)_\pm \approx -\frac{6\mu r_e^2}{na^4}\Bigg[&2C_{22}\sin(\chi_\pm) \\ &+ e\left(\left(-\frac{1}{2}C_{20} + 3C_{22}\cos(\chi_\pm)\right)\sin\theta + 10C_{22}\sin(\chi_\pm)\cos\theta\right)\Bigg]\end{aligned} \tag{4.23}$$

Similarly, the same can be done to obtain an expression for $\frac{de}{dt}$. The result is presented in Equation 4.24.

$$\begin{aligned}\left(\frac{de}{dt}\right)_\pm \approx -\frac{3\mu r_e^2}{na^5}\Bigg[&\left(-\frac{1}{2}C_{20} + 3C_{22}\cos(\chi_\pm)\right)\sin\theta + 4C_{22}\sin(\chi_\pm)\cos\theta \\ &+ e\left(2\left(-\frac{1}{2}C_{20} + 3C_{22}\cos(\chi_\pm)\right)\sin 2\theta + C_{22}\sin(\chi_\pm)\left(9 + 7\cos 2\theta\right)\right)\Bigg]\end{aligned} \tag{4.24}$$

4.4. Solutions for $a(t)$ and $e(t)$

Using the equations derived in the previous section, it is now possible to obtain analytical expressions for a and e as a function of time. $a(t)$ and $e(t)$ are given in Equations 4.25 and 4.26 respectively assuming $a = a_0$ and $e = e_0$ at $t = 0$.

$$a(t') = a_0 + \int_0^{t'} \frac{da}{dt}dt \tag{4.25}$$

$$e(t') = e_0 + \int_0^{t'} \frac{de}{dt}dt \tag{4.26}$$

Due to the assumptions and simplifications introduced before, it is possible to integrate the equations above analytically. It is not trivial to carry out the integrations by hand and simplify the resulting expressions. Therefore, *Wolfram Mathematica* is used for this purpose. The solution of

$a(t)$ for prograde and retrograde orbits is presented in Equation 4.27. The solution of $e(t)$ for prograde and retrograde orbits is presented in Equation 4.28. Again, it is assumed that changes in a, n and e are small such that they can be treated as constants throughout the integration.

$$\begin{aligned} a(t)_{\pm} \approx a_0 - \frac{3\mu r_e^2}{n_0 {a_0}^4}\Bigg[& 2C_{22}\frac{\cos\left(2(\theta_0+\bar{\omega}_0)\right)-\cos\left(\chi_{\pm}\right)}{\psi_{\pm}n_0 \mp \omega_A} \\ & + e_0\Bigg(C_{20}\frac{\cos\theta-\cos\theta_0}{n_0} \\ & + 7C_{22}\frac{\cos\left(\theta_0+2\bar{\omega}_0\right)-\cos\left(\theta_0+2\bar{\omega}_0+(2\psi_{\pm}-1)n_0t\mp 2\omega_A t\right)}{(2\psi_{\pm}-1)n_0\mp 2\omega_A} \\ & + 13C_{22}\frac{\cos\left(3\theta_0+2\bar{\omega}_0\right)-\cos\left(3\theta_0+2\bar{\omega}_0+(2\psi_{\pm}+1)n_0t\mp 2\omega_A t\right)}{(2\psi_{\pm}+1)n_0\mp 2\omega_A}\Bigg)\Bigg] \end{aligned} \tag{4.27}$$

$$\begin{aligned} e(t)_{\pm} \approx e_0 - \frac{3\mu r_e^2}{2n_0 {a_0}^5}\Bigg[& C_{20}\frac{\cos\theta-\cos\theta_0}{n_0} \\ & + C_{22}\frac{\cos\left(\theta_0+2\bar{\omega}_0\right)-\cos\left(\theta_0+2\bar{\omega}_0+(2\psi_{\pm}-1)n_0t\mp 2\omega_A t\right)}{(2\psi_{\pm}-1)n_0\mp 2\omega_A} \\ & + 7C_{22}\frac{\cos\left(3\theta_0+2\bar{\omega}_0\right)-\cos\left(3\theta_0+2\bar{\omega}_0+(2\psi_{\pm}+1)n_0t\mp 2\omega_A t\right)}{(2\psi_{\pm}+1)n_0\mp 2\omega_A} \\ & + e_0\Bigg(C_{20}\frac{\cos\left(2\theta\right)-\cos\left(2\theta_0\right)}{n_0} + 9C_{22}\frac{\cos\left(2(\theta_0+\bar{\omega}_0)\right)-\cos\left(\chi_{\pm}\right)}{\psi_{\pm}n_0\mp\omega_A} \\ & + \frac{1}{2}C_{22}\frac{\cos\left(2\bar{\omega}_0\right)-\cos\left(2(\bar{\omega}_0+(\psi_{\pm}-1)n_0t-\omega_A t)\right)}{(\psi_{\pm}-1)n_0\mp\omega_A} \\ & + \frac{13}{2}C_{22}\frac{\cos\left(2(2\theta_0+\bar{\omega}_0)\right)-\cos\left(2(2\theta_0+\bar{\omega}_0+(\psi_{\pm}+1)n_0t-\omega_A t)\right)}{(\psi_{\pm}+1)n_0\mp\omega_A}\Bigg)\Bigg] \end{aligned} \tag{4.28}$$

With the expressions for $a(t)$ and $e(t)$, it is also possible to obtain an analytical expression for $r(t)$, which is given in Equation 4.29.

$$r(t)_{\pm} \approx a(t)_{\pm}(1-e(t)_{\pm}\cos\theta) \tag{4.29}$$

The results presented above are notable. After opening the square bracket, $a(t)$ contains one term independent of eccentricity and three terms proportional to e. All terms dependent on C_{22} are singular at specific prograde resonant orbits. The first, third and fourth term approach infinity as the mean motion of the orbiting body gets close to the 1:1, 1:2 and 3:2 resonances with the rotation of the central body respectively. The amplitude of the second term (which depends on C_{20}) does not grow at a particular resonant orbit. This result is expected as it is well known that C_{22} contributes strongly to the instability of orbits. These analytical equations clearly demonstrate the origin of the instabilities and their relation to gravity field coefficients and resonances of the mean motion with the rotation of the central body. It is expected that it will be possible to observe these instabilities at resonant orbits in numerical results. Similarly, $e(t)$ contains three terms independent of eccentricity and four terms proportional to e. Again, singularities appear at resonant orbits for terms proportional to C_{22}. The second, third, fifth and seventh term approach infinity as the mean motion of the orbiting body gets close to the 1:2, 3:2, 1:1 and 2:1 resonances with the rotation of the central body respectively. By including second- and higher-order terms in e and higher degree and order spherical harmonic coefficients, it is expected that more resonances will appear, although it is likely that the resonant orbits presented here cause the strongest instabilities.

To give an indication of the relative importance of the different terms in Equations 4.27 and 4.28, the magnitudes of the amplitudes of the periodic terms are presented below. Tables 4.1 and 4.2 list the amplitudes of the periodic terms in the expressions of the semi-major axis and the eccentricity respectively. These are given for a prograde (i_0 = 0 deg) and a retrograde (i_0 = 180 deg) orbit with initial conditions a_0 = 500 km and e_0 = 0.1 in Psyche's nominal second degree and order gravity field.

Term	1	2	3	4
Prograde Amplitude [km]	1.06	0.79	0.16	0.42
Retrograde Amplitude [km]	0.61	0.79	0.12	0.18

Table 4.1: Amplitudes of periodic terms in Equation 4.27. Values are given for a prograde (i_0 = 0 deg) and a retrograde (i_0 = 180 deg) orbit with initial conditions a_0 = 500 km and e_0 = 0.1 in Psyche's nominal second degree and order gravity field.

Term	1	2	3	4	5	6	7
Prograde Amplitude [10^{-4}]	79.01	2.25	22.73	7.90	4.78	0.20	5.43
Retrograde Amplitude [10^{-4}]	79.01	1.71	9.69	7.90	2.75	0.19	1.64

Table 4.2: Amplitudes of periodic terms in Equation 4.28. Values are given for a prograde (i_0 = 0 deg) and a retrograde (i_0 = 180 deg) orbit with initial conditions a_0 = 500 km and e_0 = 0.1 in Psyche's nominal second degree and order gravity field.

Firstly, it can be observed that the amplitudes of the periodic terms of the retrograde orbit are equal or smaller than those of the prograde orbit. This is expected when analyzing the denominators of Equations 4.27 and 4.28. Secondly, the importance of terms proportional to e_0 is slightly smaller when compared to terms not proportional to e_0. However, it is clear that they still have a relatively large impact. Finally, it is noted that the relative importance of each term changes for different orbits (especially close to resonance) and gravity field coefficients.

4.5. Comparison with High-Fidelity Numerical Integration

Now, the analytical first-order expressions derived in the previous sections will be compared to a high-fidelity numerical simulation. The orbits are propagated in the equatorial plane of Psyche's nominal uniformly rotating second degree and order gravity field for a duration of three orbital periods (of the orbiting object). All orbits are integrated in prograde (i_0 = 0 deg) and retrograde (i_0 = 180 deg) direction with respect to the rotation of the central body with $\bar{\omega}_0$ = 80 deg and θ_0 = 130 deg (arbitrary values).

Orbit	a_0 [km]	e_0 [-]	**Orbit**	a_0 [km]	e_0
a	500	0.01	e	450	0.1
b	500	0.1	f	400	0.1
c	500	0.3	g	350	0.1
d	500	0.5	h	300	0.1

Table 4.3: Initial conditions of orbits a through h in Psyche's uniformly rotating second degree and order nominal gravity field. Each orbit is integrated in prograde (i_0 = 0 deg) and retrograde (i_0 = 180 deg) direction with respect to the rotation of the central body with $\bar{\omega}_0$ = 80 deg and θ_0 = 130 deg for a duration of approximately three orbital periods.

As can be seen in the table above, the semi-major axis and the eccentricity are varied in order to demonstrate when the analytical expressions match the numerical results well and when they break down (for this specific model). It is expected that the approximations are less accurate for smaller

semi-major axes since the orbits will experience stronger perturbations and instabilities closer to the surface of the body. Moderately eccentric orbits are expected to have a similar effect due to low-altitude periapsis approaches and higher-order effects in e. In addition, the phase of the oscillations in orbital elements is expected to be off for small eccentricities due to the singularity for e approaching zero (affecting θ and $\bar{\omega}$). Finally, the analytical expressions are expected to match the numerical results better for retrograde orbits when compared to prograde orbits since they are much more stable and resilient to gravity-field perturbations. Firstly, Figures 4.2 and 4.3 present a detailed comparison of analytical and numerical results for orbit b propagated in prograde and retrograde direction respectively.

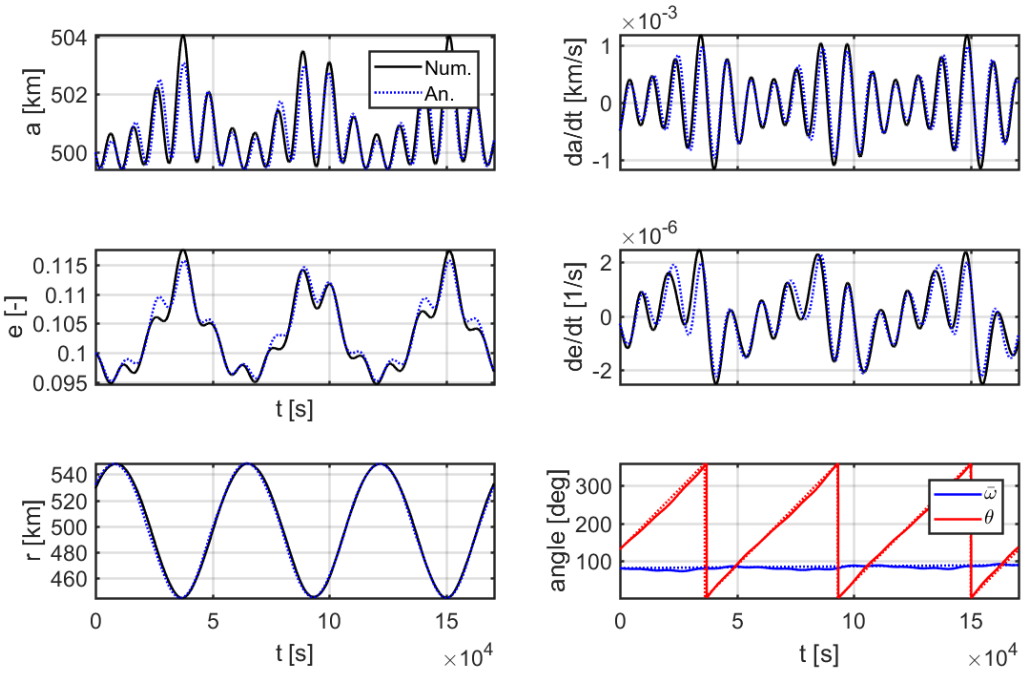

Figure 4.2: Comparison of analytical and numerical results of a, e, r, $\frac{da}{dt}$, $\frac{de}{dt}$, θ and $\bar{\omega}$ for prograde orbit b. The orbit is propagated for approximately three orbital periods and initialized with the conditions presented in Table 4.3.

The figures show that the analytical and numerical results match very well for orbit b. It is clear that the omission of periodic terms in $\bar{\omega}$ and θ does not have a large detrimental impact on the results. Qualitatively, these results demonstrate the validity of the analytical expressions given the assumptions that were introduced. In addition, it can be seen that the analytical results for retrograde orbit b match the numerical results better when compared to prograde orbit b, which was expected. Retrograde orbits are known to be more stable and resilient against mean motion resonances. One way to explain this is the fact that the perturbing frequencies are larger when compared to prograde orbits due to the counter rotation of the orbiting object with respect to the central body, which causes averaging of the perturbations.

Now, a comparison between numerical and analytical results is shown for all orbits listed in Table 4.3. Time histories of the radial distance r are presented in Figures 4.4 and 4.5 for prograde and retrograde orbits respectively. In addition, a more extensive assessment of the analytical results is presented in the form of color plots, where the parameter space of a_0 and e_0 is explored and the Root-Mean-Square (RMS) of the difference in r (between the analytical and numerical results) over three orbital periods is presented. These color plots are shown in Figure 4.6. Again, results

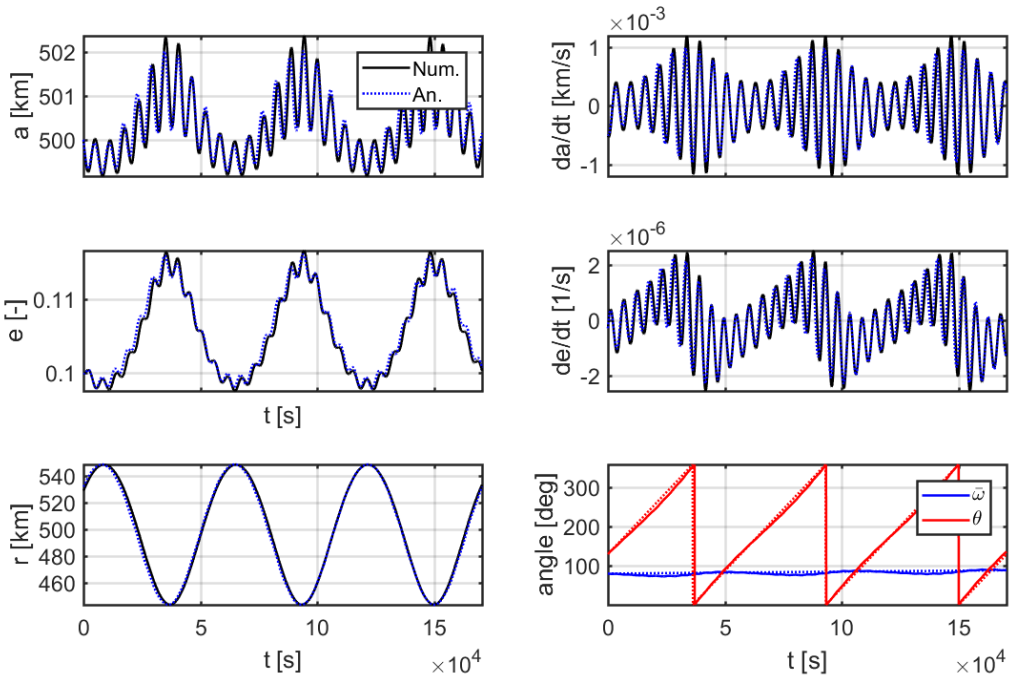

Figure 4.3: Comparison of analytical and numerical results of a, e, r, $\frac{da}{dt}$, $\frac{de}{dt}$, θ and $\bar{\omega}$ for retrograde orbit b. The orbit is propagated for approximately three orbital periods and initialized with the conditions presented in Table 4.3.

are shown considering Psyche's nominal second degree and order gravity field with $\bar{\omega}_0 = 80$ deg and $\theta_0 = 130$ deg.

As expected, the analytical results are accurate for small eccentricities ($e_0 < 0.2$) and generally deteriorate for larger eccentricities for prograde and retrograde orbits. The analytical approximations also become slightly worse for orbits with eccentricities close to zero, due to the singular terms in e for $\bar{\omega}$ and θ. However, increasing the eccentricity has a much more detrimental impact on the accuracy of the analytical solutions as can be seen in Figures 4.4, 4.5 and 4.6. In addition, the analytical solutions for retrograde orbits are more accurate for lower semi-major axes. This is simply due to the fact that the retrograde orbits are much more stable at these low altitudes. The trajectories of prograde orbits become unstable much sooner, such that the analytical approximations cannot describe the orbits anymore. Unsurprisingly, the analytical results for prograde orbits do not match the numerical results as the semi-major axis gets closer and closer to the body (the 2:1 resonance corresponds to a semi-major axis of approximately 330 km). From Figure 4.6, it can be conclude that the analytical solutions match the real solutions well, under the specified assumptions in Section 4.1. Finally, note that an absolute RMS error is presented in Figure 4.6. For larger semi-major axes, the RMS is expected to grow as well. A relative RMS error could have been used as well.

Approximate analytical expressions were derived for the uniformly rotating second degree and order gravity field. Several resonant terms appear in the analytical expressions of the semi-major axis and the eccentricity. Those terms flag instabilities occurring at mean motion resonances with the asteroid rotation for prograde orbits. The equations clearly show that these singularities disappear for retrograde orbits, which will be validated with numerical results later on.

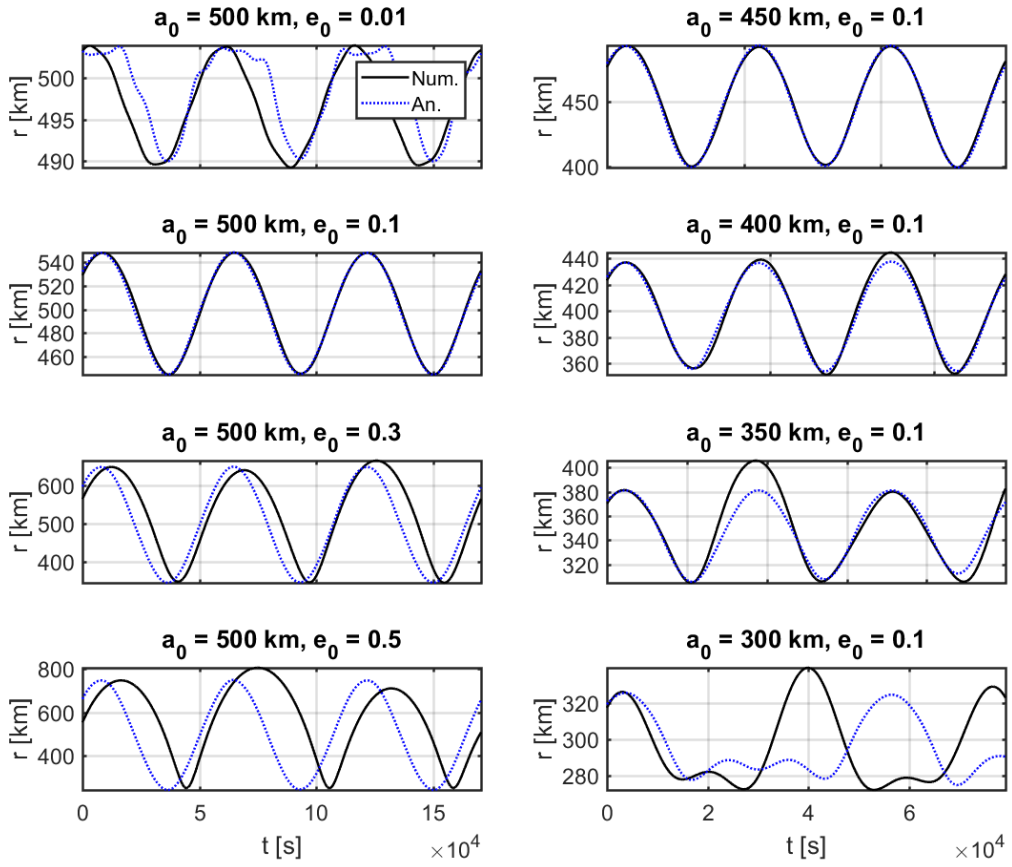

Figure 4.4: Comparison of analytical and numerical results of the radial distance r for all orbits listed in Table 4.3. The orbits are prograde ($i_0 = 0$) and propagated for approximately three orbital periods.

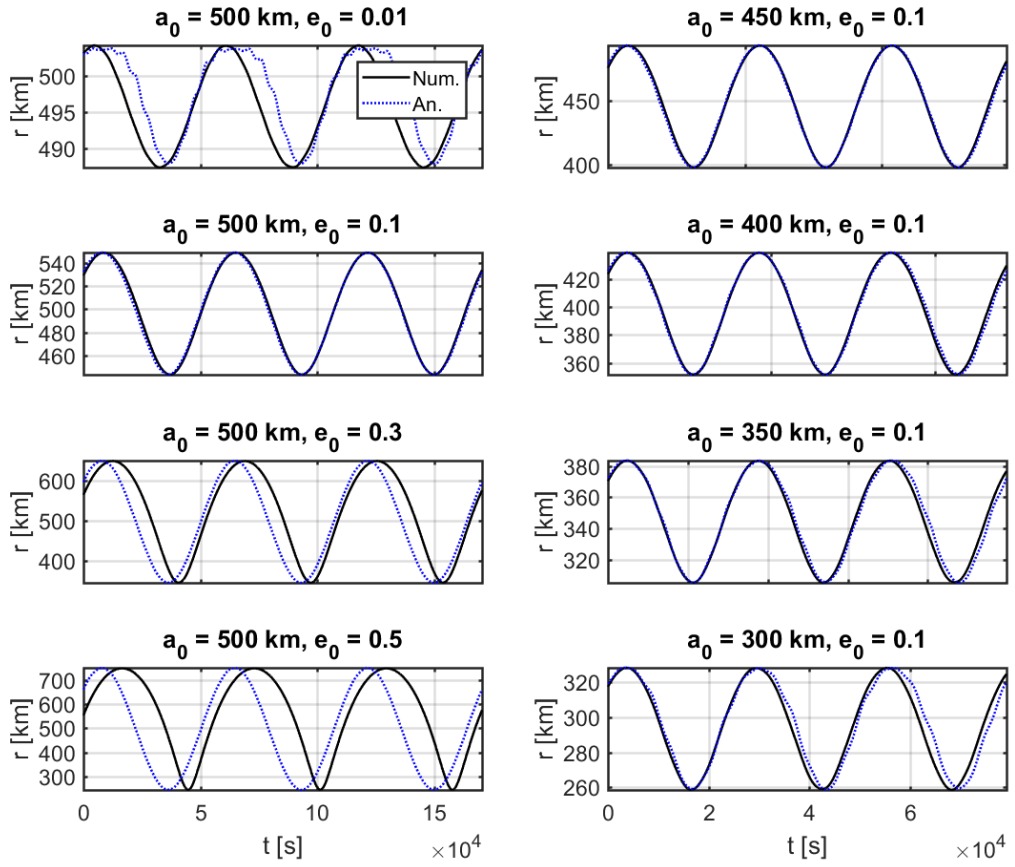

Figure 4.5: Comparison of analytical and numerical results of the radial distance r for all orbits listed in Table 4.3. The orbits are retrograde ($i_0 = 0$ deg) and propagated for approximately three orbital periods.

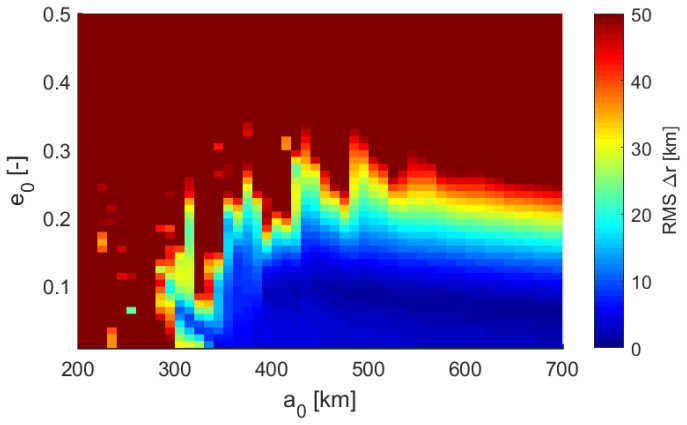

(a) Prograde orbits.

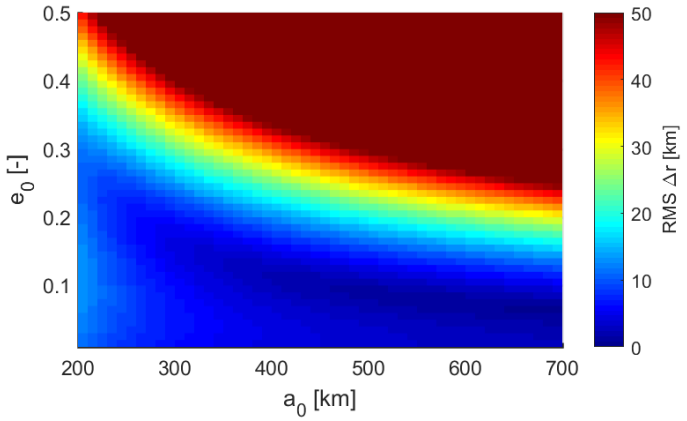

(b) Retrograde orbits.

Figure 4.6: Comparison of analytical and high-fidelity numerical results. The RMS of Δr over three orbital periods (of the orbiting object) is shown for retrograde and prograde orbits. Results are shown for Psyche's nominal second degree and order gravity field with $\bar{\omega}_0 = 80$ deg and $\theta_0 = 130$ deg.

5 Simulator

This chapter will give a description of the software used and developed while carrying out the research. Firstly, Section 5.1 describes the SBDT, which is used for visualization and validation purposes. Then, the numerical integration scheme is selected and described in Section 5.2. Finally, Section 5.3 presents the software architecture by means of software flow diagrams.

The stability analysis tool is developed in C++ using *Microsoft Visual Studio* and the code is executed in parallel on a Linux machine of the Astrodynamics & Space Missions Department at the Faculty of Aerospace Engineering at TU Delft. The machine has a total of two Intel® Xeon® CPU E5-2683 v3 sockets that operate at 2.00 GHz. Each socket consists 14 cores and each core has two threads. 14 out of 56 threads were made available for this research.

5.1. Small-Body Dynamics Toolkit

The SBDT is a MATLAB© toolkit developed by Broschart et al. (2015) of which a significant part has been developed at JPL. It is specifically aimed at providing preliminary mission analysis capabilities around small bodies and is therefore a useful additional software tool for the stability analyses carried out throughout this research. Several of the toolkit's main capabilities are listed below.

- Numerical integration of spacecraft trajectories
- Visualization of trajectories around a small body
- Usage of various gravitational field models: point mass, constant density (polyhedron or ellipsoidal) and spherical harmonics
- Taking into account SRP and comet out-gassing forces
- Handling various sets of equations of motion: two-body, Hill, circular and elliptical restricted three-body problem and four-body problem
- Generation of spherical harmonic coefficients from polyhedron shape models and vice versa
- Propellant budget calculations

The SBDT has many other capabilities as well and has been used for various purposes including orbit stability analysis, designing control laws for hovering spacecraft at asteroids, analyzing planetary defense strategies, autonomous spacecraft navigation strategies, etc. Furthermore, the SBDT has been used for at least eight NASA Discovery and New Frontiers proposals (Broschart et al., 2015).

Here, the tool is used exclusively for the following purposes.

- Visualization of spacecraft trajectories in the vicinity of the Psyche asteroid
- Numerical integration of the spacecraft trajectories in the body-fixed frame of the uniformly rotating second and eighth degree and order gravity fields (for validation purposes)
- Generation of spherical harmonic coefficients corresponding to the shape model of the Psyche asteroid (Shepard et al., 2016) assuming uniform density (nominal gravity field)

Unsurprisingly, the nominal spherical harmonic gravity generated using SBDT and the one provided by Psyche's mission design team match exactly.

5.2. Integrator

Instead of developing a numerical integration scheme purposely, use is made of an existing and well-know library in C++. This approach saves valuable time and energy. *odeint* is a free and open-source C++ library that offers the capability of numerically integrating sets of Ordinary Differential Equations (ODEs). The library is distributed under the peer-reviewed Boost Software License and was originally developed by Ahnert and Mulansky (2011). Its main goal "is to provide a modern and fast C++ library for solving the Initial Value Problem (IVP) of ODEs" and its software design approach emphasizes container independence, operation independence, high performance and generality.

Currently, *odeint* contains 21 numerical integration schemes. However, many of these (such as the explicit Euler or the implicit Euler) can easily be ruled out as viable candidates due to their weak performance in astrodynamics applications. In a literature study preceding this research, several favorable characteristics of a suitable numerical integration scheme were identified:

- **Explicit**: Implicit integration schemes depend on the current state and a state at a later time. Therefore, they require the non-analytical solution of a set of complex equations, which are often solved iteratively. Consequently, implicit methods require more function evaluations per step when compared to explicit methods. However, the main advantage of these methods is that they are more stable and therefore preferred when solving stiff ODEs. Since the equations of motion at hand are generally non-stiff (no large discrepancies between slow and fast dynamics), an explicit integration scheme is preferred for its efficiency.
- **Single Step**: Multistep methods rely on states before the state at the current step and take advantage of that information. The accuracy of the multistep method increases with the number of past states used in the integration scheme. Generally, classical multistep methods are not preferred for long-duration numerical integrations of Hamiltonian systems (Hairer et al., 2006, p. 566). Single-step methods are often more efficient for the same accuracy. Multistep methods are most useful when function evaluations are very costly, which is not the case here due to the low degree and order gravity fields used. Therefore, single-step methods are preferred over multistep methods.
- **Variable Step Size**: For the majority of applications in astrodynamics, variable step size integrators are preferred. For example, when considering an elliptic orbit around an asteroid, smaller step sizes are required during periapsis when compared to apoapsis since the spacecraft state varies more strongly and rapidly during periapsis. Therefore, the integration scheme preferably has a variable step size.

Considering the properties listed above, the majority of the 21 integration schemes of *odeint* can be ruled out. The remaining candidates are listed in Table 5.1.

Class	Family	Type
runge_kutta_dopri5	Runge-Kutta	Dormand-Prince 5(4)
runge_kutta_cash_karp54	Runge-Kutta	Cash-Karp 5(4)
runge_kutta_fehlberg78	Runge-Kutta	Fehlberg 7(8)
bulirsch_stoer	Bulirsch-Stoer	variable order

Table 5.1: Numerical solvers for ordinary differential equations provided by the *odeint* library in C++ (Ahnert and Mulansky, 2011). These numerical integration schemes are the only ones which are explicit, single-step integrators with a variable step size.

To select the most suitable integrator (high accuracy for lowest computational effort), the performance of the four integrators listed in Table 5.1 is compared. For each integrator, the final integration time is plotted as a function of the error in Jacobi constant, which is supposed to remain constant for the considered dynamical system. An orbit in Psyche's uniformly rotating second degree and order gravity field is integrated 11 times for each integrator for a duration of 90 days. For each integration, the absolute and relative error tolerances are varied. The results are presented in Figure 5.1 by means of a logarithmic plot. Here, the integrations are carried out on a laptop computer so overall performance is low.

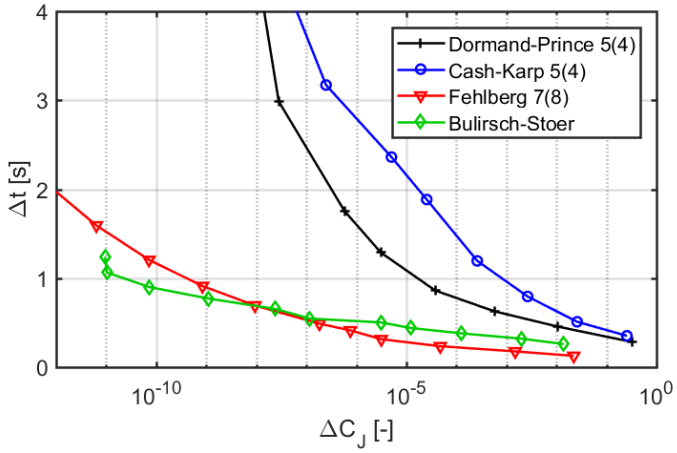

Figure 5.1: Performance of several numerical integration schemes provided by *odeint*. An orbit in Psyche's uniformly rotating second degree and order gravity field is integrated for 90 days on a laptop computer. C_J is normalized with Equations 3.19 and 3.20.

It can be observed that the Runge-Kutta Fehlberg 7(8) (RKF78) is the most suitable integrator for accuracies $\Delta C_J < 10^{-8}$ over 90 days and the Bulirsch-Stoer integrator is most optimal for higher accuracies. Since ΔC_J is normalized, this roughly corresponds to eight digit accuracy (~cm accuracy), which is much more than required for the integrations performed in this research. Consequently, RKF78 is selected as the integration scheme. Due to the normalization, the absolute and relative error tolerances can be set equal to each other. Their values are set at 10^{-9} such that $\Delta C_J \approx 10^{-7}$ over 90 days (~m accuracy). This accuracy is still higher than required by one or two orders of magnitude to remain conservative. The resolution of the uniform sampling presented in the following chapter will provide additional justification for the selection of this accuracy.

5.3. Software Architecture

Before starting on this section, the reader is referred to Chapters 6 and 7. These chapters present the methodology, results and discussion of the numerical stability analyses using BIBO- and FLI-

stability conditions respectively. It is recommended to read these chapters first in order to better understand the flow diagrams presented in this section.

The software architectures of the stability analysis tools are modular and simple. As mentioned before, the majority of the code is developed in C++, with data visualization and validation done in MATLAB©. Many initial conditions are sampled in the BIBO-stability analyses *A*, *B* and *C*. For a single orbit, the software flow diagrams are presented in Figures 5.2, D.1 and D.2 respectively.

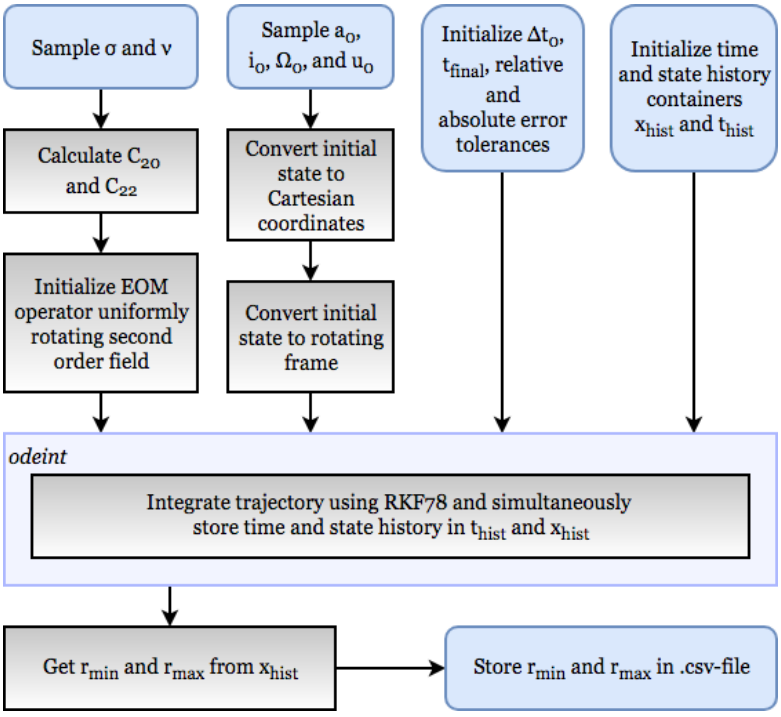

Figure 5.2: Flow diagram of sampled orbit in BIBO-stability analysis A.

Since the flow diagrams of analyses *B* and *C* are very similar to those of analysis *A*, they are shown in Appendix D. Figure 5.2 shows the flow diagram of a single sampled orbit. Due to the accessibility of 14 threads on a Linux computer, for-loops sampling the search space can be executed in parallel which decreases computation time. As can be seen in the diagram, the minimum and maximum radii of the orbit are stored in .csv-files. These files can later be accessed by scripts developed in MATLAB© to generate the required stability plots. Finally, the flow diagram of the FLI-stability analysis is shown in Figure 5.3.

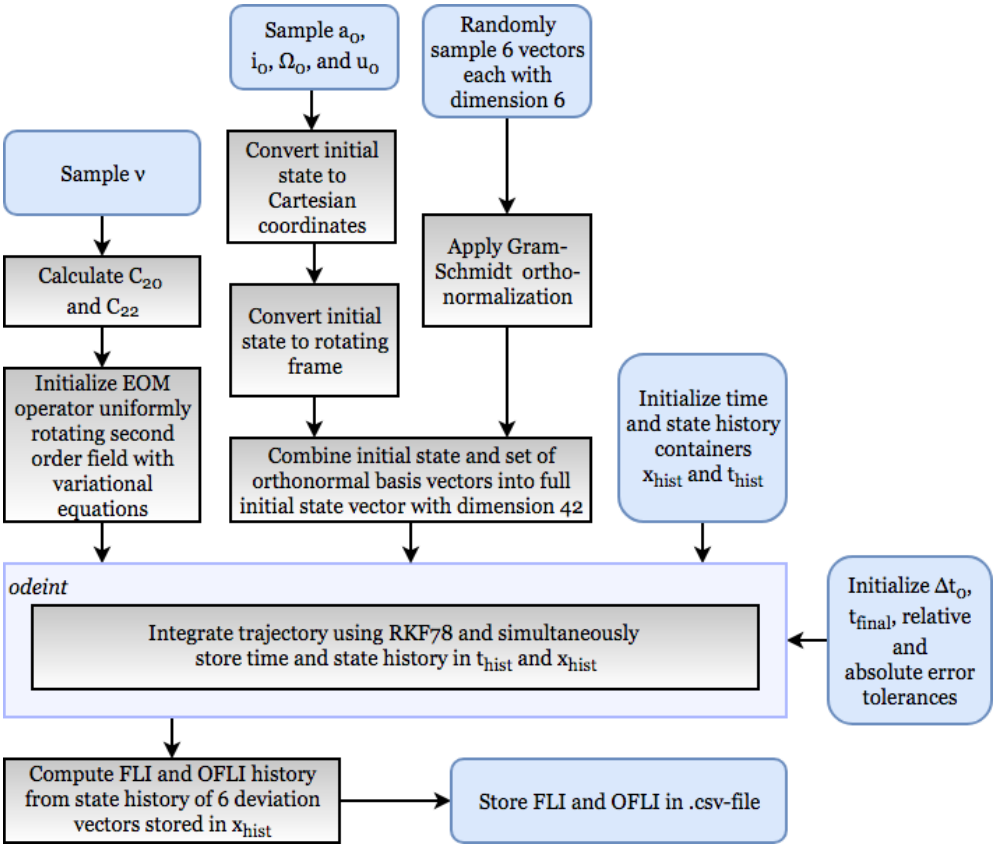

Figure 5.3: Flow diagram of sampled orbit in FLI/OFLI stability analysis.

This page is intentionally left blank.

6

Numerical Stability Analysis

Since the set of differential equations defining the physical environment around the asteroid can only be solved analytically to first order, it is favorable to carry out a large numerical parametric stability analysis in order to identify stability regions near the asteroid. This can be achieved by numerically integrating a large number of initial conditions in the phase space around the asteroid and quantitatively determining whether the resulting trajectories are stable or unstable. In addition to varying the initial conditions of the sampled trajectories, it is also possible and desirable to consider variations in the gravity field of the asteroid. In this way, it can be assessed whether the stability of a certain trajectory is robust against gravity field uncertainties and the results become applicable to a wide range of small bodies. In this chapter, stability in the vicinity of the Psyche asteroid and a general second degree and order gravity field will be analyzed and discussed. The main focus is a numerical analysis of stability using BIBO-stability constraints. Firstly, a practical definition of stability similar to BIBO-stability is introduced in Section 6.1. Secondly, the methodology of the numerical analyses is presented in Section 6.2. After that, Section 6.3 presents and discusses the results of the general stability analysis and introduces an empirical conservative stability limit. Finally, Sections 6.4 and 6.5 focus on the Psyche mission specifically and analyze the influence of higher-order spherical harmonic coefficients.

6.1. Practical Definition Stability

One option to analyze stability in a dynamical system is eigenvalue analysis. However, this method gives a mathematical and therefore restrictive test of stability. In addition, most common stability tests are often limited to a certain class of motion such as equilibria and periodic solutions. To find suitable orbits for the Psyche mission, it is more applicable to analyze stability from a practical point of view similar to Hu and Scheeres (2004) and Araujo et al. (2015). Instead of restricting the analysis to a certain class of orbits around the asteroid and mathematical constraints, numerical conditions can be imposed on the orbits that define stability from a mission perspective.

Hu and Scheeres (2004) proposed a numerical stability condition based on the evolution of Keplerian elements of the trajectory. As mentioned before, it was shown analytically by Scheeres (1999b) that orbits close to the body experience significant short-term non-periodic variations in a and e. This behaviour is clearly illustrated in Figure 6.1, which shows stable, impact and escape trajectories in Psyche's second degree and order gravity field for prograde equatorial orbits. All three orbits were initialized with $C_J > C_{J_X}$. However, the orbit that impacts the asteroid was initialized inside the zero-velocity surface $C_J = C_{J_X}$ and the other two orbits were initialized outside this surface, conforming with the concept of zero-velocity surface analysis presented in Appendix B.

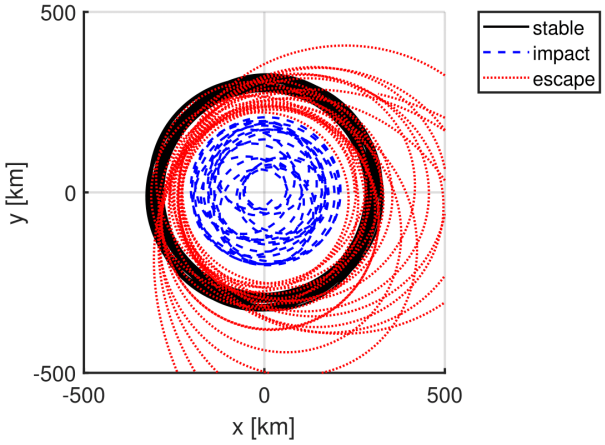

(a) View in equatorial plane in the inertial frame.

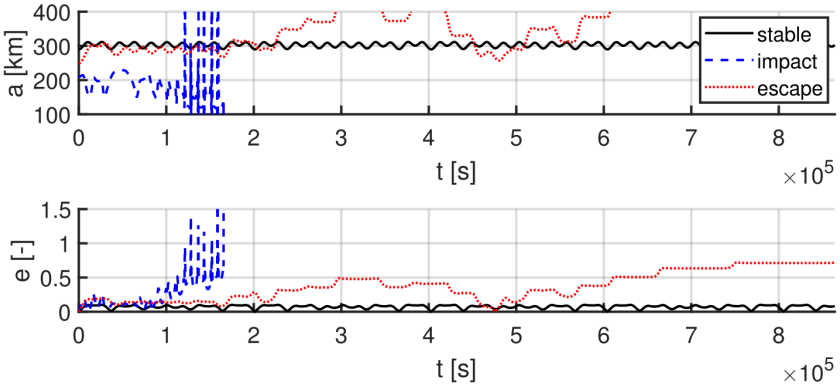

(b) Orbit size and shape parameters a and e.

Figure 6.1: Stable, impact and escape trajectories in Psyche's nominal second degree and order gravity field. The trajectories are initialized as circular orbits in the xy-plane at semi-major axes 290, 210 and 250 km respectively.

From Figure 6.1b, it is clear that stability correlates strongly with the extent to which a and e vary over time. By the definition of Hu and Scheeres (2004), the impacting and escaping orbits are both size-shape unstable and the regular orbit is size-shape stable. A possible criterion for stability is that the maximum change in eccentricity Δe_{max} cannot be larger than a specified value. The choice of this value is somewhat arbitrary, but 0.25 appears realistic as Hu and Scheeres (2004) noted that any Δe_{max} between 0.2 and 0.6 can be appropriate. In addition, it is sufficient to track changes in e since a considerable change in the semi-major axis of an orbit is not possible without a change in eccentricity. To determine the stability of an orbit, a limit has to be set on the duration of propagation T_f. This duration is set at 90 days, which is considerably longer than the time the spacecraft has to be able to orbit safely without operator intervention (28 days as specified by Oh et al. (2017)). Subsequently, a practical stability constraint is presented in Equation 6.1.

$$|e(t) - e_0| < \Delta e_{max}, \{t \,|\, 0 \leq t \leq T_f\} \tag{6.1}$$

Another possible stability criterion is to specify a range of allowable radii. Again, it is arbitrary to specify numerical values for r_{min} and r_{max}. However, values which are assumed to be realistic and compatible with the orbits of Figure 2.5 are presented in Equations 6.2 and 6.3.

$$r_{min} = 0.75 r_{p_0} = 0.75(1 - e_0)a_0 \tag{6.2}$$

$$r_{max} = 1.5 r_{a0} = 1.5(1 + e_0) a_0 \tag{6.3}$$

In the equations above, r_{p_0} and r_{a0} are the initial periapsis and apoapsis distances respectively. In addition, the discrepancy between r_{max} and r is allowed to be larger since impact is considered more detrimental from a mission and planetary protection perspective compared to escape. This stability criterion is presented in Equation 6.4.

$$r_{min} < r(t) < r_{max}, \{t \,|\, 0 \leq t \leq T_f\} \tag{6.4}$$

Both stability criteria can be compared for a large sample of orbits. Initially circular orbits are propagated in Psyche's nominal uniformly rotating second degree and order gravity field for varying initial semi-major axes and varying ν with $i_0 = 70$ deg, $\Omega_0 = 120$ deg, $\theta_0 = 45$ deg and $\sigma = 0.5$. A comparison of both criteria is presented in Figure 6.2, where the black and white regions indicate initial conditions leading to stable and unstable orbits respectively, according to the imposed stability criterion.

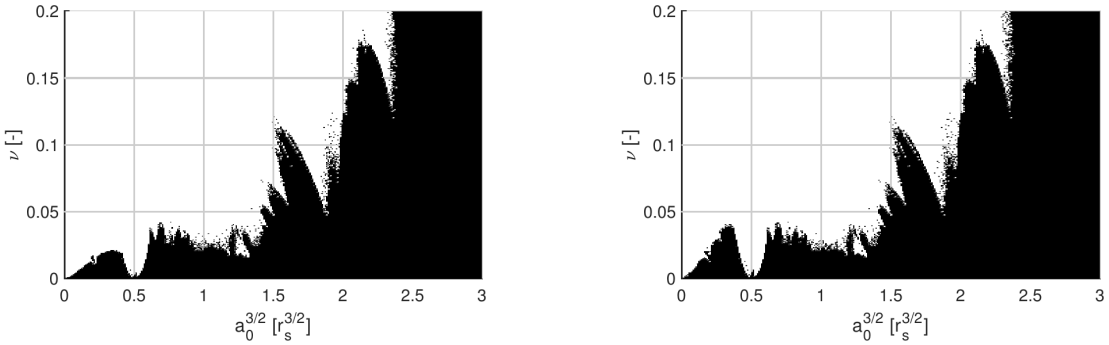

(a) Stability plot according to criterion on e.

(b) Stability plot according to criterion on r.

Figure 6.2: Comparison of stability criteria for a large sample of orbits within a second degree and order gravity field, where $i_0 = 70$ deg, $\Omega_0 = 120$ deg, $\theta_0 = 45$ deg and $\sigma = 0.5$. The black and white regions indicate initial conditions leading to stable and unstable orbits respectively. Trajectories were propagated for 515 asteroid rotations (90 days in Psyche's denormalized system).

From Figure 6.2, it is clear that the choice of stability criterion does not affect the global characterization of stability. Unsurprisingly, variations in e and r are strongly correlated. Therefore, the stability criterion on r (Equation 6.4) will be used, since it is even more intuitive when compared to the condition on e (Equation 6.1). Furthermore, a condition based on the distance between the orbiting body and the central body is more directly related to the mission requirement for safe science orbits. In some cases, a condition on e might be too restrictive (if e varies more strongly over a short time span when compared to r) or not restrictive enough.

The stability condition presented in Equation 6.4 is a relative one and can generally be applied to any body. In addition to this condition, it is possible to define an absolute condition specifically applicable to the Psyche mission. The maximum radius of the Psyche asteroid is 140 km. Therefore, it is realistic to place an additional constraint on $r(t)$ based on this maximum radius. To limit the probability of impact on the asteroid surface, $r(t)$ shall be larger than 150 km over the 90-day period. This stability condition is then presented in Equation 6.5.

$$\max(r_{min}, 150\,\text{km}) < r(t) < r_{max}, \{t \,|\, 0 \leq t \leq T_f\} \tag{6.5}$$

6.2. Methodology

6.2.1. Analysis A

The first numerical analysis builds upon the work done by Hu and Scheeres (2004) and considers initially circular orbits in a uniformly rotating second degree and order gravity field. However, the work is extended drastically by including variations in the initial inclination of the orbit i_0, the initial right ascension of the ascending node Ω_0 and the initial argument of latitude u_0. In this way, the analysis also has a practical value for Psyche's mission design and possibly many other future small-body missions which consider circular orbits for their nominal mission phase. Consequently, the initial conditions will be sampled for varying a_0, i_0, Ω_0 and u_0. It is required to represent the initial position of the spacecraft in its orbit by the argument of latitude $u = \omega + \theta$ for non-equatorial circular orbits since the argument of periapsis and the true, eccentric and mean anomaly are undefined for circular orbits. Furthermore, for the special case of circular equatorial orbits, u is also undefined and the true longitude $\lambda_t = \Omega + \omega + \theta$ is used to represent the position of the spacecraft within its instantaneous Kepler orbit. Non-circular orbits are excluded from this analysis to decrease the dimensionality of the search space.

The main goal of analysis A is to characterize stability, while considering large variations in the gravity field of the asteroid as well. Therefore, a simple second degree and order gravity field will be used. In this way, variations in the gravity-field parameters are restricted to variations in C_{20} and C_{22}, or equivalently σ and ν. Consequently, the search space for analysis A is six-dimensional. The sampling scheme is presented in Table 6.1. In case of equatorial orbits, λ_{t0} is sampled according to the sampling scheme of Ω_0. Since the results of analysis A are general for any uniformly rotating body, the stability condition is the inequality presented in Equation 6.4, without an additional (and absolute) condition for impact.

Parameter	Sampling Range	Sampling Interval	Number of Samples	Unit
$(a_0/r_s)^{3/2}$	[0.01,4]	0.01	400	-
i_0	[0,180]	10	19	deg
Ω_0	[0,160]	20	9	deg
u_0	[0,135]	45	4	deg
ν	[0,0.2]	0.02/3	301	-
σ	[0.5,1.0]	0.25	3	-

Table 6.1: Sampling scheme of analysis A. The orbital parameters of initially circular orbits are varied as well as the second degree and order gravity-field parameters σ and ν. Total number of trajectories propagated: $2.47\ 10^8$.

Since resonances of the spacecraft's mean motion with the rotation of the asteroid have a crucial impact on stability close to the body, $(a_0/r_s)^{3/2}$ is sampled with a high resolution. At Psyche's 1:1 resonance radius, the resolution is smaller than 1.5 km. For completeness, $(a_0/r_s)^{3/2}$ ranges from 0.01 to 4 such that the obtained results can be applied to almost any combination of central body and orbiting object. Furthermore, it will be clear that all orbits are stable for $(a_0/r_s)^{3/2} > 4$. The motivation for sampling $(a_0/r_s)^{3/2}$ instead of a_0/r_s is to clearly show the influence of mean motion resonance on stability, since $(a_0/r_s)^{3/2} \propto T$, where T is the orbital period.

ν is a variable that accounts for the ellipticity of the body and correlates strongly with C_{22}. It was shown by Hu and Scheeres (2004) to have a large impact on orbital stability. Consequently, ν is sampled with a high resolution as well: it ranges from 0 to 0.2 (see Section 3.2).

Orbital elements i_0, Ω_0 and u_0 are all sampled with decreasing resolution since their impact on stability is assumed to be smaller. Of these three orbital elements, i_0 correlates the most with stability as it is well known that retrograde orbits are generally more stable when compared with prograde orbits (Zhang and Innanen, 1988). Furthermore, it is assumed that the initial position of the spacecraft within its orbit influences stability the least. However, it was identified that u_0 does have some influence on stability, especially close to the body (where changes in a and e can occur on a very short time span). In addition, the problem is point-symmetric about the origin. It can easily be shown that $V(-\boldsymbol{r}) = V(\boldsymbol{r})$ for the second degree and order gravity field (see Equations 3.17 and C.1). Therefore, Ω_0 and u_0 are both sampled for values below 180 deg only. Otherwise trajectories would be propagated which are mirrored about the origin, which is redundant.

Finally, trajectories are propagated for σ = 0.5, 0.75 and 1.0. As mentioned by Hu and Scheeres (2004), this brackets the parameter space since $\sigma > 0.5$ for most asteroids. For example, asteroids Castalia and Itokawa have values of 0.9 and 0.92 for σ. In contrast, the Earth (which has a roughly oblate spheroidal shape) has a σ-value close to zero, meaning that also trajectories close to the body are almost always stable. In addition, stability varies moderately and linearly with σ, which will be shown in the results and justifies a low-resolution sampling for this parameter.

This analysis is extremely valuable for mission design since it will allow the identification stable regions in the parameter space for any uniformly rotating asteroid assuming its second degree and order gravity field (excluding asteroids experiencing tensile stress due to fast rotation). In addition, the results are general for any asteroid mass and rotational rate. For any combination of μ, ω_A, C_{20} and C_{22}, it will be possible to identify which circular orbits are stable, moderately stable or completely unstable given the initial semi-major axis a_0 and inclination i_0. The analysis will be used to assess stability in the vicinity of the Psyche asteroid as an example. To generate these generalized results, a total of number of approximately 250 million trajectories are propagated for a duration of 515 asteroid rotations (90 days in Psyche's denormalized system).

6.2.2. Analysis *B*

The second analysis considers the second degree and order gravity field similar to analysis *A*. However, analysis *B* is specifically aimed at characterizing stability near the Psyche asteroid and covers both its nominal and conservative gravity fields. Consequently, analysis *B* will be especially valuable for the Psyche mission. The analysis is executed for σ and ν presented in Table 3.2. By removing significant variations in σ and ν throughout the analysis, it is possible to consider non-circular orbits as well, which adds an additional dimension to the parameter space of initial conditions. Since two dimensions in the parameter space of analysis *A* are removed (σ and ν), the parameter space is five-dimensional, with θ_0 set to zero for non-circular non-equatorial orbits. For circular non-equatorial orbits ω is undefined and the initial argument of latitude u_0 is sampled according to the sampling scheme of Ω_0. For non-circular equatorial orbits, Ω is undefined and the initial longitude of periapsis $\bar{\omega}_0$ is sampled according to the sampling scheme of Ω_0. Finally for circular equatorial orbits, the true longitude λ_t is used to represent the position of the spacecraft within its instantaneous Kepler orbit. The sampling scheme of analysis *B* is presented in Table 6.2.

Since Analysis *B* considers variations in the eccentricity as well, $(r_{p_0}/r_s)^{3/2}$ is sampled instead of $(a_0/r_s)^{3/2}$ from 0.01 to 4. In this way, it is easier to deduct from the stability plots, how close the sampled orbits get to the asteroid. Since the dimensionality of the parameter space is reduced, the initial inclination can be sampled with a higher resolution compared to analysis *A* with intervals of 1 deg. The eccentricity is sampled with an interval of 0.05 ranging from 0 to 0.5. Larger eccentricities are not considered due to their limited practical value for the Psyche mission. Finally, Ω_0 and ω_0

Parameter	Sampling Range	Sampling Interval	Number of Samples	Unit
$(r_{p_0}/r_s)^{3/2}$	[0.01,4]	0.01	400	-
i_0	[0,180]	1	181	deg
e_0	[0,0.5]	0.05	11	-
Ω_0	[0,150]	30	6	deg
ω_0	[0,135]	45	4	deg

Table 6.2: Sampling scheme of analysis *B*. Five Keplerian elements are sampled and orbits are propagated in Psyche's nominal and conservative second degree and order gravity field. Total number of trajectories propagated: 1.91 10^7.

are sampled with a lower resolution compared to analysis *A*, such that the discrepancy with the sampling intervals for Ω_0 and ω_0 of analysis *C* is limited.

6.2.3. Analysis *C*

The final numerical stability analysis is almost identical to analysis *B*, but differs in two ways. Firstly, and most importantly, analysis *C* uses the nominal and conservative eighth degree and order gravity fields. This is essential to answer one of the research goals, which is to assess whether a second degree and order gravity field can be used to globally characterize stability around a small body. By comparing the results of analysis *B* with analysis *C*, this question can be answered. In addition, the results will provide valuable information for the Psyche mission. It can be assessed whether the orbits that are currently proposed are stable (for both the nominal and conservative gravity fields), and alternative mission scenarios can potentially be suggested.

Secondly, Ω_0 and ω_0 are sampled from 0 to 360 deg since the effective potential for a higher degree and order gravity field is generally not point-symmetric about the origin. The use of a higher degree and order gravity field requires considerably more function evaluations during orbit propagations. Consequently, the computation time for analysis *C* is higher compared to analysis *B*. The sampling interval of Ω_0 and ω_0 is therefore slightly increased when compared to analysis *B* (still, with more samples for these two parameters). The sampling scheme of analysis *C* is presented in Table 6.3.

Parameter	Sampling Range	Sampling Interval	Number of Samples	Unit
$(r_{p_0}/r_s)^{3/2}$	[0.01,4]	0.01	400	-
i_0	[0,180]	1	181	deg
e_0	[0,0.5]	0.05	11	-
Ω_0	[0,320]	40	9	deg
ω_0	[0,300]	60	6	deg

Table 6.3: Sampling scheme of analysis *C*. Five Keplerian elements are sampled and orbits are propagated in Psyche's nominal and conservative eighth degree and order gravity field. Total number of trajectories propagated: 4.30 10^7.

6.3. Analysis *A*

6.3.1. Stability plots

For all trajectories propagated in the normalized second degree and order gravity field, the minimum and maximum radial distance (r_{min} and r_{max}) of the spacecraft with respect to the CoM of the body can be stored. By subjecting these values to the stability condition specified in Equation 6.4, it can be assessed whether a given initial condition leads to a stable or unstable orbit around the body.

Subsequently, surface plots can be generated with $(a_0/r_s)^{3/2}$ along the x-axis and ν along the y-axis. These stability plots can be produced for a given combination of i_0, Ω_0, u_0 and σ, similar to what was shown in Figure 6.2. In these plots, the black and white regions indicate initial conditions leading to stable and unstable trajectories respectively. To show the influence of Ω_0 and u_0 on stability, four stability plots are shown in Figure 6.3 for i_0 = 90 deg and σ = 1.0 and varying Ω_0 and u_0. This figure only shows a small subset of the 36 combinations of Ω_0 and u_0 for a given i_0 and σ.

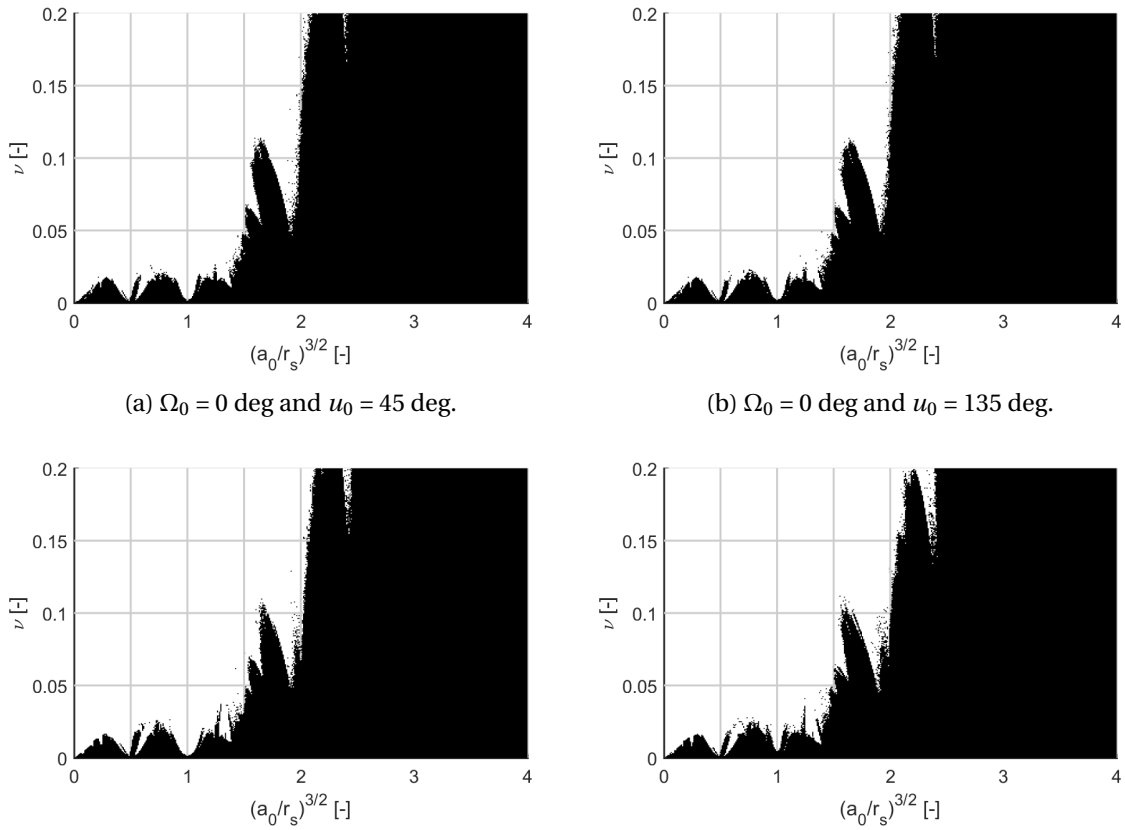

(a) Ω_0 = 0 deg and u_0 = 45 deg.

(b) Ω_0 = 0 deg and u_0 = 135 deg.

(c) Ω_0 = 80 deg and u_0 = 45 deg.

(d) Ω_0 = 80 deg and u_0 = 135 deg.

Figure 6.3: Stable and unstable regions for σ = 1.0 and i_0 = 90 deg for a second degree and order gravity field. Different plots show stability regions for varying initial conditions in Ω_0 and u_0. The black and white regions indicate stable and unstable trajectories according to Equation 6.4.

From the stability plots presented in Figure 6.3, several important characteristics can be observed. Firstly, the basic trend is that stability increases with decreasing values of ν and increasing values of $(a_0/r_s)^{3/2}$. This is expected since ν is strongly correlated with C_{22}, which is known to cause large variations in orbital energy (Scheeres, 1999b) and the influence of gravity-field perturbations decreases with distance away from the body. Secondly, mean motion resonances with central body rotation have a strong detrimental impact on orbit stability. Referring back to the analytically derived solutions in Equations 4.27 and 4.28 for a and e respectively, the numerical results confirm the instabilities caused by mean motion resonances appearing in the analytical equations. The strongest resonances that can be observed for this set of initial conditions are 1:2, 1:1, 3:2 and 2:1. These are the resonances that also appeared in the analytical expressions. It is clear that many other resonances (like 5:2) have influence as well, but do not show up in the analytical equations due to the assumptions that were made. Thirdly, Ω_0 and u_0 have a small influence on the stability

plots, which was anticipated in the methodology outlined in the previous section. Although only a subset of the data is presented, these observations and conclusions hold for all combinations of i_0, Ω_0, u_0 and σ of Table 6.1 (except for i_0 approaching 180 deg, for which the influence of mean motion resonance becomes negligible).

A more effective (and paper-saving) way of illustrating stability as a function of $(a_0/r_s)^{3/2}$, i_0, ν and σ is by overlaying the stability plots (as shown in Figure 6.3) for all sampled combinations of Ω_0 and u_0 (36 in total for analysis A). Then, stability can be expressed as a percentage as shown in Equation 6.6. The overlaid stability plot is shown in Figure 6.4 for σ = 1.0 and i_0 = 90 deg.

$$\text{Stability [\%]} = \frac{\text{Number of stable orbits}}{\text{Total number of orbits}} \cdot 100 \tag{6.6}$$

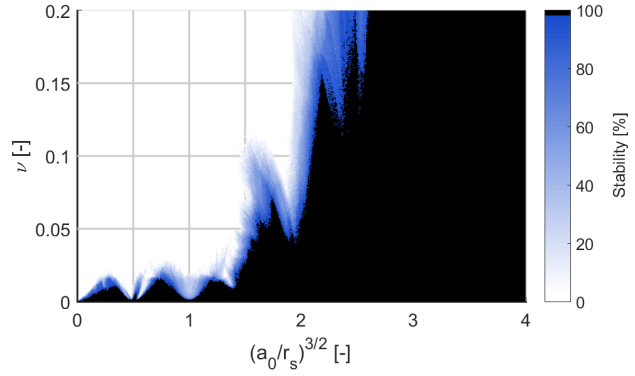

Figure 6.4: Stable (black), intermediate (blue) and unstable (white) regions in a uniformly rotating second degree and order gravity field, where σ = 1.0 and i_0 = 90 deg. Ω_0 and u_0 are varied for 36 combinations according to the sampling scheme presented in Table 6.1. The plot shows the percentage of initial conditions that result in stable trajectories according to Equation 6.4.

6.3.2. Comparison σ = 0.5, 0.75 and 1.0

In order to assess the influence of σ on orbital stability, a comparison can be made between stability plots for different values of σ. A stability plot for i_0 = 90 deg and σ = 1.0 was already shown in Figure 6.4. Therefore, stability plots for i_0 = 90 deg and σ = 0.75 and 0.5 are shown in Figures 6.5a and 6.5b respectively.

By comparing the results for σ = 0.5, 0.75 and 1.0, it is clear that more trajectories are unstable for increasing values of σ. Again, although only a subset of the data is presented, these observations and conclusions hold for all combinations of i_0 and σ of Table 6.1 (except for i_0 approaching 180 deg). To understand this behaviour, Equation 3.21 can be rewritten into Equation 6.7.

$$\sigma = \frac{4}{2 + \frac{J_2}{C_{22}}} \tag{6.7}$$

By setting a value for σ, the ratio between J_2 and C_{22} is fixed. From Equation 6.7, it can clearly be seen that C_{22}/J_2 increases for increasing values of σ. This is expected since large values of C_{22} are more detrimental for stability compared with large values of J_2. The flattening of the body does not cause variations in a and e averaged over an orbital period (Scheeres, 1994).

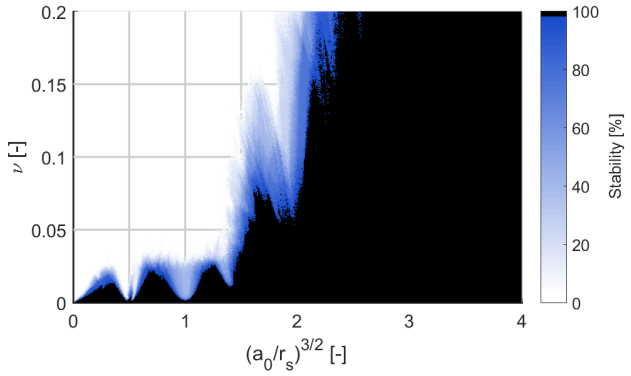

(a) $\sigma = 0.75$

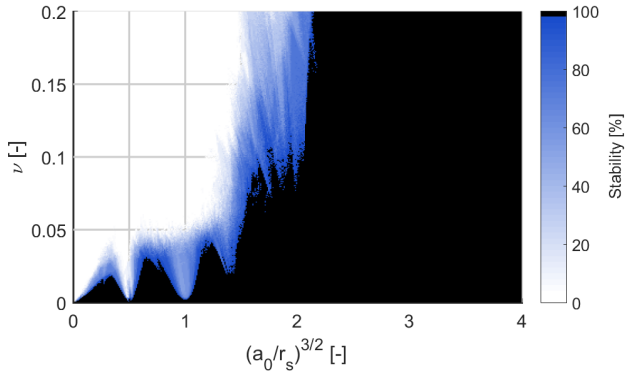

(b) $\sigma = 0.5$

Figure 6.5: Stable and unstable regions for $i_0 = 90$ deg and varying σ for a second degree and order gravity field.

6.3.3. Empirical stability limit

Holman and Wiegert (1999) investigated the long-term stability of planets in binary systems. In their analysis, the researchers investigated which regions in the phase space of the system allow for orbits to survive extended periods of time. Although the dynamical system is different and on a much larger length and time scale, their analysis holds many similarities to the analysis presented in this work regarding the uniformly rotating second degree and order gravity field. In their study, they varied the binary eccentricity and mass ratio and the semi-major axis of planets orbiting the system in circular orbits. By generating a sufficiently large set of trajectories, stable and unstable regions in the parameter space were identified. From these numerical results, the researchers were able to develop empirical expressions for the critical semi-major axis a_c as a function of binary eccentricity and mass ratio. For orbits with an initial semi-major axis larger than a_c (in the regime far away from the binary system), their orbit is very likely to be long-term stable.

In a similar fashion, an empirical expression for semi-major axis as a function of i_0, σ and ν will be developed. The empirical expression will result in a conservative bound for the stable semi-major axis a_s, above which orbits are stable (according to Equation 6.4) in the second degree and order gravity field. That is, the circular orbit with initial conditions a_0, i_0, Ω_0 and u_0 is stable in the second degree and order gravity field if $a_0 > a_s(i_0, \sigma, \nu)$, where a_0 and a_s are normalized with respect to the resonance radius r_s of the body. The developed inequality will be a sufficient condition for stability, but not a necessary one.

The first step in developing an empirical expression for a_s is to generate a set of data points that ideally represents the limit for stable orbits. Then, a_s (which contains several free parameters) will be fitted to this data set. For every stability plot (i.e. combination of i_0 and σ), samples are generated automatically at some arbitrary distance from the resonance 'cuts' within the stable (black) region to ensure that the final fit for a_s is a conservative one. The samples for two combinations of i_0 and σ are illustrated in Figure 6.6.

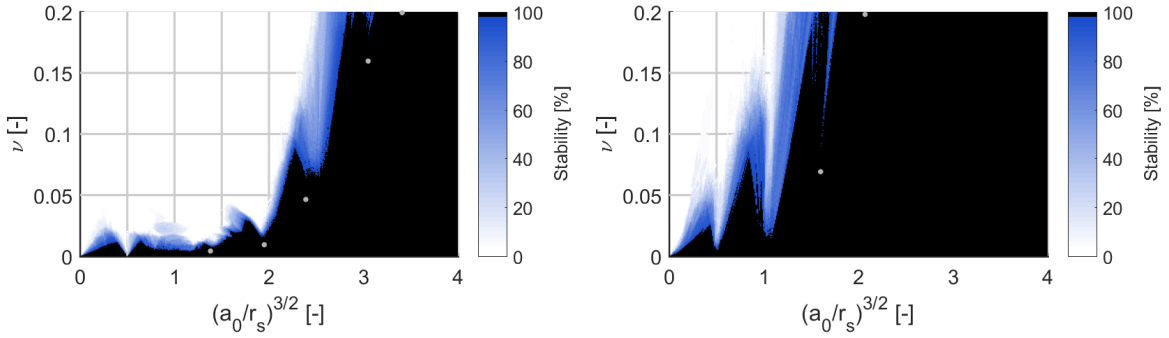

(a) i_0 = 50 deg and σ = 1.0 (b) i_0 = 130 deg and σ = 0.5

Figure 6.6: Sampling data points in stability plots to generate empirical expression for a_s. Grey dots indicate samples.

The stable limit a_s is not guaranteed to hold for $i_0 = 63.435 \pm 5$ deg and $i_0 = 116.565 \pm 5$ deg. These inclinations are known as the critical inclinations for which the argument of periapsis does not exhibit secular variations according to first-order approximations, which can easily be verified with Equation 6.8 (Wakker, 2015, p. 624).

$$\dot{\omega} = \frac{3}{4}\tilde{n}C_{20}\left(\frac{r_e}{a(1-e^2)}\right)^2(1-5\cos^2 i) \tag{6.8}$$

In the expression above, $\tilde{n}$ is the perturbed mean motion, approximately equal to the mean motion n (accurate to first order in C_{20}). Only even zonal harmonic terms produce secular variations in M, Ω and ω (Wakker, 2015, p. 624), causing only C_{20} to appear in the expression for the second degree and order gravity field. Since the orbit precesses very slowly about its angular momentum vector for inclinations close to these critical inclinations, resonances will have an even larger detrimental impact on stability. Therefore, it was decided to limit the applicability of the conservative stability limit to inclinations at least 5 degrees smaller or larger than the critical inclinations. Consequently, the stability plots for i_0 = 60 and 120 degrees will not be used to sample data points for the development of the empirical expression for a_s. The total number of stability plots used to sample data is equal to 51 and the total number of samples amounts 177.

The second step is to parameterize the volume a_s. Since the relation is empirical, the parameterization of a_s is arbitrary. Ideally, the expression for a_s is simple and fits the data points in an acceptable way (which again, is arbitrary). The proposed parameterization is presented in Equation 6.9.

$$\frac{a_s}{r_s} = \nu(\alpha_1 + \beta_1 i_0 + \gamma_1\sigma) + \sqrt{\nu}(\alpha_2 + \beta_2 i_0 + \gamma_2\sigma) + 1 \tag{6.9}$$

In the equation above, α_1, α_2, β_1, β_2, γ_1 and γ_2 are coefficients that will be solved for and i_0 should be given in radians. An important property of the empirical expression is that $a_s = 1$ for $\nu = 0$. From Figures 6.3, 6.4, 6.5 and 6.6, it is clear that the orbits are almost completely unstable

at the 1:1 resonance radius. Therefore, an ideal property of the expression for a_s is that it equals 1 for $\nu = 0$. Secondly, stability varies most strongly with ν. Therefore, two different powers of ν (1 and 1/2) appear in the expression. By observing the aforementioned figures and carrying out multiple fitting procedures with various powers of ν, it appears that a square root in ν helps in fitting the sampled data points considerably. Lastly, linear terms in i_0, σ and ν appear in the expression in order to fit the data adequately, while still maintaining a simple and easy-to-use expression for a_s.

In order to fit Equation 6.9 and its free parameters to the sampled data points, a weighted least squares is executed. The weights are distributed in such a way that each stability plot has the same weight. This is not the case with a regular least squares fit since the number of data points can vary over different stability plots (see Figure 6.6). For completeness, the weighted least squares formula is given in Equation 6.10,

$$\boldsymbol{x} = (A^T W A)^{-1} A^T W (\boldsymbol{a}_s - 1) \tag{6.10}$$

where $\boldsymbol{x}$ contains the coefficients of Equation 6.9, A is the matrix containing the function evaluations of the terms in Equation 6.9, W is the weighting matrix and $\boldsymbol{a}_s$ is a vector containing the observed values of a_s for each sampled data point. After executing Equation 6.9, the best-fit parameters are obtained in vector $\boldsymbol{x}$ and are presented in Table 6.4. In addition, the RMS can be computed between vector $\boldsymbol{a}_s$ and the empirical fit values of $\frac{a_s}{r_s}$ using Equation 6.9. This is done using MATLAB©.

Parameter	Value
α_1	-3.41
α_2	4.35
β_1	3.86
β_2	-2.29
γ_1	-4.98
γ_2	2.41
RMS	0.08

Table 6.4: Weighted least squares fit for $\frac{a_s}{r_s}$.

To ensure that the expression is conservative and sufficient for stability, the RMS is added to $\frac{a_s}{r_s}$. Comparing the RMS to the model parameters, it is clear that the empirical expression fits the data well. In addition, the R^2-value (which is a quantitative measure of the goodness of a fit) of the empirical function is calculated as well and is equal to 0.95, which indicates that the model fits the data well. The final empirical expression for $\frac{a_s}{r_s}$ is given in Equation 6.11,

$$\frac{a_s}{r_s} = \nu(-3.41 + 3.86 i_0 - 4.98\sigma) + \sqrt{\nu}(4.35 - 2.29 i_0 + 2.41\sigma) + 1.08 \tag{6.11}$$

which holds within the parameter space presented in Table 6.5. It is emphasized that the developed empirical stability limit is generally applicable to the majority of small bodies. Knowing the mass, the uniform rotation rate, C_{20} and C_{22} of an irregular body, it is possible to determine a sufficient condition for the stability of initially circular orbits in the uniformly rotating second degree and order gravity field. Equation 6.11 can be used for verification purposes and is especially of practical value for back-of-the-envelope preliminary mission design. To illustrate the empirical stability limit, a_s is shown on the stability plots of Figure 6.6 in Figure 6.7.

Parameter	Constraint	Unit
a_s/r_s	$a_s/r_s > 0$	-
i_0	$0 \leq i_0 \leq 1.020$ or $1.194 \leq i_0 \leq 1.947$ or $2.122 \leq i_0 \leq \pi$	rad
e_0	$e_0 = 0$	-
σ	$0.5 \leq \sigma \leq 1.0$	-
ν	$0 \leq \nu \leq 0.2$	-

Table 6.5: Constraints for which the empirical expression in Equation 6.11 holds.

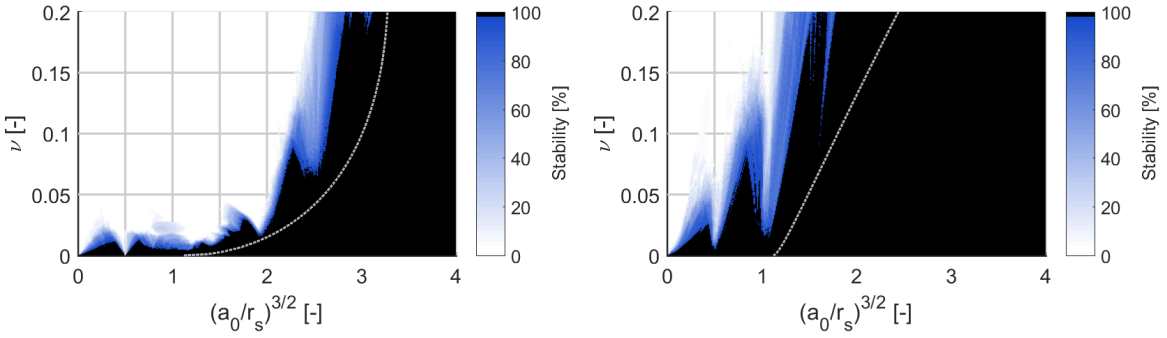

(a) $i_0 = 50$ deg and $\sigma = 1.0$

(b) $i_0 = 130$ deg and $\sigma = 0.5$

Figure 6.7: Empirical stability limit a_s (grey dotted line). Orbits with $a_0 > a_s$ are stable.

6.3.4. Results for Psyche ($\sigma \approx 0.5$)

In Table 3.2, σ is given for Psyche's nominal and conservative second degree and order gravity field as 0.5406 and 0.5888 respectively. The results of analysis A are given for $\sigma = 0.5$, 0.75 and 1.0. To extract useful information on stability for orbits around the Psyche asteroid, it is assumed that $\sigma = 0.5$. To ensure that the approximation is conservative, ν is calculated again for $\sigma = 0.5$ and C_{22} fixed. Now, ν has values 0.0457 and 0.0781 for the nominal and conservative gravity fields respectively. Therefore, the error made by the approximation results in an overestimation of the magnitude of C_{20}, which is conservative.

Stability plots can be generated for $\sigma = 0.5$ at various inclinations. First, results are shown for $i_0 = 0$ deg in Figure 6.8.

Again, the figure presents the stable and unstable regions around a uniformly rotating second degree and order gravity field. In addition, the values of ν for Psyche's nominal and conservative gravity fields are indicated by the lower and upper blue horizontal lines respectively. The red leftmost vertical line indicates the lowest allowable radial distance of 150 km and the three dashed green lines represent mission orbits D, C and B from left to right (orbit A has a semi-major axis outside of the sampled range and is always stable). Finally, the stability limit a_s is shown as well. Figure 6.8 is of limited practical value to the Psyche mission since equatorial orbits are unfavorable due to limited coverage capabilities. In addition, it can be seen that orbits B and C are unstable for both the nominal and the conservative gravity fields. This is not surprising since orbits with low inclinations are more often unstable when compared to orbits of higher inclinations.

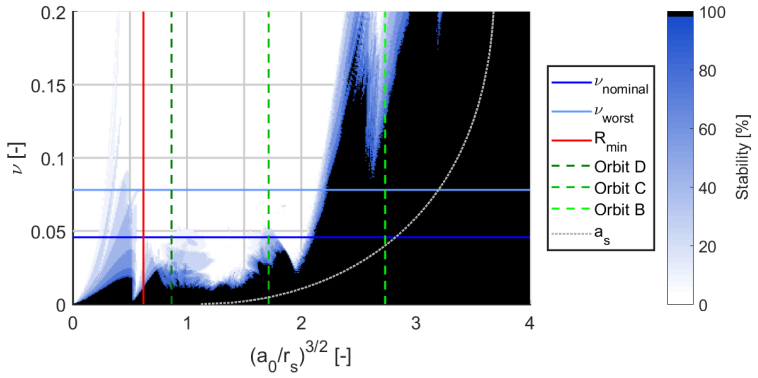

Figure 6.8: Stable (black), intermediate (blue) and unstable (white) regions in a uniformly rotating second degree and order gravity field, where $\sigma = 0.5$ and $i_0 = 0$ deg.

According to Oh et al. (2017), Psyche's currently selected orbits A, B and C are polar orbits with inclinations $i_0 \approx 90$ deg, whereas orbit D is a retrograde orbit with an inclination of $i_0 = 160$ deg. In order to analyze various realistic inclinations for all mission orbits, stability plots are shown for inclinations $i_0 = 90$, 120, 140, 160 and 180 deg in Figure 6.9.

For orbits propagated in the second degree and order gravity field, it can be seen in Figure 6.9a that the vertical lines of polar orbits B and C intersect with both horizontal lines (representing ν for the nominal and conservative gravity field) in the black (stable) region. Therefore, it can be concluded that polar orbits B and C are stable over a duration of at least 90 days and that these orbits are robust against variations in the dominant C_{22} gravity field term. Also, these orbits remain stable for varying Ω_0 and u_0. This observation provides external validation to the trajectory design of the Psyche mission for these orbits. However, considering the conservative gravity field, orbit C is on the verge of becoming only marginally stable. Higher-order gravity terms might cause orbit C to become unstable in the conservative gravity field (which will be explored in Section 6.5). In the same figure, it can also be seen that orbit D (which is closest to the asteroid surface) is unstable at an inclination of 90 deg, which again, complies with the results presented by Oh et al. (2017). Consequently, for orbit D to remain stable over a duration of at least 90 days, it is required that its inclination i_0 is larger than 90 deg.

Figure 6.9a also shows the empirical stability limit a_s, which provides a conservative value for the initial semi-major axis above which all circular orbits are stable. Using Equation 6.11, $a_s = 311.4$ km and 339.2 km considering the nominal and conservative gravity fields respectively. According to these values, polar orbits A and B are guaranteed to be stable, which is true. However, orbits C and D have a semi-major axes which lie below these values so nothing can be stated on the stability of these orbits and an analysis such as the one presented in the previous paragraph must be executed.

Figures 6.9b, 6.9c, 6.9d and 6.9e show stability plots for retrograde orbits in order to determine which inclinations are suitable for orbit D from a stability and coverage perspective. Firstly, it can be seen in Figure 6.9b that an inclination of 120 degrees for orbit D places the intersections of the vertical line for orbit D and both horizontal lines in the blue (intermediate) region. Therefore, it is possible to find stable trajectories at $i_0 = 120$ deg depending on the choice of Ω_0 and u_0. Consequently, stability at $i_0 = 120$ deg is not robust against variations in initial conditions and therefore not ideal. In addition, $i_0 = 120$ deg lies very close to the critical inclination of 116.565 deg, which is undesirable. At $i_0 = 140$ deg (shown in Figure 7.16c), orbit D is completely stable for both the nominal and conservative gravity fields. At this inclination, the stability of the orbit is robust against

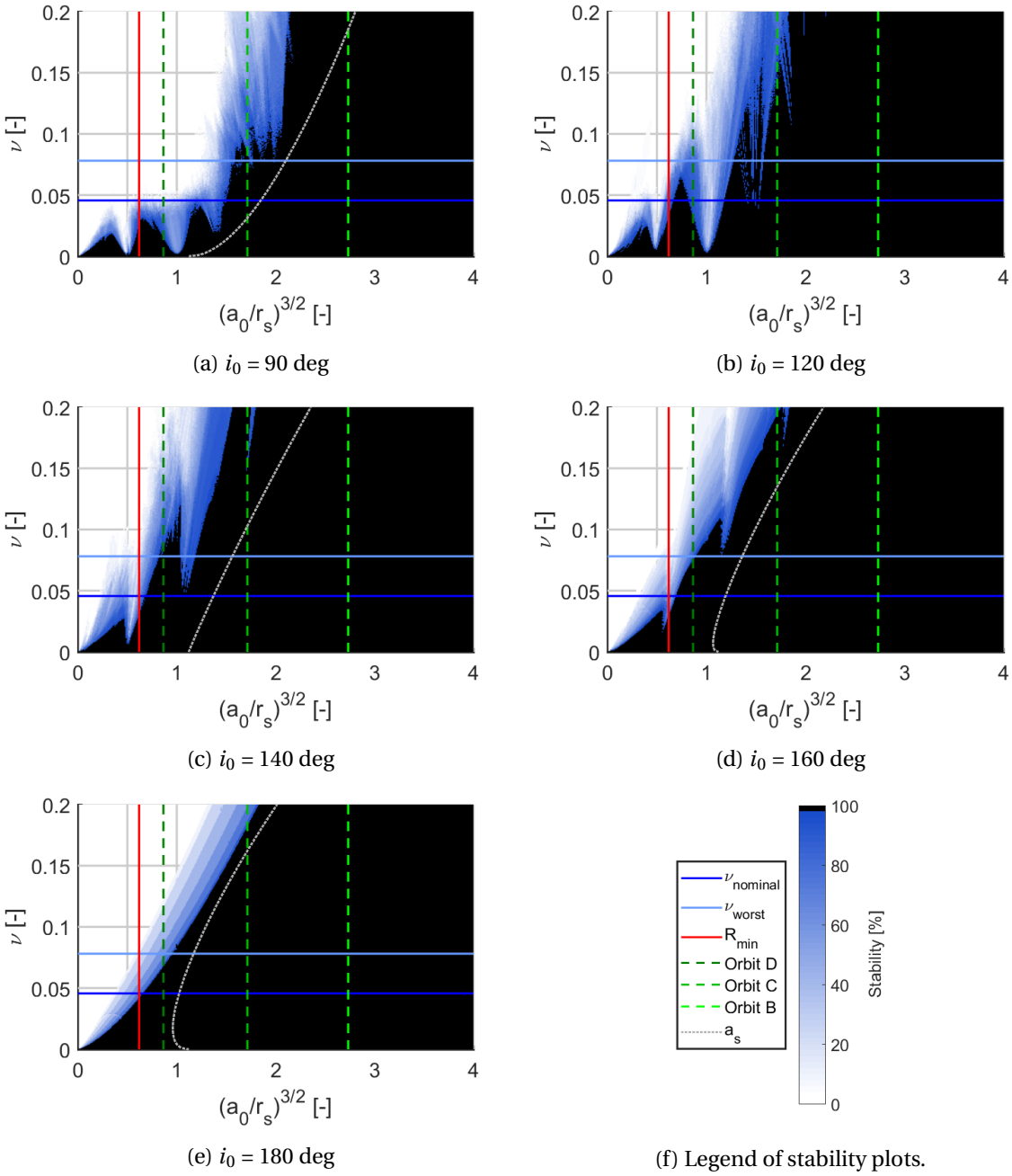

(a) i_0 = 90 deg

(b) i_0 = 120 deg

(c) i_0 = 140 deg

(d) i_0 = 160 deg

(e) i_0 = 180 deg

(f) Legend of stability plots.

Figure 6.9: Stable (black), intermediate (blue) and unstable (white) regions in a uniformly rotating second degree and order gravity field, where $\sigma = 0.5$ and i_0 varies for each plot.

variations in Ω_0 and u_0 and the dominant C_{22} gravity field term. Finally, at inclinations 160 and 180 degrees, the stability of orbit D deteriorates and coverage of the asteroid diminishes. Therefore, an inclination of 140 degrees for orbit D is recommended from a stability and coverage perspective. This recommendation is different from the currently proposed inclination of 160 degrees by Oh et al. (2017).

6.4. Analysis *B*

As mentioned before, analysis *B* is specifically aimed at analyzing stability near the Psyche asteroid in the second degree and order gravity field by fixing values of σ and ν to the values determined for the nominal and conservative gravity fields. In addition, the stability and behaviour of non-circular orbits is analyzed as well. Figures 6.10 and 6.11 present stability plots for the nominal (left) and conservative (right) gravity fields. The initial eccentricity e_0 varies from 0 to 0.3 with steps of 0.1. In these figures, the initial inclination i_0 is shown on the y-axis and the initial periapsis distance r_{p_0} is shown on the x-axis. Note that the stability condition used in analyses B and C contains the additional constraint that r must always be larger than R_{max}, which is 150 km.

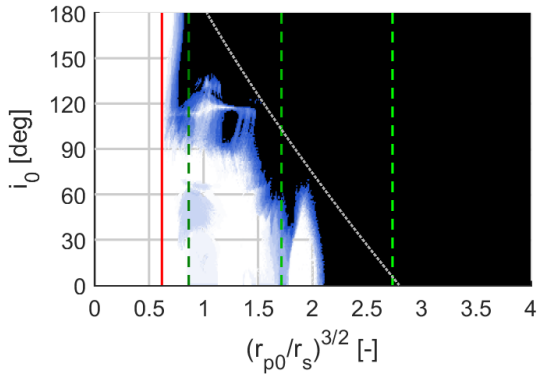

(a) Nominal gravity field, $e_0 = 0$.

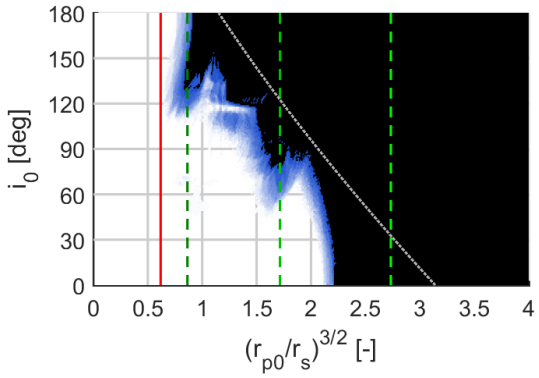

(b) Conservative gravity field, $e_0 = 0$.

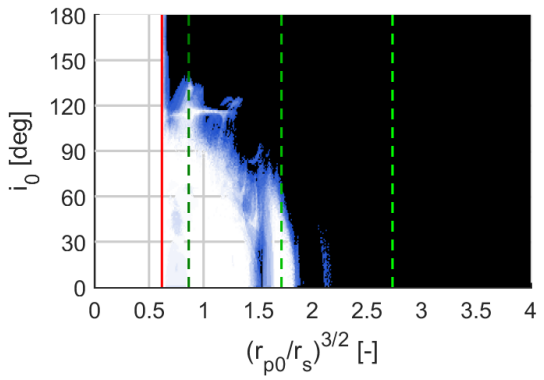

(c) Nominal gravity field, $e_0 = 0.1$.

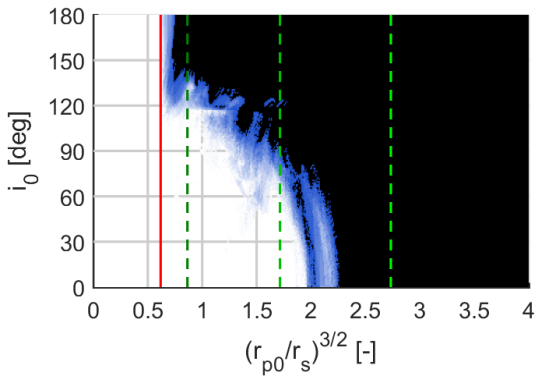

(d) Conservative gravity field, $e_0 = 0.1$.

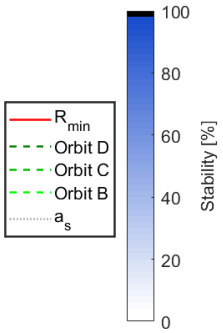

(e) Legend of stability plots.

Figure 6.10: Stable (black), intermediate (blue) and unstable (white) regions in the vicinity of asteroid Psyche in a uniformly rotating second degree and order gravity field. The empirical stability limit is also shown for the stability plots with initially circular orbits.

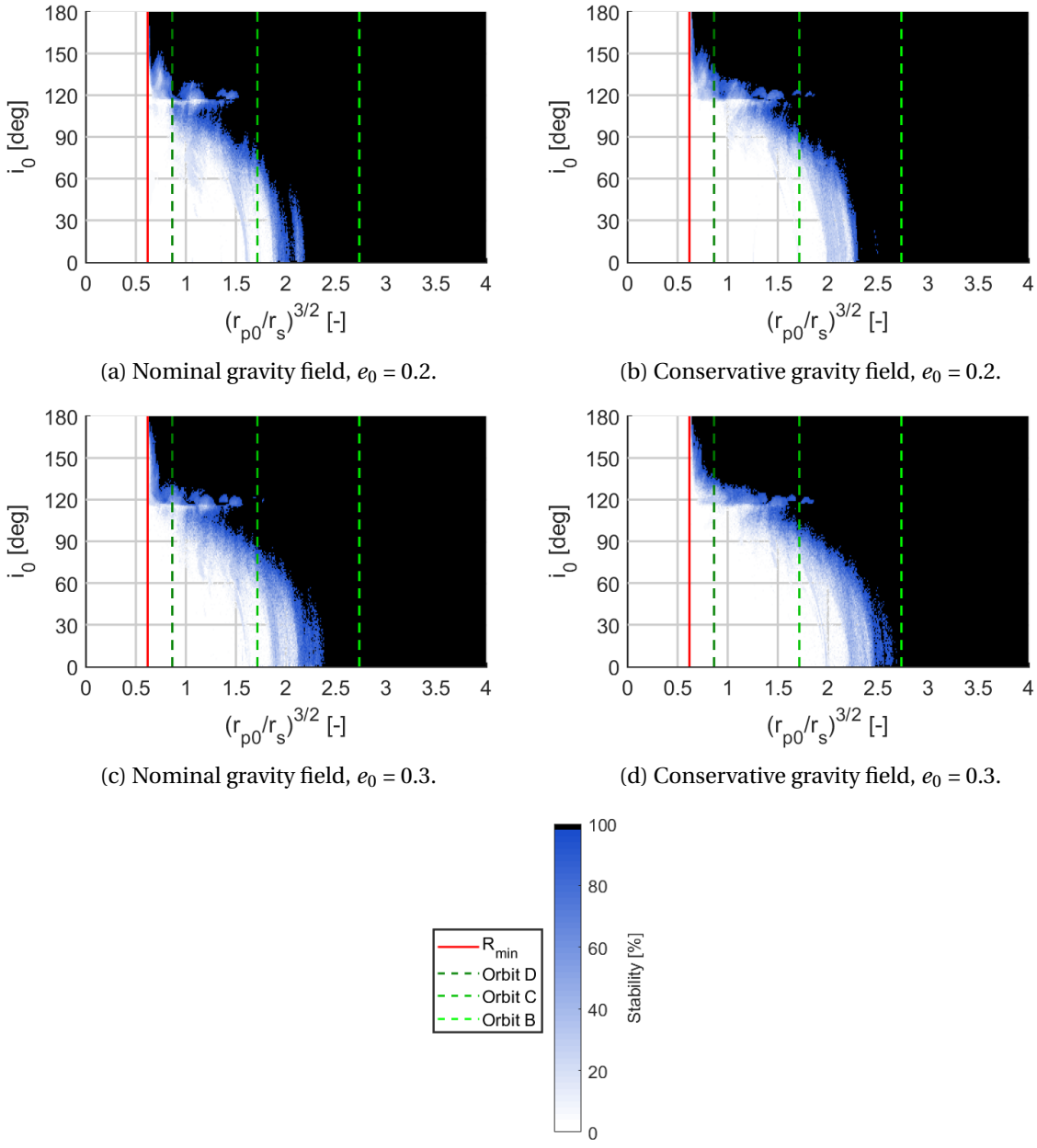

(a) Nominal gravity field, $e_0 = 0.2$.

(b) Conservative gravity field, $e_0 = 0.2$.

(c) Nominal gravity field, $e_0 = 0.3$.

(d) Conservative gravity field, $e_0 = 0.3$.

(e) Legend of stability plots.

Figure 6.11: Stable (black), intermediate (blue) and unstable (white) regions in the vicinity of asteroid Psyche in a uniformly rotating second degree and order gravity field.

Firstly, it can be seen that the stable regions for the conservative gravity field are smaller when compared to the nominal gravity field, which is expected. Secondly, Figures 6.10a and 6.10b illustrate that the empirical stability limit works well, even at inclinations close to the critical inclinations. Furthermore, these figures show that circular orbits B and C are stable at an inclination of 90 deg and an inclination of approximately 140 deg is suitable for orbit D. Unsurprisingly, this complies with the analysis of Section 6.3. Figures 6.10 and 6.11 also show the detrimental impact of the critical inclination (116.656 deg) on orbital stability.

Going from top to bottom in Figures 6.10 and 6.11 (increasing initial eccentricity e_0), it can be seen that selecting a non-zero eccentricity for orbits with high inclinations ($i_0 > 120$ deg) can have a positive impact on orbit stability close to the central body. The stability regions close to the body seem to increase in size going from $e_0 = 0$ to 0.1. Eccentricities larger than 0.1 do not seem to increase stability regions significantly. Especially for orbit D, it is recommended to select an initial eccentricity of 0.1. In this way, low altitudes can be reached safely by the spacecraft in order to conduct high-resolution observations of the asteroid surface using its gamma ray and neutron spectrometer.

6.5. Analysis *C*

Lastly, results using Psyche's eighth degree and order gravity field are shown in this section. Most of the observations made and conclusions drawn from analysis *B* hold for analysis *C* as well. First, the goal is to focus on the differences and assess the validity of using a second degree and order gravity field for the characterization of stable regions near a small body. To clearly compare the results of both analyses, Figure 6.12 shows the stability plots for the nominal gravity field with initial eccentricity $e_0 = 0$ using the second and eighth degree and order gravity fields.

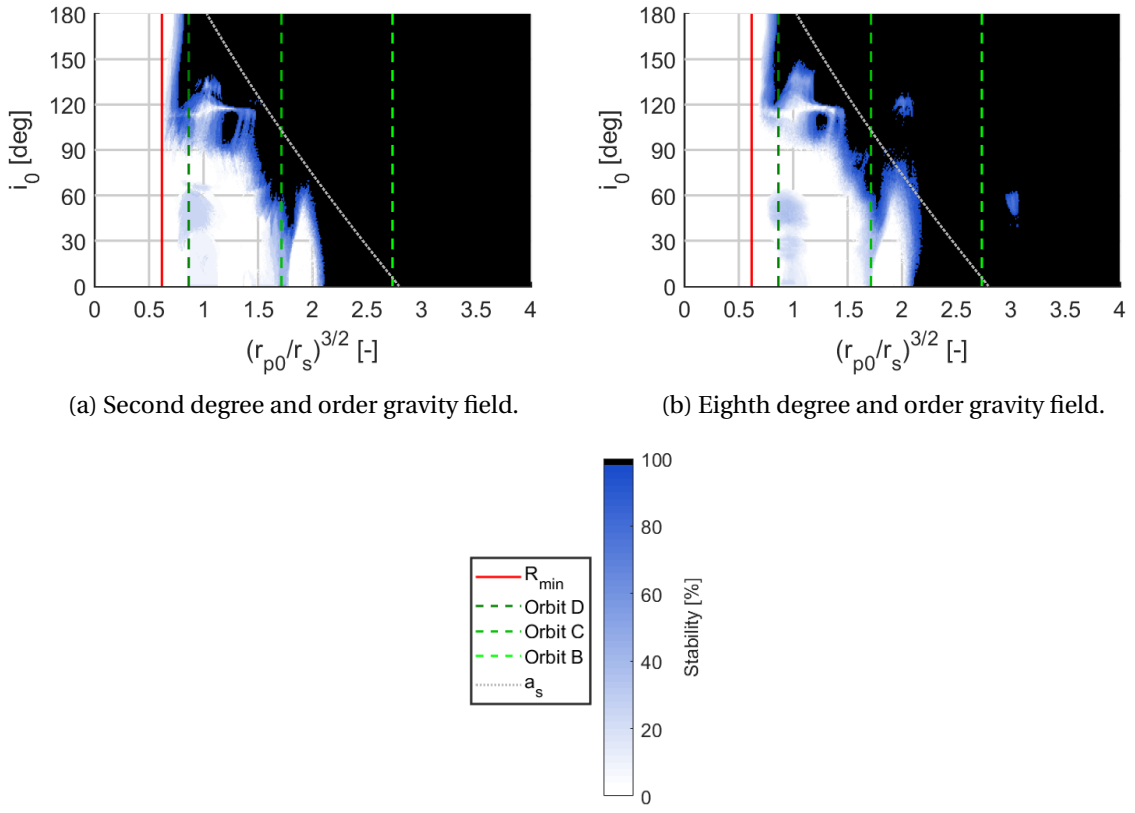

(a) Second degree and order gravity field.

(b) Eighth degree and order gravity field.

(c) Legend of stability plots.

Figure 6.12: Comparison of stability plots using a second and eighth degree and order gravity field. The stability plots are shown for Psyche's nominal gravity field and initially circular orbits ($e_0 = 0$). The empirical stability limit is also shown.

Figure 6.12 shows that the stable regions shrink when going from the low to the high degree and order gravity field. This result is expected since additional gravity terms (even though smaller in magnitude) give rise to additional perturbations causing instability. In addition to shrinking the stability regions slightly, new 'islands' of unstable orbits appear at the intersections of the critical

inclinations and the mean motion resonances. Furthermore, the empirical stability limit is not a sufficient condition in the higher degree and order gravity field due to the fact that it crosses the blue regions and islands of intermediate stability appear.

Nonetheless, it is clear that the second degree and order gravity field does an excellent job at capturing the global stability behaviour, even though its gravity field contains only two terms. By selecting orbits in the black regions using this simple gravity field, a conservative approach is taken and the corresponding color in the high degree and order gravity field will either be black or blue. Consequently, the second degree and order gravity field can successfully be used to characterize stability near a small body such as Psyche during preliminary mission design. The major advantage of using such a low degree and order gravity field is a tremendous increase in efficiency when numerically integrating trajectories and a small parameter space allowing for large parametric analyses as shown in analysis *A*. In addition, most asteroids which have not been visited by spacecraft, contain very large uncertainties in their estimated gravity-field coefficients. Therefore, assuming a higher degree and order gravity field is more accurate when compared to a lower degree and order gravity field is false.

Similar to analysis *B*, a subset of stability plots is presented using the eighth degree and order gravity field for both the nominal and conservative gravity fields and varying initial eccentricities. The results are presented in a similar fashion in Figure 6.13. Results for eccentricities $e_0 \geq 0.2$ are not presented as motivated by the discussion in the previous section.

Considering both the nominal and conservative eighth degree and order gravity fields, the polar and initially circular orbit B remains stable. Orbit C is always stable at an inclination of 90 degrees in the nominal gravity field, but not in the conservative field. There, its stability depends on Ω_0 and u_0. A very conservative mission design approach would be to select an inclination of 105 degrees for orbit C instead of the currently proposed inclination of 90 degrees, such that the orbit is stable for all Ω_0 and u_0. Similarly, orbit D is stable for $i_0 \geq 140$ deg and $e_0 = 0$ or 0.1 using the nominal gravity field for all Ω_0 and u_0. Again, this is not the case in the conservative gravity field. Firstly, it can be concluded that an initial eccentricity of 0.1 is more optimal when compared to an initial eccentricity of zero (complying with the results of Section 6.4). Secondly, i_0 must be increased from 140 to 150 deg in order for orbit D to remain stable for all Ω_0 and u_0 in the most conservative scenario.

The stability analysis can be concluded by proposing two mission scenarios for orbits C and D. The first mission scenario assumes a nominal gravity field and the second scenario is a conservative mission design approach. The proposals are presented in Tables 6.6 and 6.7 respectively along with the originally proposed science orbits by JPL (Oh et al., 2017). Finally, a candidate trajectory for orbit D is propagated in Psyche's nominal eighth degree and order gravity field for 90 days as shown in Figure 6.14. In this figure, it can be observed that the spacecraft trajectory remains stable since its eccentricity and radial distance remain bounded. Figure 6.14a shows the trajectory in the body-fixed frame of the Psyche asteroid, which clearly illustrates that the proposed trajectory allows the spacecraft to observe the majority of the asteroid surface. Furthermore, it can be seen in Figure 6.14b that the spacecraft can reach altitudes below 20 km, while still remaining stable (assuming the nominal gravity field is an accurate representation of the actual gravity field).

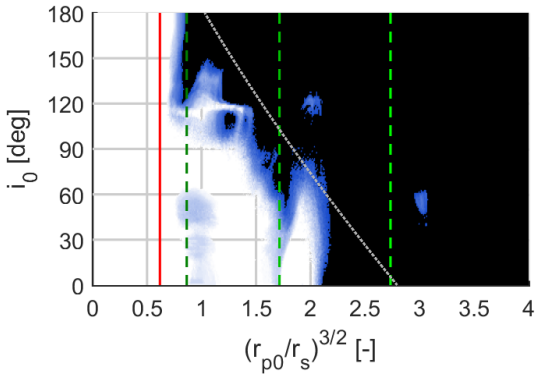

(a) Nominal gravity field, $e_0 = 0$.

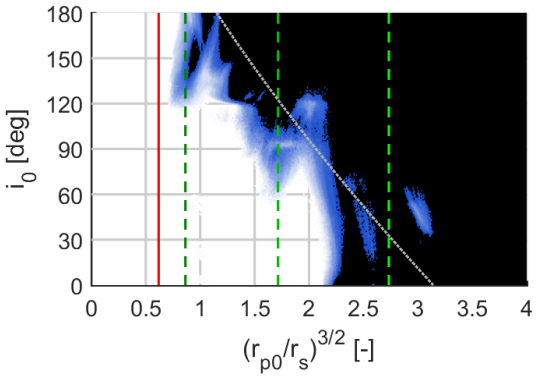

(b) Conservative gravity field, $e_0 = 0$.

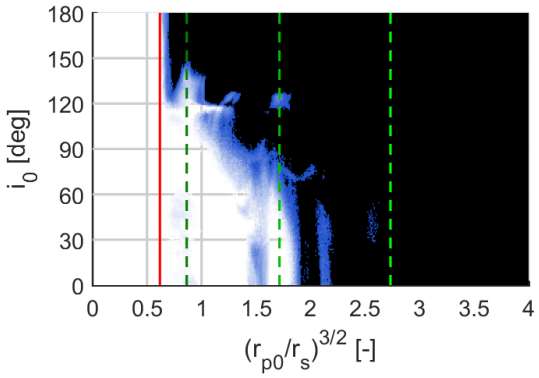

(c) Nominal gravity field, $e_0 = 0.1$.

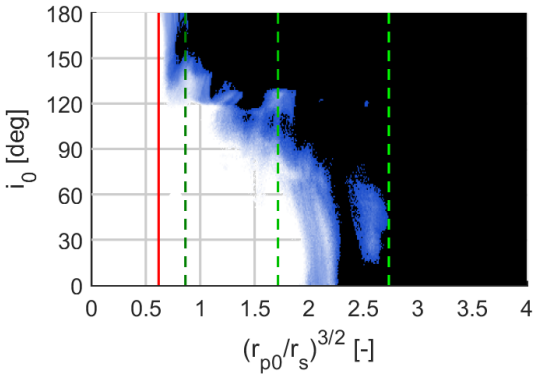

(d) Conservative gravity field, $e_0 = 0.1$.

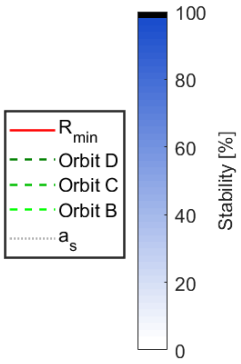

(e) Legend of stability plots.

Figure 6.13: Stable (black), intermediate (blue) and unstable (white) regions in the vicinity of asteroid Psyche in a uniformly rotating eighth degree and order gravity field.

Orbit	e_0 [-]	i_0 [deg]	a_0 [km]
C_{new}	0	90	296
C_{JPL}	0	90	296
ΔC	0	0	0
D_{new}	0.1	140	188
D_{JPL}	0	160	188
ΔD	0.1	-20	0

Table 6.6: Nominal mission design approach.

Orbit	e_0 [-]	i_0 [deg]	a_0 [km]
C_{new}	0	105	296
C_{JPL}	0	90	296
ΔC	0	15	0
D_{new}	0.1	150	188
D_{JPL}	0	160	188
ΔD	0.1	-10	0

Table 6.7: Conservative mission design approach.

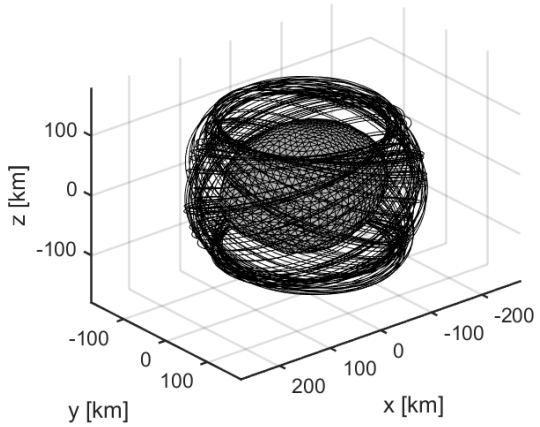

(a) Spacecraft trajectory shown in Psyche's body-fixed frame for the first 10 days of the propagation.

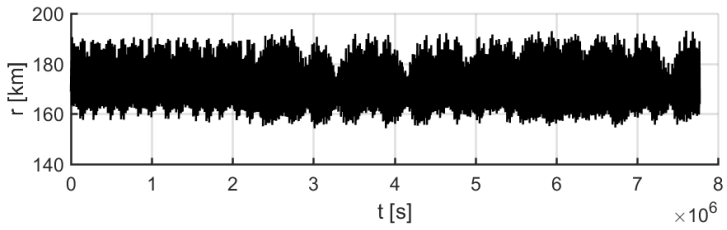

(b) Spacecraft trajectory radial distance r to Psyche's CoM as a function of time for 90 days.

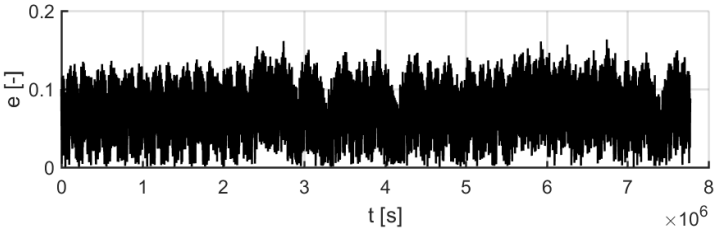

(c) Spacecraft trajectory eccentricity e as a function of time for 90 days.

Figure 6.14: Candidate trajectory for orbit D. The trajectory is propagated in the nominal eighth degree and order gravity field, where a_0 = 188 km, e_0 = 0.1, i_0 = 140 deg, Ω_0 = 0 deg, ω_0 = 60 deg and θ_0 = 0 deg.

7

Chaos Indicators

One of the research questions presented in the introduction relates to the effectiveness of using chaos indicators for the characterization of stability near an irregular body. This chapter will attempt to answer that. Firstly, Section 7.1 gives a general description and overview of chaos indicators. Secondly, Section 7.2 describes two chaos indicators and their computation in more detail, namely the FLI and its variant, the Orthogonal Fast Lyapunov Indicator (OFLI). After that, examples of regular and chaotic trajectories and their FLIs in the second degree and order gravity field are shown in Section 7.3. Finally, Section 7.4 assesses whether FLIs can be used to effectively characterize stability of orbits in the vicinity of an irregular body.

7.1. Overview

A chaos indicator is a quantitative measure of how sensitive a given trajectory is with respect to a change in its initial conditions. For two degrees of freedom systems, it can be suitable to employ techniques based on graphical treatments such as Poincaré sections. However, as the dimensionality of the system increases to three degrees and beyond (as is generally the case for satellite orbits), quantitative non-graphical methods are much more practical (Darriba et al., 2012). Chaos indicators are used to differentiate between regular and chaotic regions in the phase space. Perturbed trajectories diverging linearly from its reference can be classified as regular and those diverging exponentially can be classified as chaotic. Consequently, for a given trajectory around a central body, the evaluation of such an indicator can provide valuable information on the level of chaoticity of the orbit. Clearly, it is preferred that mission orbits show regular behaviour since chaotic trajectories (with rapid divergence from a given reference trajectory) can cost a significant amount of propellant for orbit maintenance, and possibly become uncontrollable resulting in impact on the body or escape from the system. Figure 7.1 illustrates the difference between a regular and a chaotic orbit and compares the value of the FLI (a commonly used chaos indicator) for both orbits. It can be seen that the chaos indicator attains substantially different values for the chaotic orbit when compared to the regular orbit, and can effectively be used to differentiate between regular and chaotic motion.

The foundation of characterizing (in)stability quantitatively was laid by Lyapunov (1892). In his work, Lyapunov introduced the Lyapunov Characteristic Exponents (LCEs), which are asymptotic measures of the growth rate of small deviations from a trajectory. However, considerable research on chaos indicators only initiated after the early work of Hénon and Heiles (1964). They showed that the phase space in Hamiltonian systems can be characterized by regions of regular and chaotic motion. Oseledec (1968) was the first to apply Lyapunov's theory to chaotic orbits and Benettin et al. (1980) provided a first general method of computing all LCEs of a given dynamical

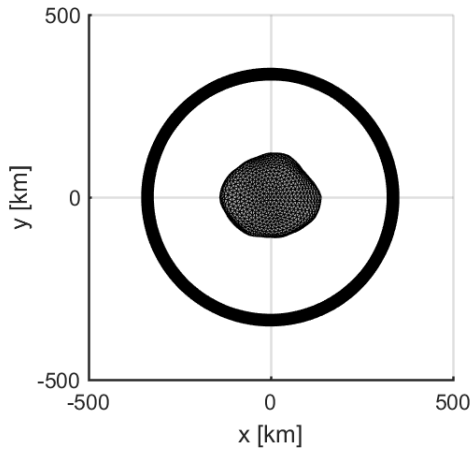

(a) Regular orbit.

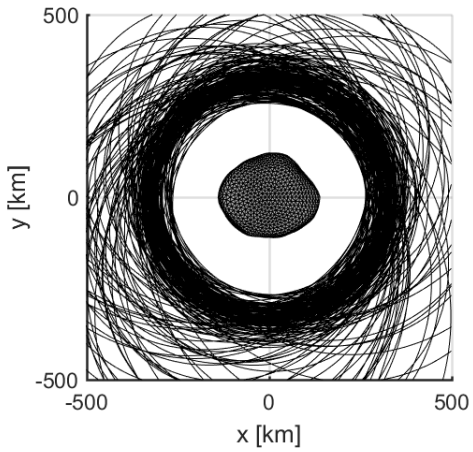

(b) Chaotic orbit.

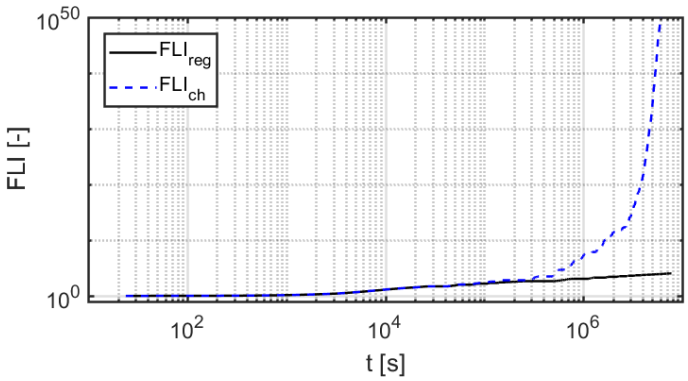

(c) Comparison of time histories of the FLI of the regular orbit (reg) and the chaotic orbit (ch).

Figure 7.1: Comparison of a regular and a chaotic orbit. These trajectories were propagated in Psyche's second degree and order gravity field in the equatorial plane. Both orbits are initially circular but differ in their initial semi-major axis.

system. The most well-known quantitative way to distinguish between regular and chaotic motion is by computing the maximum Lyapunov Characteristic Exponent (mLCE) of a given trajectory. This parameter is defined in Equation 7.1 (Skokos, 2010).

$$\chi_1 = \lim_{t\to\infty} \frac{1}{t} \ln \frac{||\boldsymbol{w}(t)||}{||\boldsymbol{w}(t_0)||} \tag{7.1}$$

In this equation, χ_1 is the mLCE and $\boldsymbol{w}(t)$ is a deviation vector at time t. Details on the computation of $\boldsymbol{w}(t)$ will be given in Section 7.2. For a regular trajectory χ_1 would be zero and for a chaotic trajectory it would equal a strictly positive value. However, since integration time is limited, only a truncated version of the LCEs can be calculated. These truncated approximations of the LCEs are referred to as the Lyapunov indicators (LIs). A major disadvantage of using LIs for chaos detection is their slow convergence to their real values (the LCEs). To make a distinction between regular and chaotic orbits, required integration times are long, resulting in a considerable computational effort. This property is especially detrimental when one has to integrate large sets of initial conditions, which is the case when globally characterizing chaoticity of a given dynamical system such as Psyche's. For a recent and extensive overview of the numerical computation of LIs, the reader is referred to Skokos (2010).

Fortunately, a variety of 'fast' chaos detection techniques has been developed over the years.

Froeschlé et al. (1997a,b) were the first to develop a chaos indicator that can discriminate between regular and chaotic motion more quickly: the FLI. A useful extension of the FLI is the OFLI, which is also able to distinguish between periodic and non-periodic orbits among regular motion by considering the component of the deviation vector(s) orthogonal to the flow (Fouchard et al., 2002). Other well-known chaos indicators are: the Mean Exponential Growth factor of Nearby Orbits (MEGNO) (Cincotta and Simó, 2000), the Smaller ALignment Index (SALI) (Skokos, 2001) and its generalization, the General ALignment Index (GALI) (Skokos, 2007), the spectral distance (D) (Voglis et al., 1999), the Relative Lyapunov Indicator (RLI) (Sándor et al., 2000) and several more. The list presented here is not exhaustive. A description or comparison of these indicators is out of scope of this research. For this, the reader is referred to the works of Maffione et al. (2011) and Darriba et al. (2012).

7.2. Fast Lyapunov Indicators

To characterize regular and chaotic motion around an irregular body, FLIs and OFLIs will be computed for large sets of initial conditions and varying gravitational parameters in the second degree and order gravity field. These chaos indicators are chosen for their ability to distinguish between regular and chaotic motion effectively, their convergence speeds, their heritage and their performance compared to other chaos indicators (see Maffione et al. (2011) and Darriba et al. (2012)). In addition, the results will be compared with the numerical study of stability presented in Chapter 6.

7.2.1. Background and Motivation

Villac and Aiello (2005) were the first to employ FLIs for the characterization of long-term stable orbits for space mission applications. In their analysis, Villac and Aiello analyzed distant retrograde orbits around Jupiter's moon Europa in the circular restricted three-body problem to find end-of-life disposal orbits. They found that FLIs can predict the long-term stability of orbits with only a relatively short integration time span. Later, Villac (2008) presented FLIs as a tool for complementing preliminary mission design by introducing the concept of FLI maps. These maps can be used by mission designers to select long-term stable orbits which are robust to model parameter perturbations. An example of such an FLI map is shown in Figure 7.2 (Villac and Aiello, 2005). In this figure, the regions of regular motion (purple) and chaotic motion (orange) can be identified very clearly. This information can be used during preliminary mission design to select regular mission orbits.

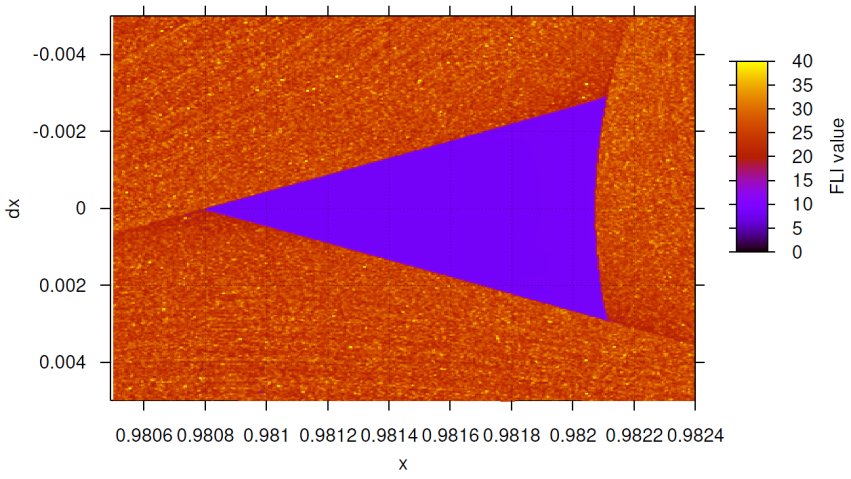

Figure 7.2: FLI map in the vicinity of a stable periodic orbit in the circular restricted three-body problem (Villac and Aiello, 2005). The purple and orange regions indicate regular and chaotic orbits respectively.

It is important to understand that the notion of stability presented in Section 6.1 is not the same as regular motion defined more strictly by Lyapunov's theory and not the opposite of chaotic motion. It will be analyzed whether FLIs and/or OFLIs provide an effective means of characterizing stability, how regions of regular motion compare with stability regions and whether the computational requirement of FLIs makes them attractive to complement preliminary mission design. In addition, this research considers orbits during the nominal mission phase of an observation mission of an irregular body with a highly-dimensional initial condition search space in the uniformly rotating two-body problem. To the best of the author's knowledge, this is a promising application of chaos indicators which has not been investigated before.

7.2.2. Variational Equations

The variational equations are the starting point of the calculation of any variational chaos indicator such as the FLI and OFLI. For any time-independent Hamiltonian system, the equations of motion can be written in first-order form as in Equation 7.2.

$$\dot{\boldsymbol{x}} = \boldsymbol{f}(\boldsymbol{x}) \tag{7.2}$$

This set of equations can be linearized to first order by introducing a Taylor-series expansion with respect to a reference trajectory according to Equations 7.3 and 7.4.

$$\boldsymbol{x} = \boldsymbol{x}^* + \delta\boldsymbol{x} \tag{7.3}$$

$$\dot{\boldsymbol{x}}^* + \delta\dot{\boldsymbol{x}} = \boldsymbol{f}(\boldsymbol{x}^* + \boldsymbol{\delta x}) \approx \boldsymbol{f}(\boldsymbol{x}^*) + \left.\frac{\partial \boldsymbol{f}}{\partial \boldsymbol{x}}\right|_{\boldsymbol{x}^*} \delta\boldsymbol{x} \tag{7.4}$$

In the equations above, $\boldsymbol{x}^*$ represent the reference trajectory and $\delta\boldsymbol{x}$ represents the deviation in the state vector (replaced by $\boldsymbol{w}$ from now on). Substituting Equation 7.2 into Equation 7.4, the first-order linear variational equations are obtained, which are given in Equation 7.5.

$$\dot{\boldsymbol{w}}(t) = \left.\frac{\partial \boldsymbol{f}(\boldsymbol{x})}{\partial \boldsymbol{x}}\right|_{\boldsymbol{x}^*(t)} \boldsymbol{w}(t) = A(t)\,\boldsymbol{w}(t) \tag{7.5}$$

Equation 7.5 represents a set of linear differential equations with respect to $\boldsymbol{w}$. This set of differential equations contains time-dependent coefficients since matrix $A(t)$ is a function of the reference trajectory $\boldsymbol{x}^*(t)$. The solution to these differential equations is given by Equation 7.6 (Skokos, 2010),

$$\boldsymbol{w}(t) = \Phi(t, t_0)\,\boldsymbol{w}(t_0) \tag{7.6}$$

where $\Phi(t, t_0)$ is known as the state transition matrix or the fundamental matrix. By substituting Equation 7.6 into Equation 7.5, it can be shown that $\Phi(t, t_0)$ satisfies Equations 7.7 and 7.8,

$$\dot{\Phi}(t, t_0) = A(t)\Phi(t, t_0) \tag{7.7}$$

$$\Phi(t_0, t_0) = I \tag{7.8}$$

where I is the identity matrix. Considering the length and time normalizations (according to Equations 3.19 and 3.20 respectively), the flow $\boldsymbol{f}$ of the dynamical system is given by Equation 7.9.

$$\boldsymbol{f} = \begin{bmatrix} \dot{x} \\ \dot{y} \\ \dot{z} \\ 2\dot{y} + V_x \\ -2\dot{x} + V_y \\ V_z \end{bmatrix} \tag{7.9}$$

In Equation 7.9, V is the effective potential of the uniformly rotating second degree and order gravity field. The full expression of V and its first- and second-order Cartesian derivatives are given in Appendix C. By taking the partial derivatives of the flow with respect to the components of the state, A can be obtained. Matrix A is given in Equation 7.10.

$$A = \begin{bmatrix} 0 & 0 & 0 & 1 & 0 & 0 \\ 0 & 0 & 0 & 0 & 1 & 0 \\ 0 & 0 & 0 & 0 & 0 & 1 \\ V^*_{xx} & V^*_{xy} & V^*_{xz} & 0 & 2 & 0 \\ V^*_{yx} & V^*_{yy} & V^*_{yz} & -2 & 0 & 0 \\ V^*_{zx} & V^*_{zy} & V^*_{zz} & 0 & 0 & 0 \end{bmatrix} \tag{7.10}$$

Now, all the ingredients are present to numerically integrate a deviation vector to a given reference trajectory in the second degree and order gravity field. It is essential that the numerical integration of the variational equations is executed simultaneously with the general equations of motion of the dynamical system. In this way, the coefficients of matrix A at time t can be computed. Therefore, the computational cost of a variational chaos indicator is always higher than a simple numerical integration of the equations of motion for a given time span and reference trajectory.

7.2.3. Definition and Computation of FLI/OFLI

First, the definition and computation of the FLI will be described, since the OFLI was introduced after the FLI and their definitions are closely related.

In their first work on FLIs, Froeschlé et al. (1997a) introduced three definitions of the FLI given in Equations 7.11, 7.12 and 7.13,

$$FLI_1(t) = \frac{1}{||\boldsymbol{w}_1(t)||^n} \tag{7.11}$$

$$FLI_2(t) = \frac{1}{\prod_{j=1}^{n} ||\boldsymbol{w}_j(t)||} \tag{7.12}$$

$$FLI_3(t) = \frac{1}{\max_{1 \le j \le n} ||\boldsymbol{w}_j(t)||^n} \tag{7.13}$$

where n is the dimension of the phase space. These definitions differ in their dependence on the choice of the initial deviation vector(s) $\boldsymbol{w}(t_0)$ and their ability to distinguish between resonant and non-resonant regular motion (Villac and Aiello, 2005). The definition in Equation 7.11 is only based on a single deviation vector. Therefore, its value has a stronger dependence on the choice of $\boldsymbol{w}(t_0)$, whereas it is computationally more efficient (since it requires the numerical integration of only one deviation vector) and able to distinguish between resonant and non-resonant regular motion.

For the purpose of this research, it is not required to distinguish between resonant and non-resonant regular motion. The most important characteristic of the FLI is that it is able to distinguish

between regular and chaotic motion effectively, independent on the choice of the initial deviation vectors. Therefore, a definition will be adopted that depends on a subset of deviation vectors rather than just a single vector. This definition is presented in Equation 7.14.

$$\begin{aligned} FLI(t) &= \max_{t_0 \leq t_i \leq t} \max_{1 \leq j \leq n} ||\boldsymbol{w}_j(t)|| \\ &= \max \left[\max_{t_0 \leq t_i \leq t} ||\boldsymbol{w}_1(t)||, \max_{t_0 \leq t_i \leq t} ||\boldsymbol{w}_2(t)||, \ldots, \max_{t_0 \leq t_i \leq t} ||\boldsymbol{w}_6(t)|| \right] \end{aligned} \tag{7.14}$$

The definition of $FLI(t)$ presented above takes the length of the largest deviation vector and the maximum length of a given deviation vector over the time history of that vector. The former reduces the dependence of $FLI(t)$ on the choice of initial deviation vector(s) and the latter is to remove the oscillatory behaviour of $||\boldsymbol{w}(t)||$. The length of a deviation vector is defined as the Euclidean norm of $\boldsymbol{w}(t)$ shown in Equation 7.15. Since the equations of motion are normalized in length and time (see Equations 3.19 and 3.20 respectively), there is no need for additional scaling between units of distance and velocity in the definition of the norm.

$$||\boldsymbol{w}|| = \sqrt{w_x^2 + w_y^2 + w_z^2 + w_{\dot{x}}^2 + w_{\dot{y}}^2 + w_{\dot{z}}^2} \tag{7.15}$$

The number of deviation vectors is taken equal to the dimensionality of the phase space of the system (here: $n = 6$). In this way, the six initial deviation vectors $\boldsymbol{w}(t_0)$ completely encompass the subspace tangent to the phase space of the system when they are chosen as a set of linearly independent vectors. Every deviation vector will evolve under the action of the largest characteristic exponent (Froeschlé et al., 1997a). However, if the dominating expanding manifold is close to being perpendicular to the set of initial deviation vectors, a transitional regime could occur during which it requires a long time before the deviation vectors align themselves with the expanding manifold. By choosing a set of n orthogonal (linearly independent) initial deviation vectors, this drawback is completely removed since there will always be at least one vector which quickly aligns itself with the expanding manifold.

The definition presented here is arbitrary and the actual value of $FLI(t)$ also depends on the integration time, the coordinate system and the metric. However, we are not interested in the absolute value of $FLI(t)$ but rather in the relative values among trajectories in order to distinguish between regular and chaotic motion. Therefore, different integration times, coordinate systems and/or metrics could be used as long as they are the same for all numerical integrations of a given system. To remain consistent, T_f is chosen to be 90 days considering the Psyche asteroid. This is the same integration time selected for the stability analyses presented in the previous chapter and corresponds to 515 central body rotations. The initial deviation vectors all have unit length and are obtained with the Gram–Schmidt orthonormalization process, which is very straightforward. For details on this routine, the reader is referred to Rice (1966). The direction of the orthonormal set of initial deviation vectors is sampled randomly for each trajectory. Each component of every initial deviation vector is sampled from a uniform distribution between -1 and 1 before executing the Gram–Schmidt orthonormalization process.

The FLI can be used to distinguish between regular and chaotic motion. However, for a continuous system, the differential rotation along the flow makes it unable for the FLI to distinguish between regular periodic and non-periodic orbits (Fouchard et al., 2002). The component of the deviation vector parallel to the flow is affected by this differential rotation and will grow at least linearly over time. By considering the components of the deviation vectors orthogonal to the flow, the

effect of differential rotation on the value of the FLI is removed. For illustrative purposes, the components of the deviation vector parallel and orthogonal to the flow are shown in Figure 7.3.

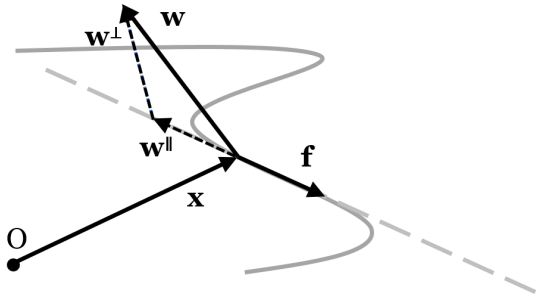

Figure 7.3: Illustration of deviation vector and its components parallel and orthogonal to the flow of the dynamical system.

Consequently, Fouchard et al. (2002) introduced the OFLI, which is able to distinguish between periodic and non-periodic regular motion as well. The definition of the OFLI adopted here is presented in Equation 7.16.

$$\begin{aligned} OFLI(t) &= \max_{t_0 \le t_i \le t} \max_{1 \le j \le n} ||\boldsymbol{w}_j^{\perp}(t)|| \\ &= \max\left[\max_{t_0 \le t_i \le t} ||\boldsymbol{w}_1^{\perp}(t)||, \max_{t_0 \le t_i \le t} ||\boldsymbol{w}_2^{\perp}(t)||, \ldots, \max_{t_0 \le t_i \le t} ||\boldsymbol{w}_6^{\perp}(t)|| \right] \end{aligned} \tag{7.16}$$

The additional computational cost of the OFLI compared to the FLI is minimal. It only requires the computation of the orthogonal component of the deviation vectors with respect to the flow. The computation of the orthogonal component is given in Equation 7.17,

$$||\boldsymbol{w}^{\perp}|| = \sqrt{||\boldsymbol{w}||^2 - \frac{(\boldsymbol{w} \cdot \boldsymbol{f})^2}{||\boldsymbol{f}||^2}} \tag{7.17}$$

where $(\cdot)$ indicates the dot product of two vectors. Even though the focus of this research is not aimed at periodic solutions, the straightforward and effortless computation of the OFLI is a compelling argument to analyze this chaos indicator as well. In addition, the OFLI has not shown to be less effective in its ability to distinguish between regular and chaotic motion when compared to the FLI (Darriba et al., 2012, Maffione et al., 2011).

Finally, it is important to point out a practical constraint when computing FLIs or OFLIs. Since the length of a deviation vector can grow exponentially under chaotic motion, numerical overflow is common. The process of renormalization is often used to omit such behaviour as thoroughly outlined by Skokos (2010). However, the only goal is to effectively distinguish between regular and chaotic motion. In case numerical overflow occurs, the value of the FLI or OFLI will be close to the maximum positive double in C++, which clearly indicates that the trajectory is chaotic. Therefore, the process of renormalization is not required and numerical overflows are allowed to occur in case of chaotic motion.

7.3. Regular and Chaotic Motion

By comparing FLI and OFLI values for regular and chaotic motion, an effective threshold can be set for these chaos indicators to distinguish between regular and chaotic motion. In addition, a brief

analysis of the time history of the deviation vectors and chaos indicators for regular and chaotic orbits partially serves as verification.

7.3.1. Comparison Regular and Chaotic Orbits

First, a comparison is made between regular and chaotic orbits. This is to illustrate the behaviour of the deviation vectors and the FLI of the orbits. It will be established whether the time history of these parameters complies with expectations. The orbits are propagated for 90 days in Psyche's nominal second degree and order gravity field with parameters σ and ν shown in Table 3.2. The initial conditions of both orbits are presented in Table 7.1. Regions of regular motion are separated very distinctly from regions of chaotic motion. Consequently, a small change in the initial conditions of the orbit can affect the behaviour of the orbit drastically as will be shown in the figures presented later on.

Parameter	Regular Orbit	Chaotic Orbit	Unit
$(a_0/r_s)^{3/2}$	1.5	1.4	-
e_0	0	0	-
i_0	70	70	deg
Ω_0	40	40	deg
u_0	135	135	deg

Table 7.1: Initial conditions of a regular and a chaotic orbit in Psyche's second degree and order gravity field.

Firstly, the trajectory of the regular orbit is shown in Figure 7.4. The time history of the length of all deviation vectors and the FLI value are shown in Figure 7.4a, the radial distance as a function of time is shown in Figure 7.4b and the trajectory in the inertial frame is shown in Figure 7.4c.

The behaviour of the regular orbit is as expected. The growth of the FLI and the length of the deviation vectors is linear, which indicates that the motion is regular. The lengths of the deviation vectors also show the anticipated oscillatory behaviour. This result complies with results from literature, which have also shown this behaviour for the lengths of the deviation vectors and the FLI in case of regular motion. Therefore, this result partially validates the correct implementation of the variational equations and the computation of the FLI. Furthermore, Figure 7.4b shows that the radial distance varies very consistent and regular over time, which is unsurprising. The stability condition presented in Section 6.1 would have indicated this orbit as stable based on the time history of the radial distance. Therefore, this specific orbit is both regular and stable, which is favorable from a mission perspective. It would be interesting to analyze in which regions of the phase space these conditions do not overlap. Are there bounded chaotic orbits and/or unbounded regular orbits and what causes these discrepancies? This will be addressed later.

The trajectory of the chaotic orbit is shown in Figure 7.5. The time history of the length of all deviation vectors and the FLI value are shown in Figure 7.5a, the radial distance as a function of time is shown in Figure 7.5b and the trajectory in the inertial frame is shown in Figure 7.5c.

The lengths of the deviations vectors of the chaotic orbit and the value of the FLI initially grow linearly until approximately 0.7 10^6 seconds (8.1 days). After this, they start to grow exponentially, indicating that the motion is chaotic. The time history of the radial distance clearly shows chaotic behaviour as well, which becomes evident after approximately 1.0 10^6 seconds (11.6 days). The spacecraft appears to be escaping from the system when analyzing the time history of the radial distance and the trajectory in the inertial frame (shown for the initial 20 days of the integration). For

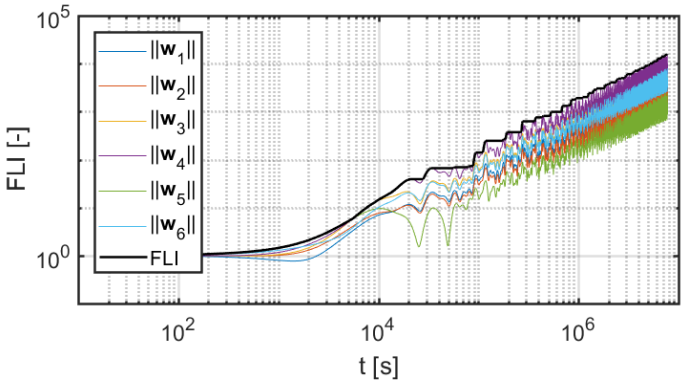

(a) Lengths of deviation vectors and FLI as a function of time.

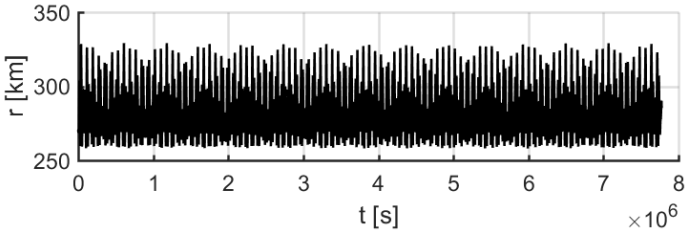

(b) Radial distance of spacecraft trajectory to CoM of Psyche as a function of time.

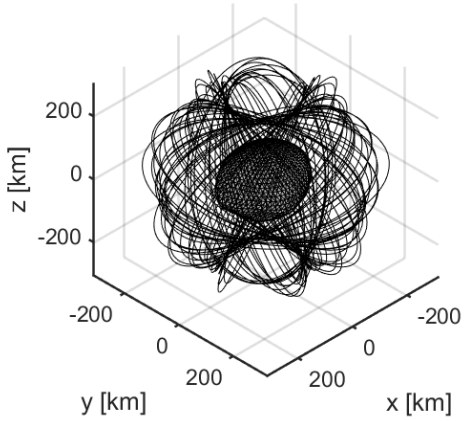

(c) Spacecraft trajectory shown in non-rotating inertial frame. The Psyche asteroid is shown stationary, but rotates uniformly in the inertial frame in reality. The trajectory is shown for the duration of the initial 20 days to avoid a cluttered plot.

Figure 7.4: Spacecraft trajectory of a regular orbit in Psyche's nominal second degree and order gravity field. The trajectory is propagated for a total duration of 90 days with initial conditions specified in Table 7.1.

this specific orbit, the FLI is able to detect chaotic motion slightly sooner compared to the stability condition utilized in the previous chapter.

Finally, a comparison of the FLI and OFLI time histories of the regular and chaotic orbits is presented in Figure 7.6.

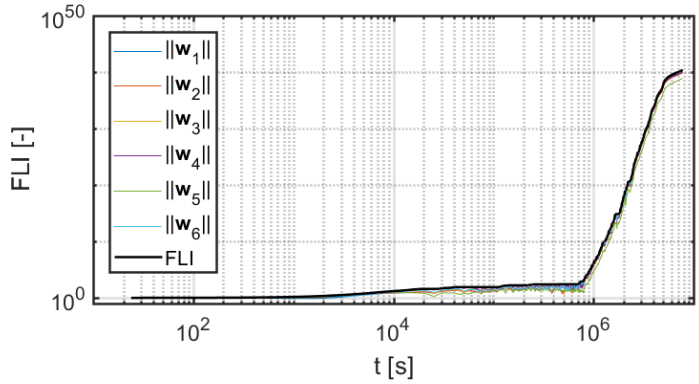

(a) Lengths of deviation vectors and FLI as a function of time.

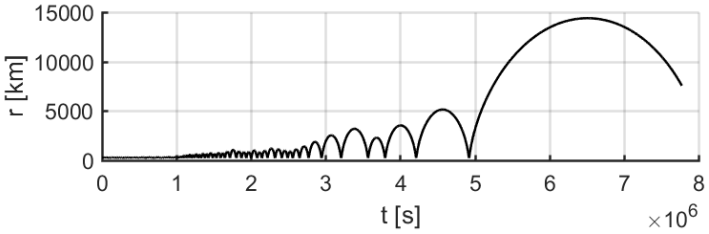

(b) Radial distance of spacecraft trajectory to CoM of Psyche as a function of time.

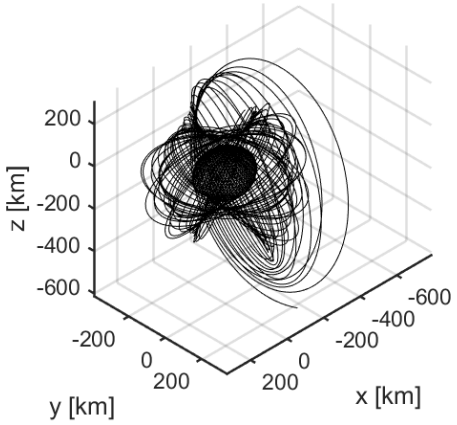

(c) Spacecraft trajectory shown in non-rotating inertial frame. The Psyche asteroid is shown stationary, but would rotate uniformly in the inertial frame in reality. The trajectory is only shown for the duration of the initial 20 days to avoid a cluttered plot.

Figure 7.5: Spacecraft trajectory of a chaotic orbit in Psyche's nominal second degree and order gravity field. The trajectory is propagated for a total duration of 90 days with initial conditions specified in Table 7.1.

Firstly, this figure shows that the discrepancies between the values of the FLI and OFLI are negligible when one has to distinguish between regular and chaotic motion. Therefore, either chaos indicator can be chosen to distinguish between regular and chaotic motion. Secondly, it is clear that the final value of the FLI/OFLI can be used to distinguish between regular and chaotic motion. The discrepancy between the final values of the FLI/OFLI is several tens of orders of magnitude. In fact, FLI maps (as the one presented in Figure 7.2) use the final value of the FLI of a given trajectory to make the distinction between regular and chaotic motion.

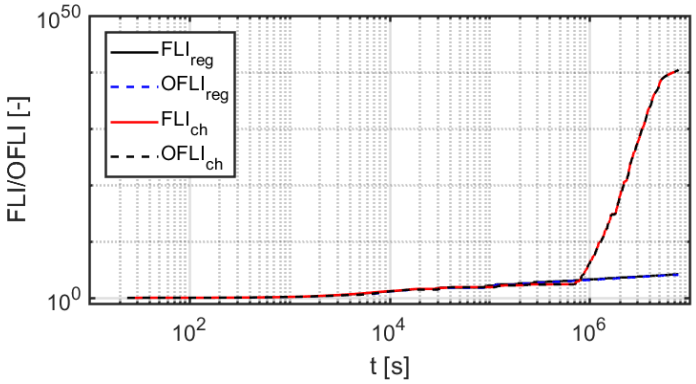

Figure 7.6: Comparison of FLI and OFLI values of regular and chaotic orbits shown in Figures 7.4 and 7.5.

7.3.2. Sampling of Initial Conditions

To generate FLI maps, large samples of initial conditions in the dynamical system must be integrated numerically for a given duration. Then, their final values can be illustrated in a 2D color plot in order to visually characterize the dynamics of the phase space. Again, the goal is to assess whether chaos indicators provide a useful complementary tool for preliminary design purposes. Therefore, a sampling scheme almost identical to analysis A will be used. Subsequently, a comparison can be made between the stability plots of analysis A (introduced in the previous chapter) and the FLI maps. In this way, the stability condition presented in Section 6.1 and an FLI threshold separating regular and chaotic motion can be compared. The sampling scheme for the FLI maps is presented in Table 7.2 (note similarity with Table 6.1).

Parameter	Sampling Range	Sampling Interval	Number of Samples	Unit
$(a_0/r_s)^{3/2}$	[0.01,4]	0.01	400	-
i_0	[0,180]	10	19	deg
Ω_0	[0,160]	20	9	deg
u_0	[0,135]	45	4	deg
ν	[0,0.2]	0.02/3	301	-
σ	0.5	-	1	-

Table 7.2: Sampling scheme of the FLI analysis. The orbital parameters of initially circular orbits are varied, as well as the second degree and order gravity-field parameters ν, while σ is kept constant at a value of 0.5. Total number of trajectories propagated: 82.4 10^6.

Note that the only discrepancy between Tables 6.1 and 7.2 is the sampling of σ, which is omitted here. The reason for fixing σ at 0.5 is to reduce computational cost. It was observed that numerical integration of the trajectory with six deviation vectors increases the computational cost by approximately a factor of seven when compared to the integration of the trajectory alone. In addition, the goal of this chapter is to assess the effectiveness of an FLI/OFLI analysis, which is completely possible while keeping σ fixed. Also, 0.5 is approximately the value of σ of the Psyche asteroid such that the FLI maps can be used to analyze orbits in the Psyche system.

7.3.3. Threshold Regular and Chaotic Orbits

To differentiate between regular and chaotic motion, use can be made of the fact the FLIs of regular orbits grow linearly over time. This proportionality is shown in Equation 7.18 (Darriba et al., 2012) and also holds for the OFLI in case of non-periodic regular motion.

$$FLI_{reg}(t) \propto t \tag{7.18}$$

Nonetheless, the rate at which the FLI of the regular orbit increases over time differs from one trajectory to another. The FLIs of regular orbits experiencing strong dynamics (orbits close to the central body) have a larger rate of change compared to orbits experiencing weaker dynamics (orbits further away from the central body). A good proxy variable to capture this discrepancy is the number of steps N executed throughout the numerical integration of the trajectory in case of variable step size integration, which will be larger for orbits experiences strong dynamics compared to orbits experiencing weak dynamics for a given set of absolute and relative error tolerances. The final value of the FLI normalized by N is deemed a better variable to distinguish between regular and chaotic motion when compared to the FLI alone. Since the final integration time is the same for all orbits, the condition for orbits to be classified as regular is shown in Equation 7.19.

$$\frac{FLI(t_{end})}{N(t_{end})} < FLI/N_{threshold} \tag{7.19}$$

In order to find an adequate value for $FLI/N_{threshold}$, $\frac{FLI(t_{end})}{N(t_{end})}$ is shown in a histogram in Figure 7.7 for all orbits with $i_0 = 0$ deg, which indicate the threshold most effectively compared to other inclinations. The full-scale histogram is shown in Figure 7.7a and a focus on the threshold is shown in Figure 7.7b.

Firstly, The histogram shows a clear discrepancy in values of $\frac{FLI(t_{end})}{N(t_{end})}$ between regular and chaotic orbits with R indicating the group of regular orbits and C_1, C_2 and C_3 indicating groups of chaotic orbits. Based on these results, $FLI/N_{threshold}$ is set to $10^{\frac{3}{2}}$. In a similar fashion, $OFLI/N_{threshold}$ can be set to $10^{\frac{1}{2}}$ (a similar histogram for OFLIs is not shown here). Secondly, distinctions can be made among the chaotic orbits. Chaotic orbits of group C_1 are orbiting the body with large irregular variations in radial distance r and do not converge towards $r = 0$ km. These chaotic orbits are usually close to regular regions of the phase space. Chaotic orbits of groups C_2 and C_3 impact the body after an unpredictable amount of time and the numerical integration breaks down as the trajectory approaches the singularity at $r = 0$ km. Even though unfavorable, this behaviour is not problematic since it only occurs for chaotic orbits. The only important result is that a clear distinction between regular and chaotic orbits is found. Finally, Group C_3 is the group of chaotic orbits that experienced numerical overflow. C++ flagged their FLIs as `+Inf`. The relative size of each group of orbits is completely dependent on the sampling scheme utilized. For each group of orbits shown in the histogram, the time history of the radial distance to the CoM of the body of an arbitrarily selected orbit is presented in Figure 7.8.

In this figure, it can be seen that orbits from group C_1 become very elliptical. The time at which orbits from groups C_2 and C_3 converge towards the center is unpredictable. Because these orbits are chaotic in nature, a small change in its initial conditions can completely change its subsequent time history.

7.4. Characterizing Stability

FLI and OFLI maps will be presented in a similar fashion as the stability plots of analysis A (see for example Figure 6.3) in order to characterize the regularity and chaoticity of orbits in the second degree and order gravity field in a global way. Then, the maps can be compared with the stability plots of analysis A, as mentioned before. Finally, its relevance as a complementary mission design tool for the Psyche mission will be shown and discussed.

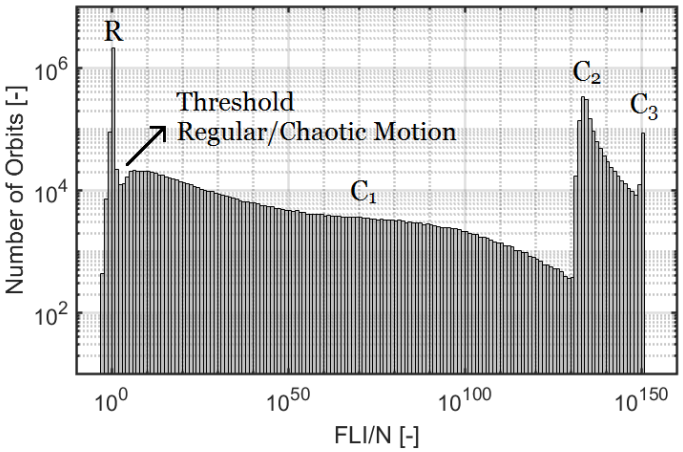

(a) Full-scale histogram.

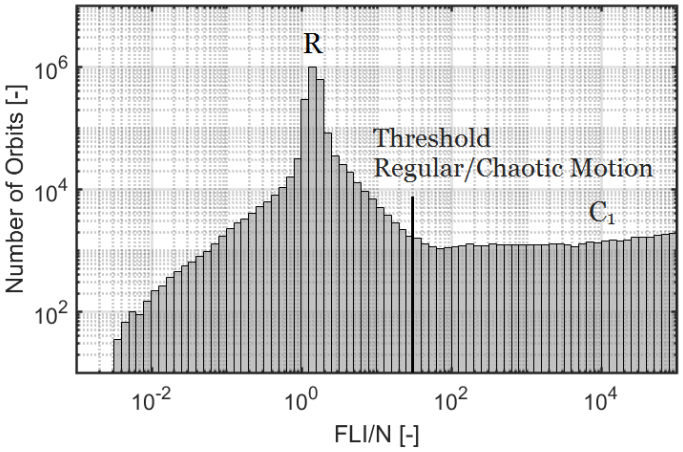

(b) Focus on threshold regular and chaotic orbits.

Figure 7.7: Histograms of final FLI values normalized with respect to the number of steps taken during the numerical integration of the trajectories. R indicates the group of regular orbits and C_1, C_2 and C_3 indicate groups of chaotic orbits. The histogram shows data for all orbits with $i_0 = 0$ deg of the sampling scheme presented in Table 7.2.

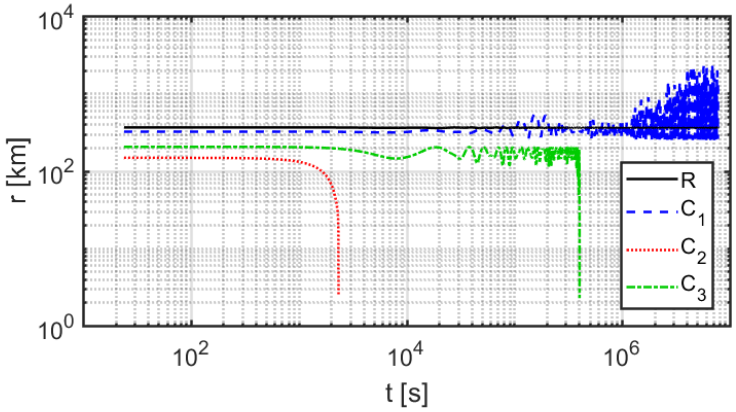

Figure 7.8: Time history comparison of the radial distance for arbitrarily selected orbits of groups R, C_1, C_2 and C_3. These groups are indicated in the histogram of Figure 7.7.

7.4.1. FLI and OFLI Maps

For all maps, the horizontal axis represents the initial semi-major axis and the parameter ν is given along the vertical axis. In this way, a total of 684 FLI and OFLI maps could be generated for each combination of i_0, Ω_0 and u_0 (see Table 7.2). However, only a few arbitrarily selected plots will be presented and their features will be discussed and compared. Figure 7.9 shows an FLI and an OFLI map for equatorial orbits with initial conditions $i_0 = 0$ deg and $\lambda_{t0} = 80$ deg. After that, Figure 7.10 shows a similar comparison for non-equatorial orbits with initial conditions $i_0 = 140$ deg, $\Omega_0 = 0$ deg and $u_0 = 90$ deg. The lower and upper boundaries of the color scale for all maps are fixed at $10^{-7/2}$ and $10^{3/2}$ respectively. This ensures a focus on the regular orbits. Since the upper boundary is set at $10^{3/2}$, the chaotic region has a dark red color. For the OFLI maps, the upper boundary could be set at $10^{1/2}$, since this value would be the optimal threshold for OFLIs as mentioned before. However, equal color scales were chosen to ensure a clear comparison between the FLI and OFLI maps.

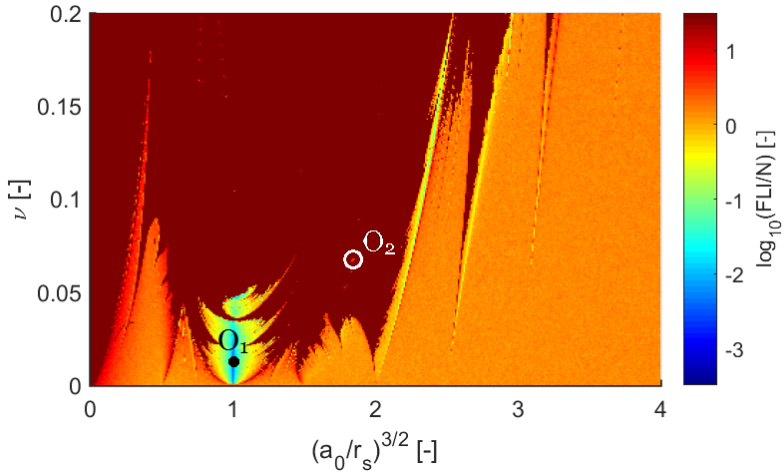

(a) FLI map.

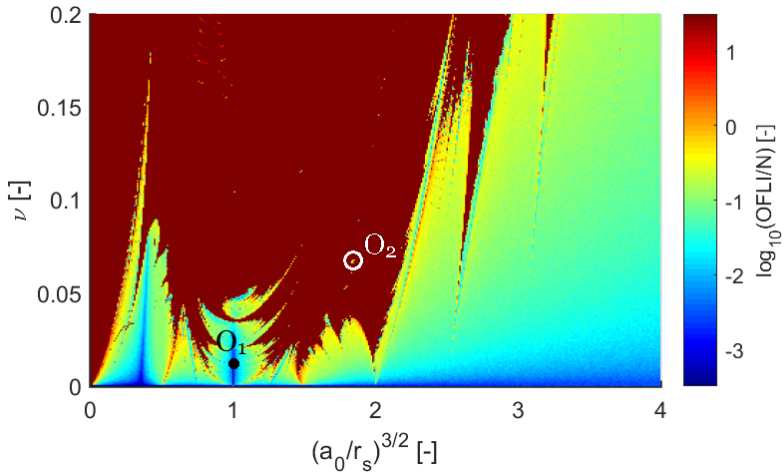

(b) OFLI map.

Figure 7.9: Comparison of FLI and OFLI map for orbits propagated in the second degree and order gravity field with parameters: $\sigma = 0.5$, $i_0 = 0$ deg and $\lambda_{t0} = 80$ deg.

Firstly, it can be observed that mean motion resonances with the asteroid rotation are correlated with chaotic regions. This behaviour is similar to the stability plots presented in the previous

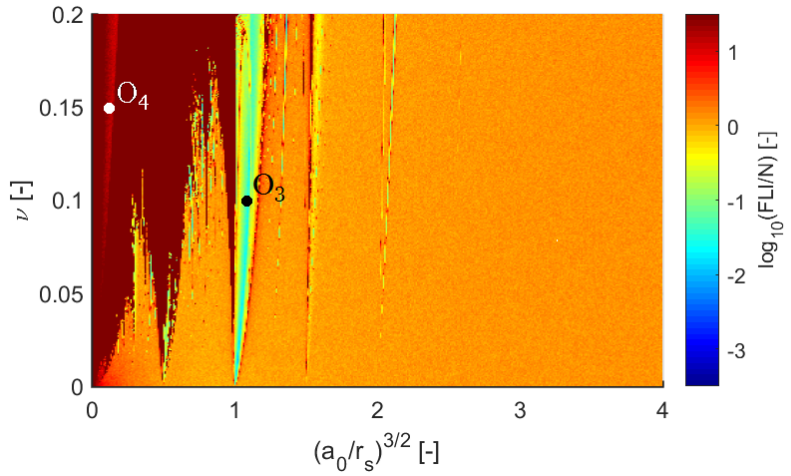

(a) FLI map.

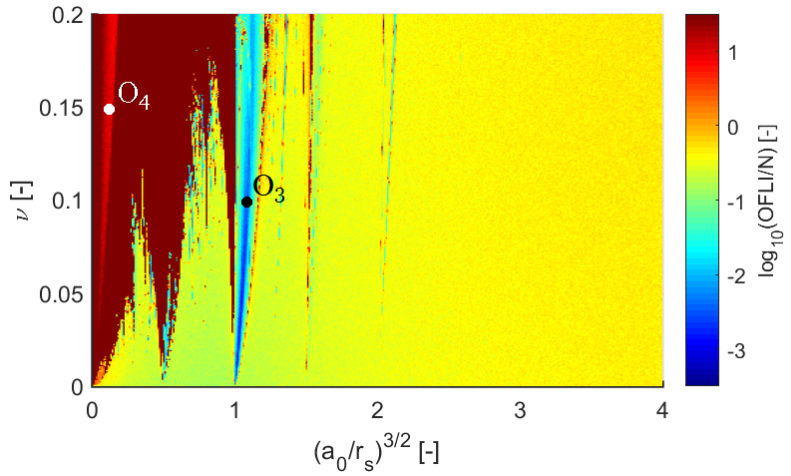

(b) OFLI map.

Figure 7.10: Comparison of FLI and OFLI map for orbits propagated in the second degree and order gravity field with parameters: $\sigma = 0.5$, $i_0 = 140$ deg, $\Omega_0 = 0$ deg and $u_0 = 90$ deg.

chapter. Generally, there are strong similarities in the structures of the FLI and OFLI maps and the BIBO-stability plots, influenced by these resonances. Comparing Figures 7.9 and 7.10, the size of chaotic regions increases with decreasing inclination, decreasing semi-major axis and increasing irregularity of the body. Also, the maps show a distinct boundary between regular and chaotic motion, which was identified in the histogram of Figure 7.7.

Secondly, FLI and OFLI maps show structures caused by resonances with more detail compared to the stability plots presented in the previous chapter. The color plots allow a clearer identification of resonant orbits (see subtle 2:1 resonance in Figure 7.10). In addition, FLI and OFLI maps can be used to identify families of quasi-periodic orbits in the body-fixed frame. In Figures 7.9a and 7.10a, regions with a more blue color (and lower final values of $\frac{FLI}{N}$ or $\frac{OFLI}{N}$) among the regular orbits can indicate the presence of quasi-periodic orbits. For example, a region of distinctly lower values of $\frac{FLI}{N}$ and $\frac{OFLI}{N}$ can be identified at the 1:1 resonance in both figures. One orbit from Figure 7.9 (orbit 1) and one orbit from Figure 7.10 (orbit 3) within these regions are shown in the body-fixed frame in Figure 7.11a. The time history of their FLI and OFLI is shown in Figure 7.11b.

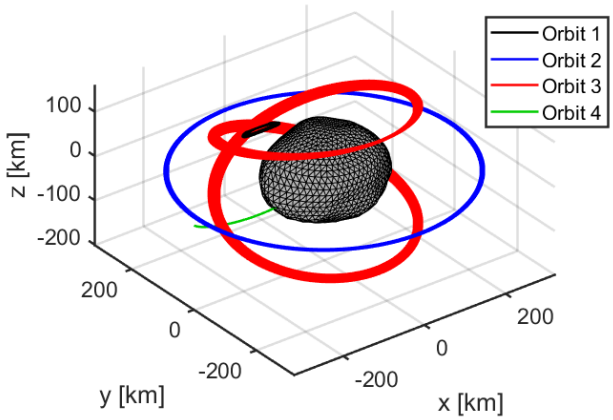

(a) Trajectories of orbits 1 through 4 shown in the uniformly rotating frame. The shape of the Psyche asteroid is shown for illustrative purposes. However, ν for these orbits does necessarily correspond with a realistic value of ν for the Psyche asteroid.

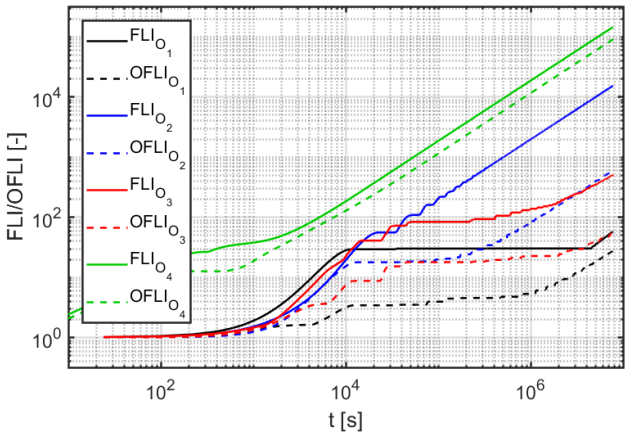

(b) Time history of FLI and OFLI values of orbits 1 through 4.

Figure 7.11: Trajectories and time histories of FLI and OFLI values shown for orbits 1 through 4. Initial conditions in the uniformly rotating second degree and order gravity field are given in Table 7.3.

From the trajectories shown in the body-fixed frame, it is clear that orbits 1 and 3 are quasi-periodic orbits. It was possible to identify these quasi-periodic orbits because the values of their FLI and OFLI started increasing linearly only after a considerable amount of integration time resulting in lower final $\frac{FLI}{N}$ and $\frac{OFLI}{N}$ values compared to other orbits. Orbit 1 corresponds to a stable quasi-periodic orbit about one of the stable equilibria, similar to the orbits presented in Figure B.3. Furthermore, several isolated islands of regular motion can be identified in Figure 7.9. A quasi-periodic orbit from one of these islands (orbit 2) is presented in Figure 7.11. Figure 7.10 also shows a distinct regular structure in the top left corner of the plot. This region corresponds to orbits that escape almost immediately from the system. Because of their rapid escape, their FLI or OFLI values do not have the time to grow considerably during the initial phase when the trajectory is chaotic and the spacecraft is still orbiting the body. Orbit 4 is an example of such a trajectory. Due to the ellipticity of the body, a large momentum exchange occurs between the rotating body and the spacecraft that causes the trajectory of the spacecraft to become hyperbolic almost immediately within the time

period of one orbital revolution. The initial conditions of orbits 1 through 4 are given in Table 7.3. Refer to Figures 7.4 and 7.5 for a comparison of a standard regular orbit and a chaotic orbit respectively.

Parameter	Orbit 1	Orbit 2	Orbit 3	Orbit 4	Unit
$(a_0/r_s)^{3/2}$	1.0	1.84	1.09	0.12	-
e_0	0	0	0	0	-
i_0	0	0	140	140	deg
Ω_0	-	-	0	0	deg
u_0	-	-	90	90	deg
λ_{t0}	80	80	-	-	deg
ν	0.018	0.0667	0.1	0.15	-

Table 7.3: Initial conditions of orbits 1 through 4 indicated in Figures 7.9 and 7.10 and shown in Figure 7.11.

Finally, something can be said about the difference between the FLI and OFLI maps. As mentioned before, the OFLI is different from the FLI in the sense that it only considers the orthogonal component of the deviation vectors to the flow in its computation. Therefore, OFLI values are always smaller than FLI values for a given orbit. This is clear when comparing the color of the OFLI maps to the FLI maps in Figures 7.9 and 7.10 (discrepancy is too small to be observable in Figure 7.6). Because of this, the OFLI is able to distinguish between periodic and non-periodic orbits. Comparing Figures 7.9a and 7.9b, it can be seen that the OFLI map shows much more contrast among the regular orbits compared to the FLI map. Circular equatorial orbits around a body with a value of ν close to zero, will remain quasi-circular since $\nu = 0$ corresponds to point-mass gravity. The OFLI map of Figure 7.9b successfully identifies periodic orbits at $\nu = 0$. In Figure 7.10, the OFLI map does not provide additional information simply because there are no (or close to no) periodic orbits in those maps. A family of quasi-periodic orbits was identified, but it was also possible to identify these orbits with the FLI map. The cause of the increased contrast in Figure 7.9b is the fact that these orbits are equatorial. When orbits are non-equatorial, periodic orbits are less common since inclined orbits have two additional degrees of freedom (position and velocity) along the z-direction that need to map onto itself in order to be periodic. In addition, non-equatorial circular orbits around a point mass are generally non-periodic in the rotating frame. Therefore, the advantage of using OFLI maps instead of FLI maps for a systematic global analysis is minor.

Only a tiny subset of FLI and OFLI maps and orbits have been illustrated and discussed. The analysis presented here is kept brief due to the sheer size of the search space. The objective is to show how FLI and OFLI maps can be used to characterize regular and chaotic motion in the small-body problem and to demonstrate their intuitive characteristics that can be leveraged for preliminary mission design purposes. Major advantages of FLI and OFLI maps that were identified are their ability to distinguish between different types of regular motion among the regular orbits (specifically the identification of families of quasi-periodic orbits) and their ability to distinguish between regular and chaotic motion effectively.

7.4.2. Comparison BIBO- and FLI-Stability Conditions

So far, two methods have been introduced to classify the stability of orbits in the uniformly rotating second degree and order gravity field: a method based on BIBO-stability and a method based on the expansion of deviation vectors in the tangent subspace using FLIs and OFLIs. A systematic comparison of both methods in the small-body problem is currently lacking from literature. In order to compare both methods, stability maps using both methods can be overlaid. By doing so, it is

possible to effectively identify in which regions of the phase space the conditions conform (regular, BIBO-stable orbits and chaotic, BIBO-unstable orbits) and more interestingly, where these conditions do not conform (regular, BIBO-unstable orbits and chaotic, BIBO-stable orbits). To distinguish between regular and chaotic motion, the final $\frac{FLI}{N}$ value is used with a threshold of $10^{3/2}$ as mentioned before. To distinguish between BIBO-stable and -unstable orbits, Equation 6.4 is used.

The stability plots presented here were selected for two reasons: they show the largest regions of discrepancy between both conditions and they show the largest diversity of orbits that lie within these regions. Figures 7.12a, 7.12b and 7.12c present three comparative stability plots at inclinations 40, 120 and 160 degrees respectively.

It can be observed that both conditions result in remarkably similar stability plots. Note that these plots were specifically chosen to show large regions of discrepancy. For most stability plots that were generated, regions of regular orbits and BIBO-stable orbits conform even better. The plots also show that for inclinations smaller than approximately 140 degrees and semi-major axes larger than the 1:1 resonance radius, the $\frac{FLI}{N}$ condition is more conservative and shows the mean motion resonances with more detail compared to the BIBO-stability condition of Equation 6.4 (see green regions). In contrast, there are several large regions of regular, BIBO-unstable orbits around and below the 1:1 resonance radius.

As was already identified in the previous subsection, the red region in the top left corner of Figure 7.12b corresponds to orbits escaping rapidly from the system. In order to also understand the cause of the other discrepancies, four orbits are sampled in those regions. Orbits 5, 7 and 8 are sampled in regular, BIBO-unstable regions and orbit 6 is sampled in a chaotic, BIBO-stable region. The initial conditions of these orbits are presented in Table 7.4 and their radial distance and FLI values as a function of time are shown in Figures 7.13a and 7.13b respectively. The initial conditions of these orbits are also indicated in Figure 7.12.

Parameter	**Orbit 5**	**Orbit 6**	**Orbit 7**	**Orbit 8**	**Unit**
$(a_0/r_s)^{3/2}$	0.65	2.0	0.95	1.05	-
e_0	0	0	0	0	-
i_0	40	40	120	160	deg
Ω_0	0	0	0	0	deg
u_0	0	0	90	0	deg
ν	0.06	0.04	0.04	0.112	-

Table 7.4: Initial conditions of orbits 5 through 8 indicated in Figures 7.12a, 7.12b and 7.12c and shown in Figure 7.13.

Figure 7.13b shows that orbits 5, 7 and 8 can be be classified as regular since their FLIs grow linearly over time. The regularity of these orbits is also clear from Figure 7.13a. Although regular, the amplitudes of the oscillations in radial distance of these orbits are so large, that they exceed the BIBO-stability condition of Equation 6.4. By increasing the range between r_{max} and r_{min}, orbits in the red regions (excluding the top left region of Figure 7.12b) would be classified as regular and BIBO-stable as well. It depends on mission design requirements whether one wants to consider orbits with strong oscillations in radial distance as well. However, it became clear that most of the regions classified as regular and BIBO-unstable are in fact BIBO-stable with relaxed constraints. This is a remarkable result as it shows that both conditions are very strongly correlated in their classification of stable and unstable orbits. Figure 7.14 shows this by comparing Figure 7.12b with the original BIBO constraint (on the left) and a relaxed BIBO constraint (on the right) with $r_{min} = 0.5a_0(1-e_0)$

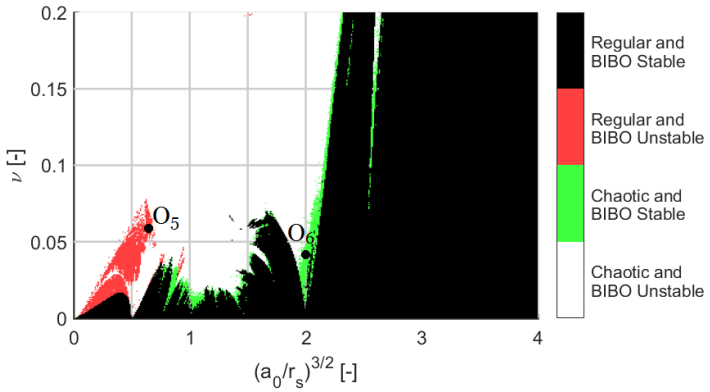

(a) i_0 = 40 deg, Ω_0 = 0 deg and u_0 = 0 deg.

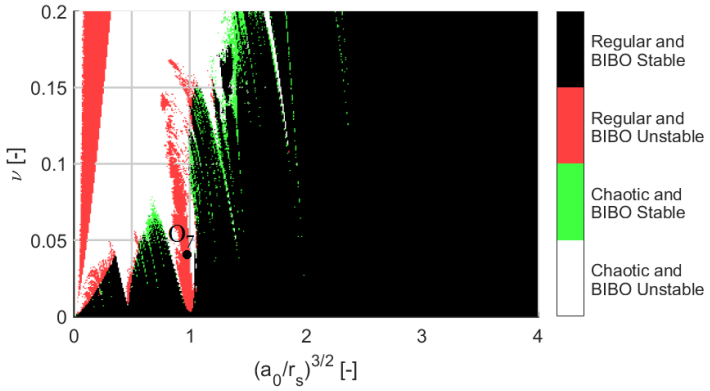

(b) i_0 = 120 deg, Ω_0 = 0 deg and u_0 = 90 deg.

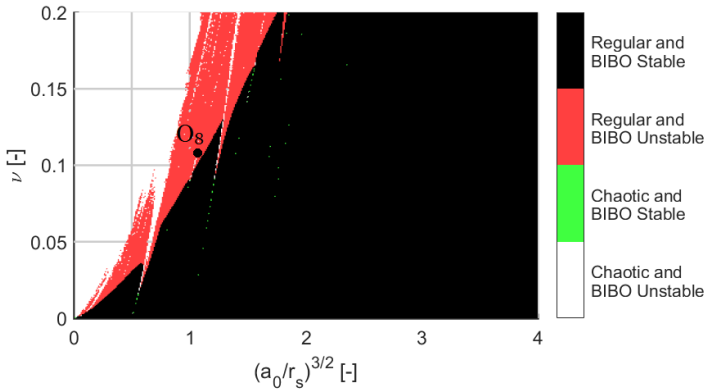

(c) i_0 = 160 deg, Ω_0 = 0 deg and u_0 = 0 deg.

Figure 7.12: Stability plots in the uniformly rotating second degree and order gravity field. A comparison is made between conditions of BIBO-(in)stability and the regularity/chaoticity or orbits.

and $r_{max} = 2.0a_0(1+e_0)$.

Orbit 6 is classified as chaotic and BIBO-stable. Figure 7.13b shows that the FLI of orbit 6 grows exponentially with time (which confirms the chaoticity of the orbit) and Figure 7.13a shows that the orbit is bounded during the integration time period of 90 days (which confirms the classification of BIBO-stability of the orbit). Only after integrating the orbit for a duration of 450 days, the chaotic nature becomes apparent in the time history of its radial distance. This is shown in Figure 7.15.

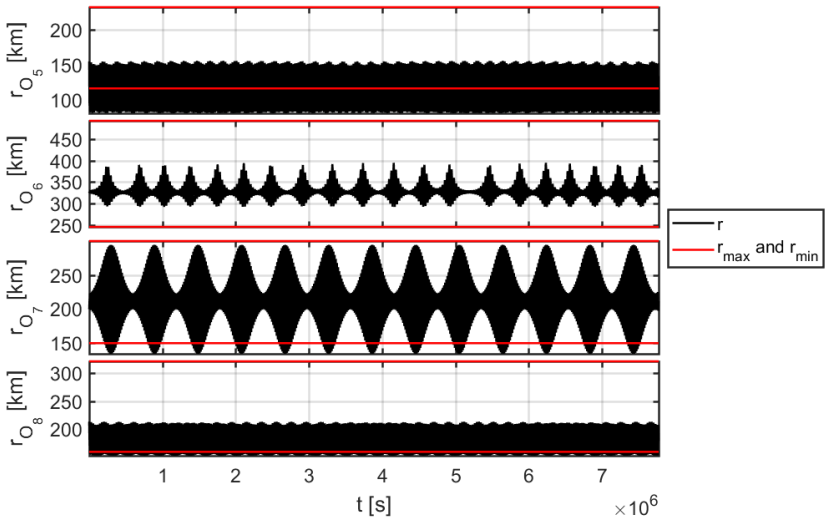

(a) Time history of radial distance to center of body of orbits 5 through 8.

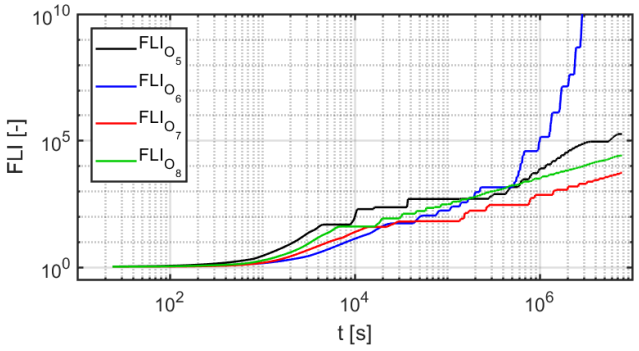

(b) Time history of FLI values of orbits 5 through 8.

Figure 7.13: Time histories of radial distance to center of body and FLI values shown for orbits 5 through 8. Initial conditions in the uniformly rotating second degree and order gravity field are given in Table 7.4.

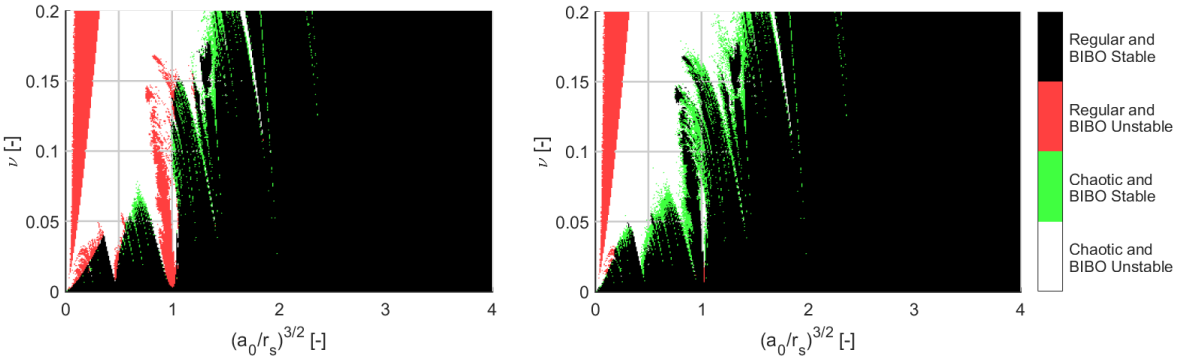

(a) BIBO condition with $r_{min} = 0.75a_0(1-e_0)$ and $r_{max} = 1.5a_0(1+e_0)$.

(b) BIBO condition with $r_{min} = 0.5a_0(1-e_0)$ and $r_{max} = 2.0a_0(1+e_0)$.

Figure 7.14: Comparison of stability plots with the original BIBO-stability condition and a relaxed version of it for $i_0 = 120$ deg, $\Omega_0 = 0$ deg and $u_0 = 90$ deg.

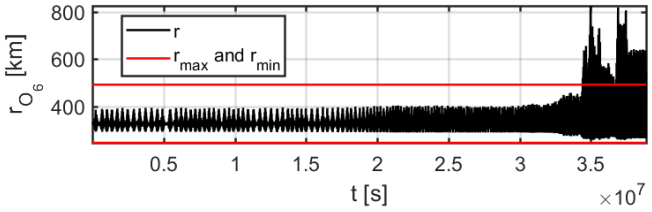

Figure 7.15: Radial distance with respect to center of body as a function of time of orbit 6. The integration time is extended from 90 days to 450 days. The initial conditions of orbit 6 are presented in Table 7.4.

The FLI was able to detect the chaotic nature of orbit 6 much more quickly compared to the BIBO-stability condition. The green regions shown in Figure 7.13 are orbits that are chaotic and might become BIBO-unstable if the integration time is increased. By only using BIBO-stability conditions in the mission design process, the chaotic nature of orbits such as orbit 6 might not be identified. In addition, under neglected or unforeseen perturbations, orbit 6 might become BIBO-unstable much more quickly which would result in an unsafe trajectory.

These results clearly demonstrate the advantage of using chaos indicators like the FLI or OFLI as a stability characterization method. Consequently, it is highly recommended to use FLI maps as a complementary mission design tool to effectively characterize regions of regular and chaotic motion. Relying solely on a BIBO-stability detection method can result in classifying chaotic orbits as stable. For this particular system (the uniformly rotating second degree and order gravity field), it was found that additionally integrating six deviation vectors increased the computational effort by a factor of 7 approximately. Nonetheless, the advantage of computing chaos indicators outweighs the additional computational cost. Furthermore, this factor can be decreased by decreasing the number of deviation vectors (6 is a conservative maximum) or decreasing the integration time (chaos indicators detect instability sooner and more effectively). A combination of a BIBO-stability condition with the computation of a chaos indicator such as the FLI or OFLI is recommended for mission design purposes.

7.4.3. Psyche Mission

Finally, stability plots similar to those shown in Figure 6.9 can be generated. Now, the stability condition is based on the regularity or chaoticity of the orbits using a final $\frac{FLI}{N}$ value of $10^{3/2}$ as threshold. For each plot, 36 individual FLI maps are overlaid for all combinations of Ω_0 and u_0 or λ_{t0} given in Table 7.2. Since $\sigma = 0.5$ is approximately the value of the Psyche asteroid, these stability plots can be used to analyze which initially circular orbits in Psyche's nominal and conservative gravity fields are regular for a large variety of initial conditions. The stability plots at inclinations similar to Figure 6.9 are shown in Figure 7.16.

It can be observed that Orbit B is regular for all combinations of Ω_0 and u_0 at the proposed inclination of 90 degrees. Therefore, orbit B is both BIBO-stable and regular in the second degree and order gravity field. The same holds for orbit C, which is both regular and BIBO-stable at $i_0 = 90$ deg. Nonetheless, the margin is small considering the conservative gravity field and orbits are not always regular for intermediate values of ν. Again, it might be required to select a slightly higher inclination for orbit C in order to ensure its regularity (and BIBO-stability). This will only affect observability of the asteroid slightly. Finally, to ensure regularity of Orbit D in both gravity fields, an inclination beyond 140 degrees is recommended, which complies with the recommendations given in Chapter 6.

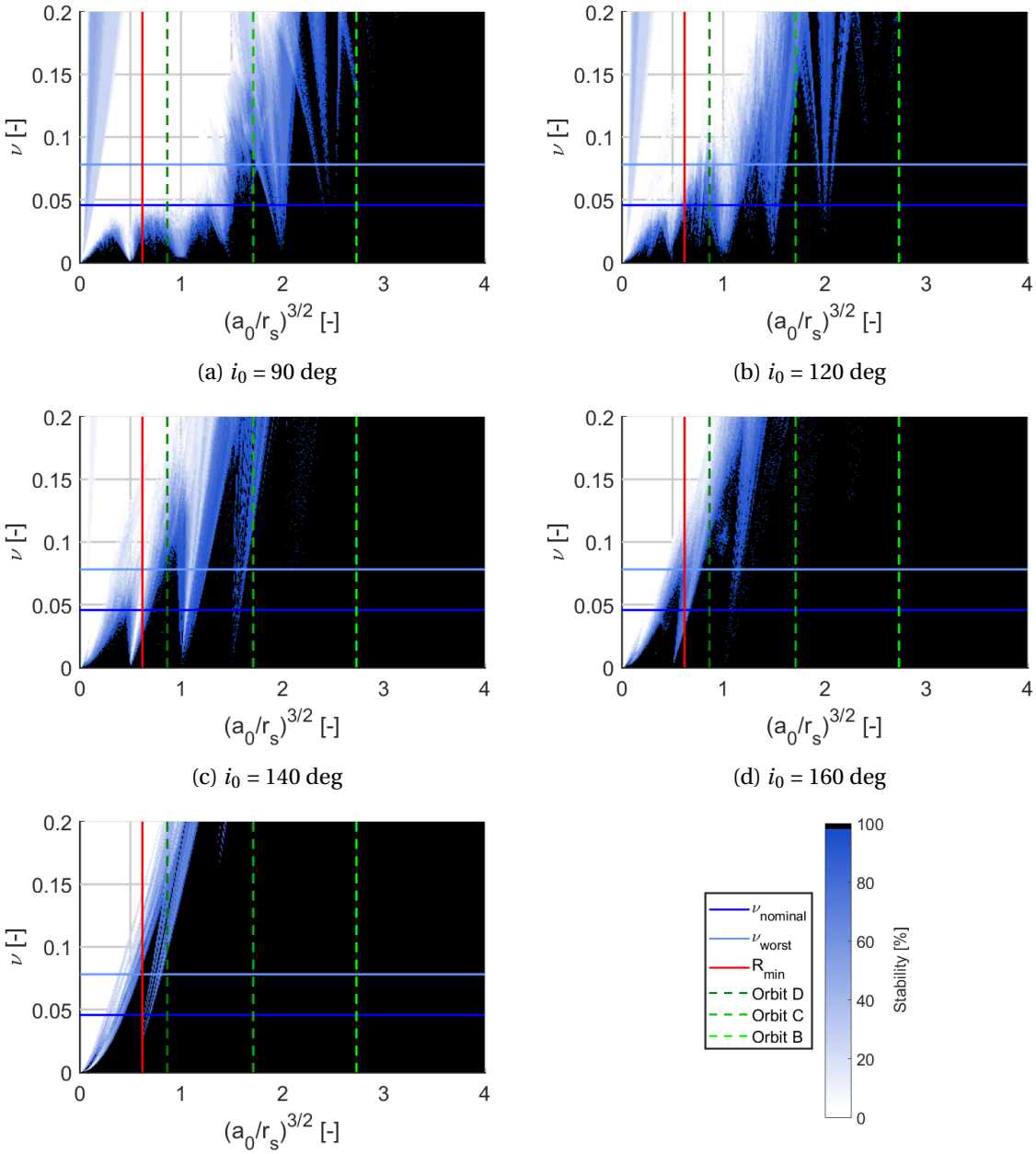

(a) i_0 = 90 deg

(b) i_0 = 120 deg

(c) i_0 = 140 deg

(d) i_0 = 160 deg

(e) i_0 = 180 deg

(f) Legend of stability plots.

Figure 7.16: Stable (black), intermediate (blue) and unstable (white) regions in a uniformly rotating second degree and order gravity field, where σ = 0.5 and i_0 varies for each plot.

Again, it has been shown that FLI maps can be a very attractive and valuable tool during the preliminary design stage of a space mission. This has been demonstrated by validating the regularity of the Psyche mission science orbits.

8

Verification and Validation

Verification and validation are essential processes when developing software. They aim to answer two different questions:

- Verification: Are we building the product right?
- Validation: Are we building the right product?

In terms of software development, verification aims to check whether the software is free of any bugs or internal errors, which can often be checked with simple tests and/or comparison with analytical results. Validation on the other hand, is executed on a higher level in the problem space and checks whether the right problem is solved. This can be achieved by analyzing whether the obtained results are consistent with results obtained by other tools or results presented in literature.

Since verification is intertwined with the software development process and culminates into validation as the software matures, this chapter will focus on presenting the validation of the software tool. Firstly, Section 8.1 compares the numerical integration of trajectories in the second and eighth degree and order gravity fields of the tool developed in C++ to JPL's SBDT. Secondly, the results of the BIBO-stability analysis are validated by comparing them to equivalent results presented in Hu and Scheeres (2004) in Section 8.2. Finally, an effort is made towards validation of the FLI and OFLI maps by comparing values of second-order derivatives of the potential obtained by the tool in C++ and *Wolfram Mathematica* and by discussing the behaviour of the FLI and OFLI in Section 8.3.

8.1. Comparison with Small-Body Dynamics Toolkit

Using SBDT presented in Section 5.1, trajectories integrated by the tool developed in C++ can be validated. This is done with Psyche's nominal second and eighth degree and order uniformly rotating gravity fields. In total, two orbits are integrated using the tool developed in C++ and SBDT: an equatorial orbit and an inclined orbit. Each orbit is integrated in the second and eighth degree and order gravity fields. The initial conditions of both orbits are presented in Table 8.1 and are chosen such that they represent two very distinct regular orbits.

Each orbit is integrated numerically for 10 days with absolute and relative error tolerances set at 10^{-15} in SBDT and C++ (assuming normalized equations of motion). In this way, the step error approaches double precision. The time history of Δr and ΔV is used to assess the validity of the integration in C++. These parameters represent the magnitude of the difference in position and

Parameter	Equatorial Orbit	Inclined Orbit	Unit
a_0	500	900	km
e_0	0.2	0.6	-
i_0	0	140	deg
$\bar{\omega}_0$	320	-	deg
Ω_0	-	70	deg
ω_0	-	190	deg
θ_0	50	260	deg

Table 8.1: Initial conditions of equatorial and inclined orbits used for validation purposes.

velocity vectors of a given orbit between the trajectories obtained in SBDT and C++. The state difference is illustrated in Figure 8.1.

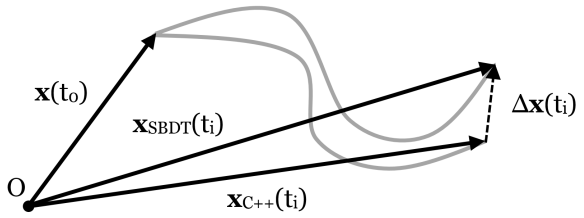

Figure 8.1: Vector $\Delta \boldsymbol{x}$ represents the difference between the states of a trajectory integrated in SBDT and C++.

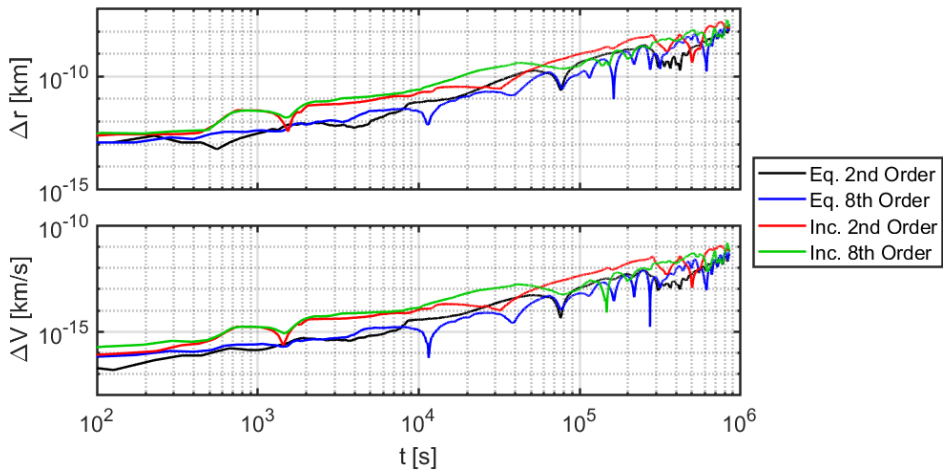

Figure 8.2: Time histories of Δr and ΔV for orbits integrated numerically using SBDT and the C++ tool. The initial conditions of the orbits are presented in Table 8.1.

The results presented in Figure 8.2 clearly show that the discrepancies in position and velocity between the orbits in SBDT and the C++ tool are extremely small. In fact, when computing the average step error, it can be shown that the origin of the discrepancies is a combination of integration and round-off errors. These results validate the correct implementation of the second and eighth degree and order spherical harmonics gravity fields, the normalized equations of motion and the implementation of the RKF78 integrator in C++. In addition, Figure 8.3 presents the relative Jacobi constant error made throughout the numerical integrations in the second degree and order gravity field for both orbits in SBDT and C++. Since the Jacobi constant is a conserved quantity in the uniformly rotating gravity field, ΔC_J is defined in Equation 8.1.

$$\Delta C_J(t) = \frac{C_J(t) - C_J(t_0)}{C_J(t_0)} \tag{8.1}$$

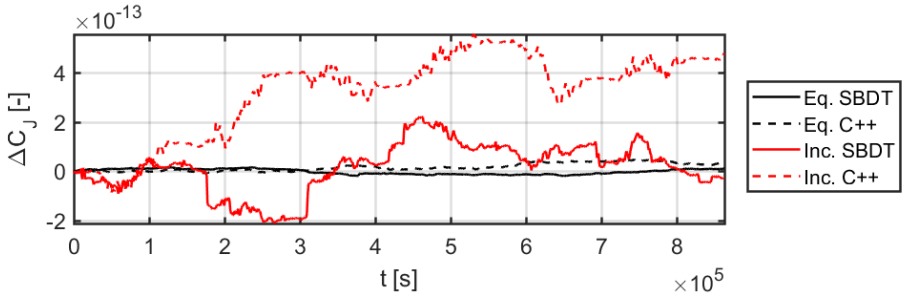

Figure 8.3: Time histories of relative Jacobi constant errors for orbits integrated numerically using SBDT and the C++ tool. The initial conditions of the orbits are presented in Table 8.1.

This figure again confirms that the equations of motion are integrated correctly in the second degree and order gravity field. The discrepancy between the equatorial orbit error and inclined orbit error is caused by the larger eccentricity of the inclined orbit, which makes the numerical integration more difficult (problem is more stiff).

8.2. BIBO-Stability Analysis

Since this research builds upon the initial work of Hu and Scheeres (2004), the results presented in their paper can be reproduced as a means of validating the stability plots. Hu and Scheeres (2004) present two stability plots (for $\sigma = 0.5$ and $\sigma = 1.0$) for orbits initialized with $e_0 = 0$, $i_0 = 0$ and $\lambda_{t0} = 0$. In their analysis, orbits are flagged as unstable if $\Delta e > \Delta e_{max}$ over the course of the trajectory, where Δe_{max} ranges between 0.2 and 0.6 (characteristics of results do not change strongly as a function of Δe_{max} between these limits) for an unspecified duration. After setting Δe_{max} at 0.4 and integrating the orbits for a duration of 515 asteroid rotations (90 days in Psyche's denormalized system), Figure 8.4 compares the original stability plots presented in Hu and Scheeres (2004) (left) and their reproduced counterparts (right).

Comparing the reproduced plots of the figure to the original plots, it is apparent that these match to a very high degree. Any observed discrepancy can be attributed to a difference in sampling (reproduced plots show a higher resolution), a difference in integration time and/or a difference in Δe_{max}. This result validates to a high degree the correct generation of the stability plots.

8.3. FLI-Stability Analysis

To the best of the author's knowledge, FLI or OFLI values in the uniformly rotating second degree and order gravity field have not been documented in literature to date. Therefore, a high-level one-to-one comparison of results to literature or another tool (which is able to compute FLI or OFLI values) is not possible. Nonetheless, several other methods of verification and validation can provide sufficient certainty that the FLI and OFLI values are computed in a correct way.

Firstly, the most complex and error-prone aspect of numerically integrating deviation vectors in the tangent subspace is the computation of the second-order derivatives of the potential. These second-order derivatives appear in the variational equations (see Equations 7.5 and 7.10). Using *Wolfram Mathematica*, Equation C.1 can be differentiated using its symbolic manipulation capabilities to obtain and compute the second-order derivatives of the potential for any given position in

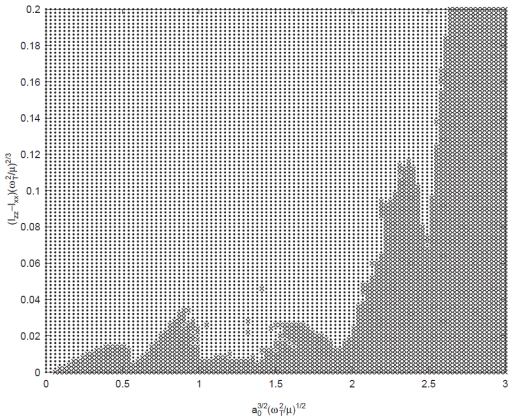

(a) Original plot with $\sigma = 1.0$.

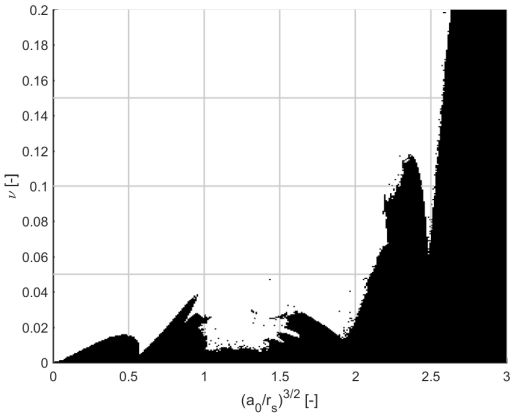

(b) Reproduced plot with $\sigma = 1.0$.

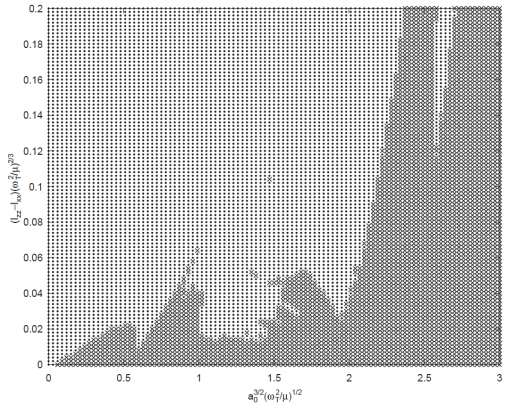

(c) Original plot with $\sigma = 0.5$.

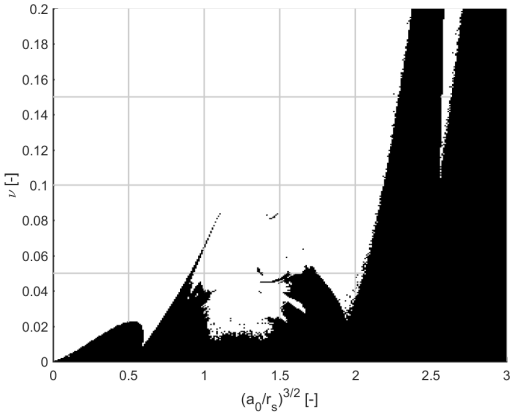

(d) Reproduced plot with $\sigma = 0.5$.

Figure 8.4: Comparison of original (left) (Hu and Scheeres, 2004) and reproduced (right) stability plots in the uniformly rotating second degree and order gravity field. Stable (dark) and unstable (light) regions can be observed. For the plots on the right, Δe_{max} is set at 0.4 and orbits are integrated for a duration of 515 central body rotations. Although different axis labels have been used in the figures on the right, they represent identical variables when compared to the axis labels on the left.

the phase space. Then, these values can be compared to the second-order derivatives computed before being entered into the variational equations as a way of verifying their computation. The comparison is presented in Table 8.2 for coordinates $x = 0.7$, $y = -1.6$ and $z = 1.1$ in the body-fixed frame of Psyche's nominal second degree and order gravity field.

Comparing the results presented in Table 8.2, it can be seen that the obtained values match to 16-digit accuracy. The observed discrepancies can be attributed to the precision of the double data type in C++ (approximately accurate to 16 digits). Multiple other coordinates (covering all eight quadrants) were checked as well and show the same level of accuracy. Therefore, it can be concluded that a major component of the computation of FLI and OFLI values is verified.

Secondly, the time histories of FLI and OFLI values presented in the previous chapter partly serve as validation as well. In particular, Figures 7.4 and 7.5 show the time history of the FLI, the deviation vectors and the radial distance of a regular and a chaotic orbit respectively. The oscillatory and linearly increasing behaviour of the deviation vectors of a regular orbit comply with results presented in literature, as does the exponentially increasing behaviour of the length of the devia-

Parameter	*Wolfram Mathematica*	C++	Δ
V_{xx}	0.9254092450199238	0.9254092450199238	$4.84\ 10^{-17}$
V_{xy}	-0.08605736768268550	-0.08605736768268547	$3.47\ 10^{-17}$
V_{xz}	0.06056849606088782	0.06056849606088782	$1.68\ 10^{-18}$
V_{yy}	1.089179569782646	1.089179569782646	$1.23\ 10^{-16}$
V_{yz}	-0.1422200057462166	-0.1422200057462166	$4.77\ 10^{-17}$
V_{zz}	-0.01458881480256971	-0.01458881480256974	$2.91\ 10^{-17}$

Table 8.2: Quantitative comparison of second order potential derivatives of a symbolic computation in *Wolfram Mathematica* and values computed in C++. The values are normalized and correspond to coordinates $x = 0.7$, $y = -1.6$ and $z = 1.1$ in the body-fixed frame of Psyche's nominal second degree and order gravity field. The fourth column contains the absolute difference between the results.

tion vectors for chaotic trajectories. The reader is referred to one of the initial papers on the FLI by Froeschlé et al. (1997a), which shows similar behaviour for a regular and a chaotic trajectory in the standard map (although a slightly different definition of the FLI is used). An additional validation can be provided by comparing the FLI and OFLI time history of a periodic orbit, which has not been shown so far. The OFLI is known to remain constant after a given period of time (Fouchard et al., 2002), whereas the value of the FLI will continue to increase indefinitely with time. The time history of the FLI and OFLI values of an equatorial circular orbit in a point-mass gravity field is presented in Figure 8.5. In the body-fixed frame, this orbit is clearly periodic.

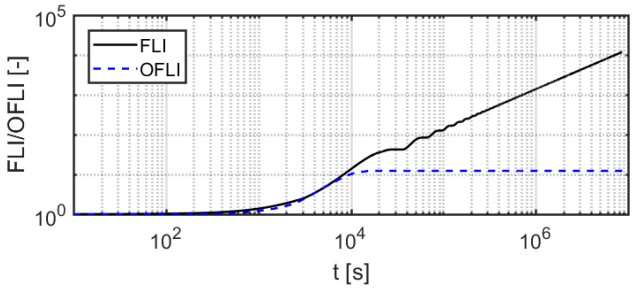

Figure 8.5: Time history of FLI and OFLI values of an equatorial circular orbit in a point-mass gravity field. The orbit is periodic in the body-fixed frame.

Again, it can be observed in this figure that the FLI and OFLI values behave as expected. The OFLI becomes constant after a given period of time, whereas the FLI continues to increase linearly with time.

Finally, refer back to Figure 7.12, which compared BIBO-stability plots to FLI maps. It clearly showed that the main characteristics of the BIBO-stability plots and the FLI maps comply, which is expected. In addition, the main discrepancies were successfully characterized and explained. Furthermore, it was shown that FLI or OFLI values can be used to flag instabilities sooner when compared to BIBO-stability constraints (see Figure 7.15).

It can be concluded that the results mentioned and illustrated in this section provide sufficient verification and validation for the computation of FLI and OFLI values and the generation of the FLI and OFLI maps for the uniformly rotating second degree and order gravity field.

This page is intentionally left blank.

9 Conclusions

The dynamically complex environment of minor celestial bodies such as the Psyche asteroid pose significant challenges for mission design. Throughout this work, the dynamics of the two-body problem with a uniformly rotating central body has been approached from an analytical perspective and with two conceptually different numerical methods. Significant contributions have been made to the study of orbit stability in this problem, and the methods presented throughout this work have been successfully applied to the Psyche mission.

Starting from the GPE, solutions for the semi-major axis and the eccentricity have been derived in the equatorial plane of the uniformly rotating second degree and order gravity field. The resulting expressions clearly show the detrimental impact of mean motion resonance with the asteroid rotation for prograde orbits. The 1:2, 1:1, 3:2 and 2:1 resonances were identified for prograde orbits. For retrograde orbits, the singularities in the solutions disappear, clearly indicating that retrograde orbits are robust against mean motion resonance instabilities. A comparison with numerical results showed that the expressions for the semi-major axis and eccentricity adequately describe the true solution for certain parameter ranges. Furthermore, the large parametric study of stability in this problem showed that the 1:2, 1:1, 3:2 and 2:1 resonances cause the strongest instabilities, which was expected.

The analytical approach mostly had a qualitative purpose to better understand the dynamics of the problem at hand. An extensive numerical characterization of stability in the uniformly rotating second degree and order gravity field proved to be of significant practical value. By sampling the initial condition space and the gravity field coefficients uniformly over a wide search range, stability plots were generated that can be applied to the majority of small bodies in the regions where gravity-field perturbations from the central body are dominant. These stability plots can be used as a preliminary mission design tool to quickly identify whether a circular orbit remains bounded for a duration up to 515 rotational periods of the central body (corresponds to 90 days in Psyche's denormalized system). In addition, these plots allowed for the development of a conservative empirical stability limit which provides a sufficient condition on stability. Comparing results for the second degree and order gravity field to the eighth degree and order gravity field showed that the lower degree and order field captures the global stability limits adequately to a level of accuracy which is suitable for preliminary mission design purposes. The major advantages of using a low degree and order gravity are the possibility of carrying out a large parametric search over the gravity field coefficients and a significant increase in computational efficiency. Furthermore, by applying the stability plots to a nominal and conservative Psyche gravity field, the current mission design was validated to a certain degree. Increasing the inclination of orbit C beyond 90 degrees might be necessary to

ensure stability in a conservative way. A non-zero eccentricity of 0.1 also allowed orbit D to reach altitudes closer to the surface of Psyche, even with an inclination smaller than the currently proposed 160 degrees. This will allow for a greater science output for the mission due to increased coverage of the asteroid surface.

It has been shown that variational chaos indicators such as the FLI or OFLI provide a valuable complementary mission design tool. FLI maps can be used to identify families of periodic orbits. In addition, it is clear that FLIs and OFLIs distinguish between stable and unstable motion much more effectively when compared to BIBO-stability constraints. For certain initial conditions, these chaos indicators detect instability much sooner when compared to BIBO-stability constraints. The only disadvantages are an increased computational effort (dependent on the number of initial deviation vectors) and occasionally flagging escape trajectories as regular. However, the latter can be mitigated by combining a BIBO-stability constraint with a stability constraint based on the final value of the FLI or OFLI. Their use has also been demonstrated to the Psyche mission design.

10 Recommendations

With the research presented in this thesis, a considerable contribution has been made to the small-body problem and the Psyche mission. Several recommendations can be made in order to extend this work and to apply it to the preliminary design of small-body missions.

The analytical expressions presented in this work were derived starting from the GPE using Keplerian elements. Consequently, singularities for the eccentricity approaching zero occur for the longitude of periapsis and the true anomaly. To mitigate this unfavorable characteristic of the derived expressions, it is recommended to derive the same expressions using equinoctial elements instead. Possibly, this will result in similar solutions without a singularity appearing for quasi-circular equatorial orbits. In addition, by including higher-order terms in the eccentricity throughout the derivations and/or by including additional spherical harmonic coefficients, it is expected that the analytical solutions will contain terms that account for additional resonances as well. However, these additional terms are expected to be weaker.

Additionally, it can be recommended to analyze the problems tackled in this research from a dynamical systems perspective as well. This can be done by extending the phase space characterization to include the following analyses: determine the locations and assess the stability of the equilibria in Psyche's eighth degree and order gravity field, apply Poincaré maps to better understand the dynamics of the problem, identify and determine the stability of families of 3D periodic solutions and search for manifold transfers within the system in order to identify low-cost transfer trajectories. It is also noted that the Jacobi constant plays an important role in conditions for impact and escape. Therefore, an additional numerical analysis concerning the impact of the Jacobi constant and zero-velocity surfaces can be valuable as well.

The parametric stability analyses presented throughout this work are limited by the available computational resources. Increasing the sampling resolution will make the results presented here even more valuable. Furthermore, it would be interesting to investigate the influence of individual third or fourth degree and order spherical harmonic coefficients on stability. Again, this comes at an increased computational cost.

Furthermore, the empirical stability limit can be complemented by an empirical instability limit, which separates the completely unstable region. In this way, three regions can be identified: a stable region, an unstable region and an intermediate region for which it is required to conduct additional stability analyses.

Finally, it can be recommended to develop this initial work into a complementary small-body mission design tool. The BIBO-stability plots complemented by the FLI maps have shown to be of significant practical value for the Psyche mission. It is expected that these tools can be valuable for other future small-body missions as well.

A

Reference Frames and Coordinate Transformations

This appendix contains a brief description of the reference frames used throughout the orbit propagations. Firstly, Section A.1 describes two reference frames and the conversion of Cartesian coordinates between these two frames. Then, Section A.2 presents the equations to convert Cartesian coordinates to Keplerian elements. Finally, Section A.3 presents the equations to convert from Keplerian elements to Cartesian coordinates.

Due to singularities appearing for equatorial and/or circular orbits in several of the Keplerian elements, it is required to use different sets of Keplerian elements for those cases than the one presented here. The conversions between Cartesian coordinates and these different sets of Keplerian elements is not presented here and the reader is referred to Vallado (2007).

A.1. Rotating and Inertial Reference Frame Transformations

In total, two reference frames are required to carry out the orbit propagations. A uniformly rotating body-fixed reference frame is needed since the equations of motion are described therein and an inertial reference frame is needed to describe the orbits in terms of their Keplerian elements. Both reference frames are centered at the CoM of the asteroid and have their z-axes aligned. The graphical relation between the two frames is illustrated in Figure A.1.

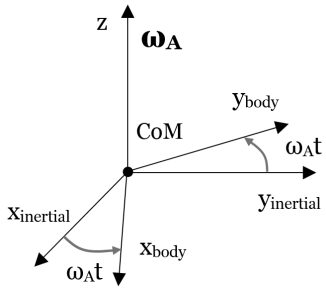

Figure A.1: Inertial and uniformly rotating body-fixed reference frames used throughout simulations.

Frame transformations are only required around the z-axis and are purely rotational. Equation A.1 shows the rotation matrix around the z-axis.

$$R_3(\omega_A t) = \begin{bmatrix} \cos\omega_A t & -\sin\omega_A t & 0 \\ \sin\omega_A t & \cos\omega_A t & 0 \\ 0 & 0 & 1 \end{bmatrix} \tag{A.1}$$

To transform Cartesian position and velocity coordinates from the rotating frame to the inertial frame and vice versa, use can be made of Equations A.2 and A.3 respectively (Niedling et al., 2016).

$$\boldsymbol{r}_{inertial} = R_3(\omega_A t)\boldsymbol{r}_{body} \tag{A.2}$$

$$\boldsymbol{v}_{inertial} = R_3(\omega_A t)(\boldsymbol{v}_{body} + \boldsymbol{\omega_A} \times \boldsymbol{r}_{body}) \tag{A.3}$$

Finally, Keplerian elements are more intuitive to analyze compared to Cartesian coordinates. The equations to convert from Cartesian coordinates to Keplerian elements and vice versa are presented in the following two sections.

A.2. Cartesian Coordinates to Keplerian Elements

This section presents the equations to convert from Cartesian coordinates to Keplerian elements in the inertial frame. All equations in this section and the next are obtained from Wertz (2002).

First, the radial position and velocity can be determined with Equations A.4 and A.5 respectively.

$$r = \sqrt{x^2 + y^2 + z^2} \tag{A.4}$$

$$v = \sqrt{v_x^2 + v_y^2 + v_z^2} \tag{A.5}$$

Then, the semi-major axis can be obtained with the vis-viva equation shown in Equation A.6.

$$a = 1/(\frac{2}{r} - \frac{v^2}{\mu}) \tag{A.6}$$

The vector describing the specific angular momentum of the spacecraft and the vector $\boldsymbol{N}$ are given in Equations A.7 and A.8 respectively.

$$\boldsymbol{h} = \boldsymbol{r} \times \boldsymbol{v} \tag{A.7}$$

$$\boldsymbol{N} = \begin{bmatrix} 0 \\ 0 \\ 1 \end{bmatrix} \times \boldsymbol{h} \tag{A.8}$$

The eccentricity vector is given in Equation A.9 and the inclination is given in Equation A.10. The eccentricity itself is simply the magnitude of the eccentricity vector.

$$\boldsymbol{e} = \frac{\boldsymbol{v} \times \boldsymbol{h}}{\mu} - \frac{\boldsymbol{r}}{r} \tag{A.9}$$

$$i = \arccos\left(\frac{h_z}{|\boldsymbol{h}|}\right) \tag{A.10}$$

Next, the right ascension of the ascending node can be calculated with Equation A.11.

$$\Omega = atan2\left(h_x, -h_y\right) \tag{A.11}$$

Finally, the argument of periapsis and the true anomaly can be calculated with Equations A.12 and A.13 respectively. Note that $sign$ takes the sign of the expression it contains.

$$\omega = sign((\boldsymbol{N} \times \boldsymbol{e}) \cdot \boldsymbol{h}) \cdot \arccos(\hat{\boldsymbol{e}} \cdot \hat{\boldsymbol{N}}) \tag{A.12}$$

$$\theta = sign((\boldsymbol{e} \times \boldsymbol{r}) \cdot \boldsymbol{h}) \cdot \arccos(\hat{\boldsymbol{r}} \cdot \hat{\boldsymbol{e}}) \tag{A.13}$$

Six Keplerian elements have been determined. Other definitions for the sixth parameter exist as well (i.e. the mean anomaly, the eccentric anomaly and the time of periapsis passage) but are not relevant for the current analysis.

A.3. Keplerian Elements to Cartesian Coordinates

Now, the equations to convert Keplerian elements to Cartesian coordinates in the inertial frame will be presented. First, the radial distance and the angular momentum can be determined from Equations A.14 and A.15 respectively.

$$r = \frac{a(1-e^2)}{1+e\cos\theta} \tag{A.14}$$

$$h = \sqrt{\mu a(1-e^2)} \tag{A.15}$$

A set of six intermediate parameters is introduced in Equations A.16 through A.21.

$$l_1 = \cos\Omega\cos\omega - \sin\Omega\sin\omega\cos i \tag{A.16}$$

$$l_2 = -\cos\Omega\sin\omega - \sin\Omega\cos\omega\cos i \tag{A.17}$$

$$m_1 = \sin\Omega\cos\omega + \cos\Omega\sin\omega\cos i \tag{A.18}$$

$$m_2 = -\sin\Omega\sin\omega + \cos\Omega\cos\omega\cos i \tag{A.19}$$

$$n_1 = \sin\omega\sin i \tag{A.20}$$

$$n_2 = \cos\omega\sin i \tag{A.21}$$

Finally, the Cartesian position and velocity coordinates can be determined from Equations A.22 through A.24 and Equations A.25 through A.27 respectively.

$$x = l_1 r\cos\theta + l_2 r\sin\theta \tag{A.22}$$

$$y = m_1 r\cos\theta + m_2 r\sin\theta \tag{A.23}$$

$$z = n_1 r\cos\theta + n_2 r\sin\theta \tag{A.24}$$

$$v_x = \frac{\mu}{h}\big[-l_1\sin\theta + l_2(e+\cos\theta)\big] \tag{A.25}$$

$$v_y = \frac{\mu}{h}\big[-m_1\sin\theta + m_2(e+\cos\theta)\big] \tag{A.26}$$

$$v_z = \frac{\mu}{h}\big[-n_1\sin\theta + n_2(e+\cos\theta)\big] \tag{A.27}$$

B

Phase Space Characterization

Since the system under consideration is non-dissipative, the notion of asymptotic stability is not applicable. In general, stable orbits are defined as orbits which are bounded to a certain region in the space around the body. Scheeres (1994) found that for a second degree and order gravity field, the body has four equilibrium points. Two of these points are always unstable and the other two can either be stable or unstable, which differentiates between Type I and Type II asteroids respectively. If Psyche were a Type I asteroid, the two stable equilibrium points can be scientifically and practically interesting as orbits close to these points would not drift away. However, the actual gravity field might result in the need for active station-keeping and orbit maintenance. Unstable equilibria can be used for energy-efficient manifold transfers.

Strongly tied with the analysis of equilibria around small bodies is the study of periodic orbits. These are orbits which close in upon itself in the body-fixed frame after a certain period of time and repeat this motion indefinitely. Similar to stable equilibria, stable periodic orbits can be scientifically interesting since the phase space around these orbits can exhibit stable behaviour as well (Scheeres, 2012, p. 121). However, the search for and analysis of such periodic solutions is out of scope of this research.

This appendix will briefly characterize the phase space of Psyche's nominal second degree and order gravity field. Firstly, Section B.1 describes the zero-velocity surfaces. After that, the equilibria are identified and their stability is analyzed in Section B.2. Finally, stable trajectories in the vicinity of the equilibria are presented in Section B.3.

B.1. Zero-Velocity Surfaces

In Section 3.3 it was shown that the Hamiltonian of the equations of motion within the uniformly rotating system is conserved. This integral of motion was defined as the Jacobi energy or Jacobi constant. From its definition, it is clear that a set of initial conditions within the phase space can have the same Jacobi constant C_J. Since the Jacobi constant does not vary for a given particle moving within the system, the motion of this particle is limited to certain regions within the phase space. For a given Jacobi constant, the phase space can be divided in an accessible region $V(\boldsymbol{r}) \geq C_J$ and a forbidden region $V(\boldsymbol{r}) < C_J$. The boundary of these regions is given by $V(\boldsymbol{r}) = C_J$ and is a so-called zero-velocity surface.

For $C_J > 0$, a trajectory can potentially collide with these surfaces and bounce off them, never crossing the surface. On the other hand if $C_J < 0$, the phase space of the system is completely accessible by the spacecraft. For Psyche and its nominal second degree and order gravity field, these

zero-velocity surfaces for different Jacobi constants are illustrated in Figure B.1 for the xy-plane. In addition to the two-dimensional surface plot, zero-velocity surfaces for different Jacobi constants can be plotted in the full three-dimensional phase space in Figure B.2 for Psyche's nominal gravity field.

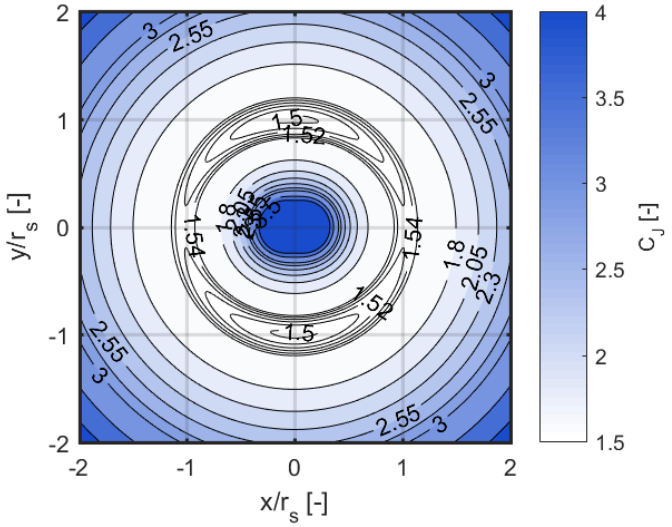

Figure B.1: Zero-velocity surfaces in Psyche's equatorial plane assuming a uniformly rotating second degree and order gravity field. All variables in this figure are normalized according to Equations 3.19 and 3.20.

The geometry of these surfaces have important implications for stability and the accessibility of spacecraft trajectories with respect to the central body. Firstly, four equilibria can be identified in Figure B.1: two saddle points along the x-axis and two equilibria along the y-axis, which complies with the results obtained by Scheeres (1994). Secondly, the volume of the forbidden regions in the phase space decreases as the Jacobi constant decreases. For $C_J > 1.54$, two surfaces encompass the body as shown in Figure B.2. One of the surfaces forms a quasi-cylindrical shape and the other wraps closely around the body. Orbits initialized with $C_J > 1.54$ outside of the quasi-cylinder will never impact the body, whereas if they are initialized inside the inner surface, they will most likely impact the body. As the Jacobi constant decreases from 1.54 to 1.52, the two surfaces intersect and form a single surface, making the body accessible by all trajectories. This intersection occurs at $J_C = 1.53109$ and will be referred to as the Jacobi constant of intersection J_{C_X}. For $1.50 < C_J < 1.48$, the zero-velocity surface splits into two branches again, making the phase space even more accessible as the Jacobi constant decreases. The Jacobi constant of intersection J_{C_X} is important since any trajectory with $J_C > J_{C_X}$ will either be trapped and impact the body or will never be able to impact the body, depending on whether the trajectory is initialized within or outside of the zero-velocity surface.

B.2. Equilibria and Stability

According to Scheeres (1994), a symmetric body with a second degree and order gravity has four equilibria placed in symmetry across its principal x- and y-axes. The locations of the four equilibria are given in Equations B.1 and B.2.

$$E_{\pm x} = (\pm x_{eq}, 0, 0) \tag{B.1}$$

$$E_{\pm y} = (0, \pm y_{eq}, 0) \tag{B.2}$$

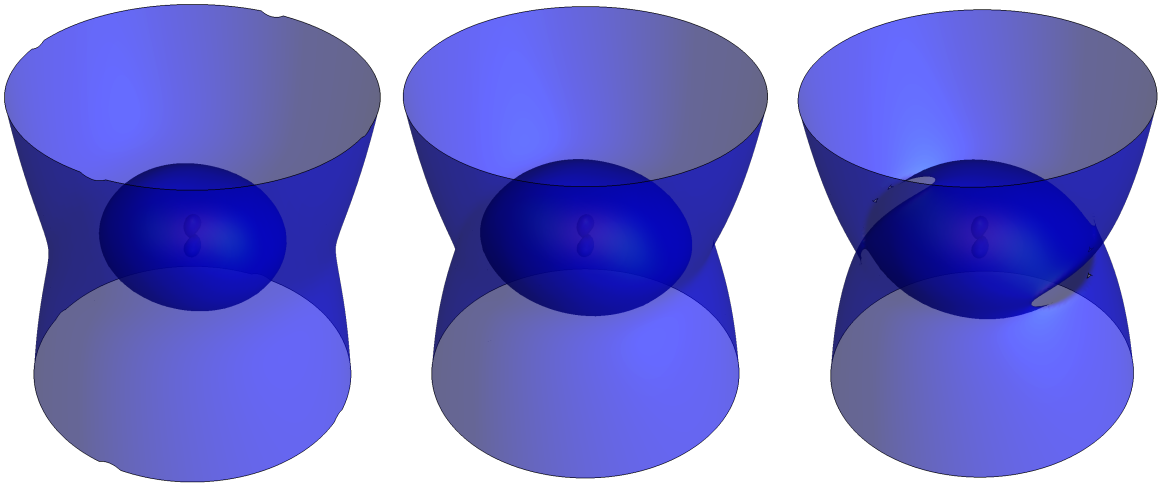

(a) $C_J = 1.60$ (b) $C_J = 1.54$ (c) $C_J = 1.52$

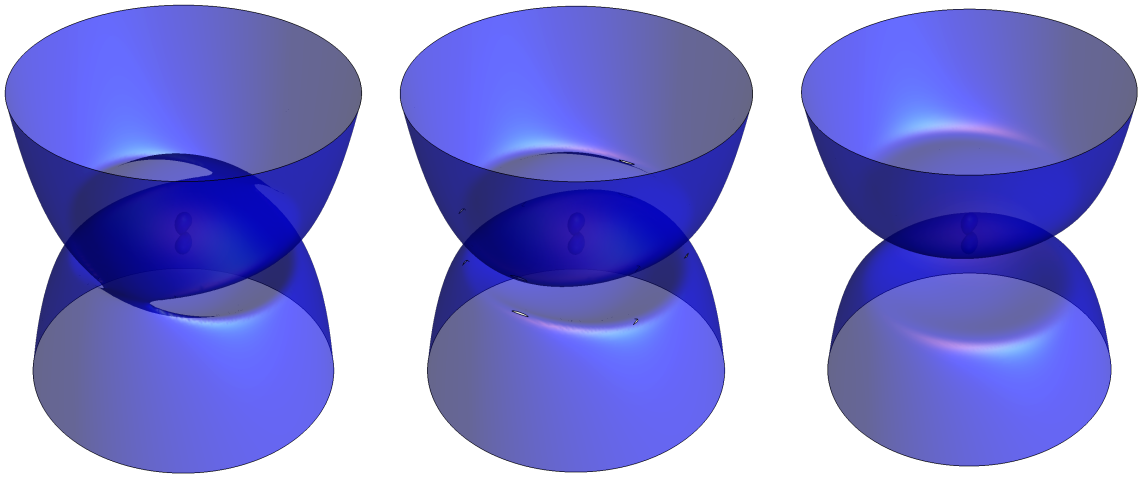

(d) $C_J = 1.50$ (e) $C_J = 1.48$ (f) $C_J = 1.40$

Figure B.2: Zero-velocity surfaces around Psyche's nominal uniformly rotating second degree and order gravity field. The normalized Jacobi constant decreases from left to right, which decreases the volume of the forbidden regions.

Coefficients C_{20} and C_{22} normalized with respect to r_s are given in Table 3.1. For C_{20}, $C_{22} \ll 1$, x_{eq} and y_{eq} can be determined to first-order accuracy with Equations B.3 and B.4 respectively (Hu and Scheeres, 2004). Their values for the nominal and conservative gravity fields are listed in Table B.1.

$$x_{eq} = 1 - \frac{1}{2}C_{20} + 3C_{22} \tag{B.3}$$

$$y_{eq} = 1 - \frac{1}{2}C_{20} - 3C_{22} \tag{B.4}$$

As mentioned before, Scheeres (1994) showed that equilibria $E_{\pm x}$ are always unstable. More interestingly is the stability of points $E_{\pm y}$, especially since unstable equilibria $E_{\pm y}$ result in unstable motion close to the 1:1 resonance radius of the body, which is a boundary that has to be crossed for the Psyche mission in order to transfer from orbit C to D. By linearizing Equations 3.48 and 3.49 about equilibrium points $(0, \pm y_{eq})$, the characteristic equation can be found which is given in Equation B.5 (Hu and Scheeres, 2004).

Equilibrium Location	Nominal	Conservative
x_{eq}	1.0325	1.0527
y_{eq}	0.9983	0.9941

Table B.1: Equilibria locations in the phase space of Psyche for its nominal and conservative second degree and order gravity fields. The values are normalized with respect to the resonance radius of the body.

$$\lambda^4 + \frac{y_{eq}^2 + \frac{3}{2}C_{20} - 3C_{22}}{y_{eq}^2 - \frac{3}{2}C_{20} - 9C_{22}}\lambda^2 + \frac{36C_{22}(y_{eq}^2 - \frac{5}{2}C_{20} - 15C_{22})}{(y_{eq}^2 - \frac{3}{2}C_{20} - 9C_{22})^2} = 0 \tag{B.5}$$

Again, assuming C_{20}, $C_{22} \ll 1$, it can be shown that Equation B.6 (Hu and Scheeres, 2004) must hold for the equilibria to be stable.

$$-C_{20} + 162C_{22} < 1 \tag{B.6}$$

The inequality above can be evaluated for Psyche's nominal and conservative gravity fields. The results are presented in Table B.2.

Stability Condition	Nominal	Conservative
$-C_{20}$+$162C_{22}$	0.9555	1.6276

Table B.2: Evaluation of stability condition presented in Equation B.6 for Psyche's nominal and conservative gravity fields.

Interestingly, the nominal second degree and order gravity field contains two marginally stable equilibria $E_{\pm y}$, whereas all equilibria are unstable considering the conservative gravity field. Therefore, it can be concluded that it is impossible to confirm whether Psyche is a Type I or Type II asteroid. In case Psyche's real gravity field closely resembles the assumed nominal field, stable trajectories could be found near its equilibria. This scenario is considered in the following section.

B.3. Stable Trajectories around Equilibria

Since equilibria $E_{\pm y}$ are stable in Psyche's nominal second degree and order gravity field, spacecraft orbits around these equilibria can be of benefit to the mission for station keeping or low-altitude scientific exploration of a certain area of the surface of the asteroid over an extended period of time. To verify the results obtained above, a trajectory in proximity of equilibrium $(0, y_{eq}, 0)$ is shown in Figures B.3a and B.3c for Psyche's nominal second degree and order field with initial position (5 km, y_{eq}-2 km, 28 km) and zero relative velocity in the body-fixed frame. To confirm the validity of the second degree and order gravity field analysis, the same initial condition is used to generate a trajectory in the eighth degree and order gravity field, which is shown in Figures B.3b and B.3d.

The trajectory shown in Figures B.3a and B.3c confirms that the equilibria $E_{\pm y}$ in the nominal second degree and order gravity field are stable. In addition, a similar pattern is observed when generating a trajectory in the eighth degree and order gravity field, while it is clear that the locations of the equilibria are different. Nonetheless, the trajectory in the higher degree and order field remains bound as well for at least 1000 days, suggesting that the equilibria remain stable as more gravity field coefficients are added to the force model. This example illustrates the impact of the second degree and order gravity coefficients on stability and the validity of using a low degree and order gravity field model for analyzing stability.

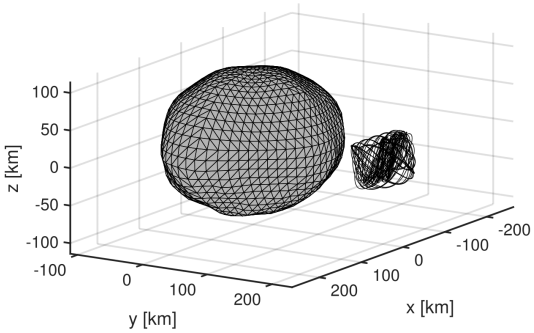

(a) 3D trajectory in second degree and order gravity field.

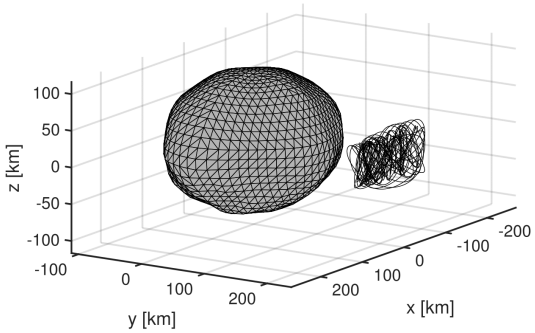

(b) 3D trajectory in eighth degree and order gravity field.

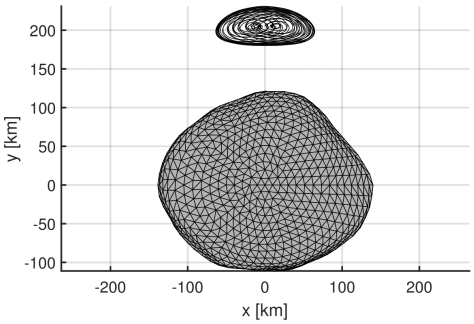

(c) xy-view of trajectory in second degree and order gravity field.

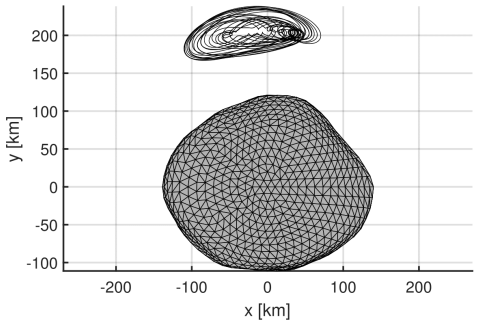

(d) xy-view of trajectory in eighth degree and order gravity field.

Figure B.3: Spacecraft trajectories near stable equilibrium on $+y$ side of Psyche, propagated for 10 days and shown within the body-fixed frame. It was verified that the trajectories remain bound within the same region for at least 1000 days and do not diverge from the equilibrium. Trajectories were generated for both the second and eighth degree and order gravity field.

This page is intentionally left blank.

C

Second Degree and Order Gravity Field Derivatives

This appendix contains expressions for the first- and second-order derivatives of the uniformly rotating second degree and order gravity field. All expressions in this appendix are normalized with respect to the 1:1 resonance radius of the uniformly rotating body.

Firstly, the effective potential in the uniformly rotating frame is given by Equation C.1 (Hu and Scheeres, 2008).

$$V = \frac{1}{2}(x^2+y^2) + \frac{1}{r} - \frac{C_{20}(x^2+y^2-2z^2)}{2r^5} + \frac{3C_{22}(x^2-y^2)}{r^5} \tag{C.1}$$

The first-order derivatives of the potential with respect to coordinates x, y and z are given in Equations C.2, C.3 and C.4 respectively.

$$V_x = x\Big[1 - \frac{15C_{22}(x^2-y^2)}{r^7} + \frac{5C_{20}(x^2+y^2-2z^2)}{2r^7} - \frac{C_{20}}{r^5} + \frac{6C_{22}}{r^5} - \frac{1}{r^3}\Big] \tag{C.2}$$

$$V_y = y\Big[1 - \frac{15C_{22}(x^2-y^2)}{r^7} + \frac{5C_{20}(x^2+y^2-2z^2)}{2r^7} - \frac{C_{20}}{r^5} - \frac{6C_{22}}{r^5} - \frac{1}{r^3}\Big] \tag{C.3}$$

$$V_z = z\Big[-\frac{15C_{22}(x^2-y^2)}{r^7} + \frac{5C_{20}(x^2+y^2-2z^2)}{2r^7} + \frac{2C_{20}}{r^5} - \frac{1}{r^3}\Big] \tag{C.4}$$

The second-order derivatives of the potential with respect to coordinates x and x, y and y, z and z, x and y, x and z and y and z are given in Equations C.5, C.6, C.7, C.8, C.9 and C.10 respectively. Note that $V_{yx} = V_{xy}$, $V_{yz} = V_{zy}$ and $V_{zx} = V_{xz}$.

$$\begin{aligned} V_{xx} =& 1 + x^2\Big[\frac{105C_{22}(x^2-y^2)}{r^9} - \frac{35C_{20}(x^2+y^2-2z^2)}{2r^9} + \frac{10C_{20}}{r^7} - \frac{60C_{22}}{r^7} + \frac{3}{r^5}\Big] + \\ & \frac{5C_{20}(x^2+y^2-2z^2)}{2r^7} - \frac{15C_{22}(x^2-y^2)}{r^7} - \frac{C_{20}}{r^5} + \frac{6C_{22}}{r^5} - \frac{1}{r^3} \end{aligned} \tag{C.5}$$

$$V_{yy} = 1 + y^2\left[\frac{105C_{22}(x^2-y^2)}{r^9} - \frac{35C_{20}(x^2+y^2-2z^2)}{2r^9} + \frac{10C_{20}}{r^7} + \frac{60C_{22}}{r^7} + \frac{3}{r^5}\right] + \frac{5C_{20}(x^2+y^2-2z^2)}{2r^7} - \frac{15C_{22}(x^2-y^2)}{r^7} - \frac{C_{20}}{r^5} - \frac{6C_{22}}{r^5} - \frac{1}{r^3} \tag{C.6}$$

$$V_{zz} = z^2\left[\frac{105C_{22}(x^2-y^2)}{r^9} - \frac{35C_{20}(x^2+y^2-2z^2)}{2r^9} - \frac{20C_{20}}{r^7} + \frac{3}{r^5}\right] + \frac{5C_{20}(x^2+y^2-2z^2)}{2r^7} - \frac{15C_{22}(x^2-y^2)}{r^7} + \frac{2C_{20}}{r^5} - \frac{1}{r^3} \tag{C.7}$$

$$V_{xy} = xy\left[\frac{105C_{22}(x^2-y^2)}{r^9} - \frac{35C_{20}(x^2+y^2-2z^2)}{2r^9} + \frac{10C_{20}}{r^7} + \frac{3}{r^5}\right] \tag{C.8}$$

$$V_{xz} = xz\left[\frac{105C_{22}(x^2-y^2)}{r^9} - \frac{35C_{20}(x^2+y^2-2z^2)}{2r^9} - \frac{5C_{20}}{r^7} - \frac{30C_{22}}{r^7} + \frac{3}{r^5}\right] \tag{C.9}$$

$$V_{yz} = yz\left[\frac{105C_{22}(x^2-y^2)}{r^9} - \frac{35C_{20}(x^2+y^2-2z^2)}{2r^9} - \frac{5C_{20}}{r^7} + \frac{30C_{22}}{r^7} + \frac{3}{r^5}\right] \tag{C.10}$$

D

Software Flow Diagrams

This appendix contains the software flow diagrams of a single sampled orbit in stability analyses *B* and *C* in Figures D.1 and D.2 respectively.

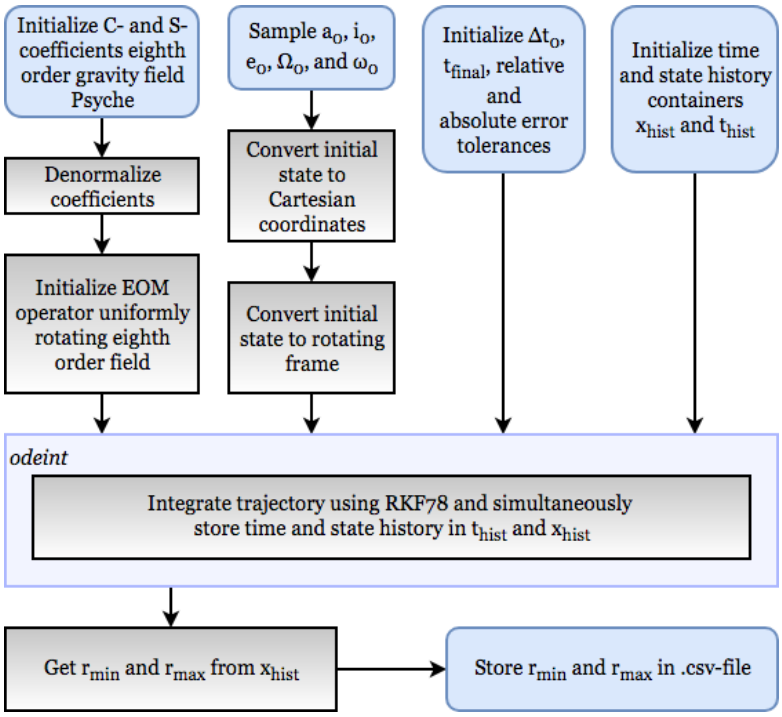

Figure D.1: Flow diagram of sampled orbit in BIBO-stability analysis *B*.

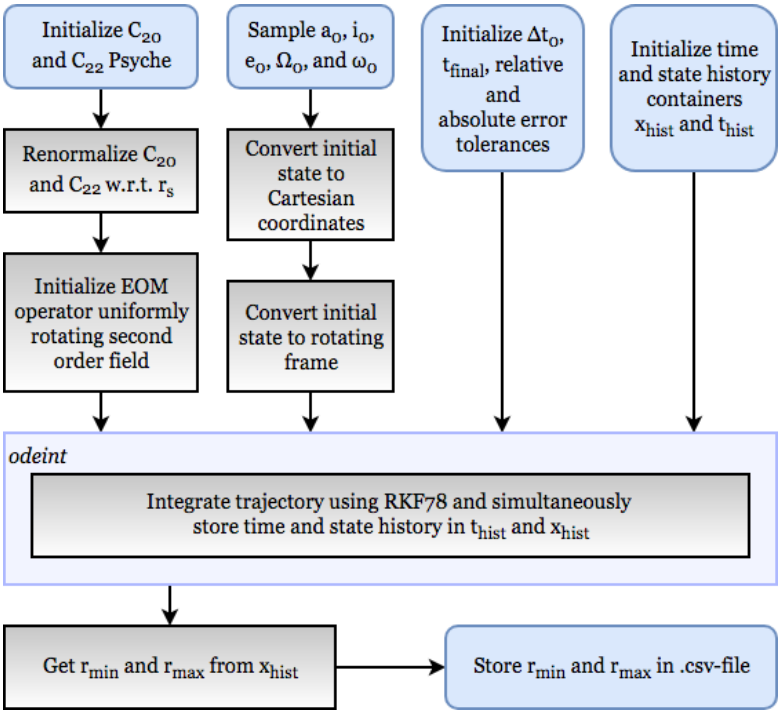

Figure D.2: Flow diagram of sampled orbit in BIBO-stability analysis *C*.

Bibliography

K. Ahnert and M. Mulansky. Odeint - Solving Ordinary Differential Equations in C++. In *AIP Conference Proceedings*, volume 1389, pages 1586–1589, Orlando, Florida, USA, 2011. American Institute of Physics.

R. A. N. Araujo, O. C. Winter, and A. F. B. A. Prado. Stable retrograde orbits around the triple system 2001 SN263. *Monthly Notices of the Royal Astronomical Society*, 449:4404–4414, 2015.

J. Baer and S. R. Chelsey. Simultaneous Mass Determination for Gravitationally Coupled Asteroids. *The Astronomical Journal*, 154(76):1–11, August 2017.

J. Baer, S. R. Chelsey, and R. D. Matson. Astrometric Masses of 26 Asteroids and Observations of Asteroid Porosity. *The Astronomical Journal*, 141(143):1–12, May 2011.

G. Benettin, L. Galgani, A. Giorgilli, and J. M. Strelcyn. Lyapunov Characteristic Exponents for Smooth Dynamical Systems and for Hamiltonian Systems; a Method for Computing all of them. Part 1 2. *Meccanica*, 15(1):9–31, 1980.

S. B. Broschart, M. Abrahamson, S. Bhaskaran, et al. The Small-Body Dynamics Toolkit and Associated Close-Proximity Navigaton Analysis Tools at JPL. In *AAS Guidance and Control Conference*, pages 1–12, Breckenridge, Colorado, USA, February 2015. American Astronautical Society.

P. M. Cincotta and C. Simó. Simple tools to study global dynamics in non-axisymmetric galactic potentials. *Astronomy and Astrophysics Supplement Series*, 147:205–228, 2000.

L. A. Darriba, N. P. Maffione, P. M. Cincotta, and C. M. Giordano. Comparative study of variational chaos indicators and ODEs' numerical integrators. *International Journal of Bifurcation and Chaos*, 22:105–112, 2012.

F. E. DeMeo, C. M. O'D. Alexander, K. J. Walsh, C. R. Chapman, and R. P. Binzel. *Asteroids IV*, chapter The Compositional Structure of the Asteroid Belt, pages 13–41. Space Science Series. University of Arizona Press, 2015.

M. Fouchard, E. Lega, Ch. Froeschlé, and Cl. Froeschlé. On the relationship between fast Lyapunov indicator and periodic orbits for continuous flows. *Celestial Mechanics and Dynamical Astronomy*, 83:205–222, 2002.

Cl. Froeschlé, R. Gonczi, and E. Lega. The fast Lyapunov indicator: a simple tool to detect weak chaos. Application to the structure of the main asteroid belt. *Planetary and Space Science*, 45(7): 881–886, 1997a.

Cl. Froeschlé, E. Lega, and R. Gonczi. Fast Lyapunov Indicators. Application to Astroidal Motion. *Celestial Mechanics and Dynamical Astronomy*, 67:41–62, 1997b.

E. Hairer, C. Lubich, and G. Wanner. *Geometrical Numerical Integration, Structure-Preserving Algorithms for Ordinary Differential Equations*. Springer Series in Computational Mathematics. Springer, second edition, 2006.

J. Hanuš et al. Volumes and bulk densities of forty asteroids from ADAM shape modeling. *Astronomy and Astrophysics*, 601(114):1–41, May 2017.

I. Haranas and O. Ragos. Gauss Planetary Equations in a Non-Singular Potential. In *Proceedings of the NPA*, volume 6, Long Beach, USA, 2010. Natural Philosophy Alliance.

B. Hofmann-Wellenhof and H. Moritz. *Physical Geodesy*. Springer-Verlag Wien, second edition, 2006.

M. J. Holman and P. A. Wiegert. Long-Term Stability of Planets in Binary Systems. *The Astronomical Journal*, 117:621–628, 1999.

W. Hu and D. J. Scheeres. Numerical determination of stability regions for orbital motion in uniformly rotating second degree and order gravity fields. *Planetary and Space Science*, 52:685–692, 2004.

W. Hu and D. J. Scheeres. Periodic Orbits in Rotating Second Degree and Order Gravity Fields. *Chinese Journal of Astronomy and Astrophysics*, 6(1):108–118, 2008.

M. Hénon and C. Heiles. The applicability of the Third Integral of Motion: Some Numerical Experiments. *The Astronomical Journal*, 69(1), 1964.

JPL. 16 Psyche JPL Small-Body Database Browser. `https://ssd.jpl.nasa.gov/sbdb.cgi?sstr=16`, 2018. Accessed: 13-02-2018.

M. Kaasalainen, J. Torppa, and J. Piironen. Models of Twenty Asteroids from Photometric Data. *Icarus*, 159(2):369–395, May 2002.

A. M. Lyapunov. *The general problem of the stability of motion*. PhD thesis, University of Kharkov, Kharkov Mathematical Society, Kharkov, Russia, 1892. Text was first translated from Russian to French by E. Davaux (A. M. Liapounoff. Problème général de la stabilité du mouvement. *Annales de la Faculté des Sciences de Toulouse* 9:203–474,1907), after which it was translated to English by A. T. Fuller (A. M. Lyapunov: The general problem of stability of motion. *International Journal of Control*, 55:531–773, 1992).

N. P. Maffione, L. A. Darriba, P. M. Cincotta, and C. M. Giordano. A comparison of different indicators of chaos based on the deviation vectors: application to symplectic mappings. *Celestial Mechanics and Dynamical Astronomy*, 111:285–307, 2011.

O. Montenbruck and E. Gill. *Satellite Orbits: Models, Methods and Applications*. Springer, 2000.

J. Niedling, D. Gaylor, M. Hallmann, and R. Foerstner. Development of a Tool for Analyzing Orbits around Asteroids. In *Spaceflight Mechanics 2016*, volume 158, pages 1–19, Napa, USA, 2016. Univelt Inc.

D. Y. Oh, S. Collins, D. Goebel, B. Hart, G. Lantoine, S. Snyder, G. Whiffen, L. Elkins-Tanton, P. Lord, Z. Pirkl, and L. Rotlisburger. Development of the Psyche Mission for NASA's Discovery Program. In *35th International Electric Propulsion Conference*, Georgia Institute of Technology, Atlanta, USA, 2017.

D. Y. Oh et al. Psyche: Journey to a Metal World. In *52nd AIAA/SAE/ASEE Joint Propulsion Conference*, pages 1–12, Salt Lake City, UT, USA, July 2016. American Institute of Aeronautics and Astronautics.

V. I. Oseledec. A multiplicative ergodic theorem. Ljapunov characteristic numbers for dynamical systems. *Transactions of the Moscow Mathematical Society*, 19:197–231, 1968.

J. R. Rice. Experiments on Gram-Schmidt Orthogonalization. *Mathematics of Computation*, 20(94): 325–328, April 1966.

R. P. Russell. Global Search for Planar and Three-Dimensional Periodic Orbits near Europa. *The Journal of the Astronautical Sciences*, 54(2):199–226, 2006.

J. A. Sanchez, V. Reddy, M. K. Shepard, C. Thomas, E. A. Cloutis, D. Takir, A. Conrad, C. Kiddel, and D. Applin. Detection of Rotational Spectral Variation on the M-type Asteroid (16) Psyche. *The Astronomical Journal*, 153(29):1–8, January 2017.

D. J. Scheeres. Satellite Dynamics About Asteroids. In *AAS/AIAA Space Flight Mechanics Meeting*, pages 94–112, Cocoa Beach, Florida, USA, February 1994. American Astronautical Society.

D. J. Scheeres. *Hamiltonian Systems with Three or More Degrees of Freedom*, volume 533 of *NATO ASI Series (Series C:Mathematical and Physical Sciences)*, chapter Satellite Dynamics About Asteroids: Computing Poincaré Maps for the General Case, pages 554–558. Springer, Dordrecht, 1999a.

D. J. Scheeres. The Effect of C22 on Orbit Energy and Angular Momentum. *Celestial Mechanics and Dynamical Astronomy*, 73(339), 1999b.

D. J. Scheeres. *Orbital Motion in Strongly Perturbed Environments: Applications to Asteroid, Comet and Planetary Satellite Orbiters*. Astronautical Engineering. Springer-Verlag Berlin Heidelberg, Praxis Publishing, 2012.

D. J. Scheeres, S. J. Ostro, R. S. Hudson, and R. A. Werner. Orbits Close to Asteroid 4769 Castalia. *Icarus*, 121(72):67–87, 1996.

M. K. Shepard et al. Radar observations and shape model of asteroid 16 Psyche. *Icarus*, 281:388–403, 2016.

Ch. Skokos. Alignment indices: a new, simple method for determining the ordered or chaotic nature of orbits. *Journal of Physics A: Mathematical and General*, 34:10029–10043, 2001.

Ch. Skokos. Geometrical properties of local dynamics in Hamiltonian systems: the Generalized Alignment Index (GALI) method. *Physica D*, 231:30–54, 2007.

Ch. Skokos. *Dynamics of Small Solar System Bodies and Exoplanets*, volume 790 of *Lecture Notes in Physics*, chapter The Lyapunov Characteristic Exponents and Their Computation, pages 62–135. Springer-Verlag Berlin Heidelberg, 2010.

Z. Sándor, B. Érdi, and C. Efthymiopoulos. The phase space structure around L_4 in the restricted three-body problem. *Celestial Mechanics and Dynamical Astronomy*, 78:113–123, 2000.

D. A. Vallado. *Fundamentals of Astrodynamics and Applications*. Microcosm Press and Springer, third edition, 2007.

B. F. Villac. Using FLI maps for preliminary spacecraft trajectory design in multi-body environments. *Celestial Mechanics and Dynamical Astronomy*, 102:29–48, 2008.

B. F. Villac and J. J. Aiello. Mapping long-term stability regions using the fast Lyapunov indicator. In *15th AAS/AIAA Spaceflight Mechanics Meeting*, Copper Mountain, CO, USA, 2005. Pasadena, CA: Jet Propulsion Laboratory, National Aeronautics and Space Administration.

N. Voglis, G. Contopoulos, and C. Efthymiopoulos. Detection of ordered and chaotic motion using the dynamical spectra. *Celestial Mechanics and Dynamical Astronomy*, 73:211–220, 1999.

K. F. Wakker. *Fundamentals of Astrodynamics*. Institutional Repository, Library, Delft University of Technology, Delft, The Netherlands, January 2015.

R. A. Werner and D. J. Scheeres. Exterior Gravitation of a Polyhedron Derived and Compared with Harmonic and Mascon Gravitation Representations of Asteroid 4769 Castalia. *Celestial Mechanics and Dynamical Astronomy*, 65:313–344, 1997.

J. R. Wertz. *Orbit and Constellation Design and Management*, volume 13 of *Space Technology Library*. Microcosm Press/Springer, January 2002.

Y. Yu. *Orbital Dynamics in the Gravitational Field of Small Bodies*. Springer Theses. Springer-Verlag Berlin Heidelberg, 1 edition, 2016.

Y. Yu and H. Baoyin. Orbital Dynamics in the Vicinity of Asteroid 216 Kleopatra. *The Astronomical Journal*, 143(62):1–9, 2012.

S. P. Zhang and K. A. Innanen. The Stable Region of Satellites of Large Asteroids. *Icarus*, 75:105–112, 1988.